Radio Frequency Energy Elevation and Characterization of a Pulsed Positron Microbeam

M.Sc. Marcel Dickmann

Vollständiger Abdruck der von der Fakultät für Luft– und Raumfahrttechnik der Universität der Bundeswehr München zur Erlangung des akademischen Grades eines

Doktors der Naturwissenschaften (Dr. rer. nat.)

genehmigten Dissertation.

Vorsitzender: Prof. Dr.-Ing. Hans-Joachim Gudladt

1. Gutachter: Prof. Dr. rer. nat. Günther Dollinger

2. Gutachter: Prof. Dr. Roberto S. Brusa

Die Dissertation wurde am 1. Juni 2017 bei der Universität der Bundeswehr München eingereicht und durch die Fakultät für Luft– und Raumfahrttechnik am 6. November 2017 angenommen. Die mündliche Prüfung fand am 17. November statt.

Abstract

This thesis concerns the implementation of the renewed Scanning Positron Microscope (SPM) interface, including the positron elevator, at the high intensity positron source NEPOMUC at the Munich research reactor FRM II. The interface transfers the NEPOMUC beam into a pulsed microbeam of high brightness in order to reach the stringent requirements of the microscope. With the SPM itself it is possible to measure spatially resolved positron annihilation lifetime spectra in order to investigate defects for material science.

The in-pile positron source NEPOMUC provides a once-re-moderated positron beam of $3.0 \cdot 10^7$ e^+/s, 20 eV kinetic energy, about 2 mm diameter and a transverse phase space volume in the range of 4.2 mm^{2}eV$\cdot m_\mathrm{e}$. To generate a beam spot of ≤ 2 µm on the sample, the SPM requires a phase space of less than 0.7 mm^{2}eV$\cdot m_\mathrm{e}$. For this reason, the interface is equipped with an additional re-moderation stage, which enhances the beam brightness. With every additional component, however, the manual beam alignment becomes more delicate and time consuming. Therefore, devices for beam characterization and automated beam alignment have been developed and applied with great success. Furthermore, a serious problem is that every re-moderation step leads to a loss of several keV total beam energy. Limitations, which issue from the low beam energy and the restricted space between microscope and interface, prevent an increase of the kinetic beam energy by a conventional radio frequency accelerator. Thus, we developed a new device, which increases the potential beam energy without altering any other beam parameters. To stress the differences we call the setup elevator. This final device is indispensable to operate the SPM at NEPOMUC. To verify that the high beam quality, which is achieved by the SPM interface, gets not lost as a result of the energy elevation, we determined the transverse phase space as 0.012 mm^{2}eV$\cdot m_\mathrm{e}$ for an 1-keV-elevated beam. The results show that the elevator concept and design work. In addition, the elevator is also of advantage for other positron beam facilities, since it offers the possibility to bias source and sample on the same potential.

Zusammenfassung

Diese Arbeit behandelt die vollständige Überarbeitung und Inbetriebnahme einer Anschlusseinheit (Interface) mit einer neuartigen Hochfrequenzkomponente, um das Rasterpositronenmikroskop (SPM) mit der intensiven Positronenquelle NEPOMUC am Münchner Forschungsreaktor FRM II zu betreiben. Das SPM dient zur ortsauflösenden Positronenlebensdauer-Spektroskopie, einem sensitiven Verfahren zur Defektanalyse in Materialien. Im Interface muss dafür der NEPOMUC-Strahl gepulst und remoderiert werden, um die Anforderungen des Mikroskopes zu gewährleisten.
NEPOMUC erzeugt einen remoderierten Positronenstrahl von $3.0 \cdot 10^7\ \mathrm{e}^+/\mathrm{s}$, einer kinetischen Energie von 20 eV, einem Durchmesser von ca. 2 mm und einem transversalem Phasenraumvolumen von 4.2 mm^{2}eV$\cdot m_\mathrm{e}$. Um eine Auflösung von ≤ 2 µm zu erreichen, benötigt das SPM jedoch einen Strahl mit maximalem Phasenraum von 0.7 mm^{2}eV$\cdot m_\mathrm{e}$. Darum muss der Strahl im Interface remoderiert werden. Jede zusätzliche Komponente erschwert und verlängert jedoch die manuelle Strahljustage. Deswegen wurde ein System zur automatischen Strahlcharakterisierung und –justage entwickelt und erfolgreich eingesetzt.
Mit jeder Remoderation gehen aber auch mehrere keV Strahlenergie verloren. Der begrenzte Raum zwischen Mikroskop und Interface, sowie die geringe kinetische Strahlenergie, verhindern den Einsatz eines herkömmlichen Hochfrequenzbeschleunigers. Daher wurde ein neuartiger Positronenaufzug entwickelt, welcher, im Unterschied zu konventionellen Beschleunigern, nur die potentielle Strahlenergie erhöht, alle andere Strahlparameter dabei aber unverändert lässt. Um sicherzustellen, dass die Strahlqualität bei der Erhöhung der potentiellen Energie nicht verloren geht, wurde der transversale Phasenraum eines um 1.0 keV gehobenen Strahls vermessen. Das Phasenraumvolumen von 0.012 mm^{2}eV$\cdot m_\mathrm{e}$ zeigt, dass sowohl Konzept, als auch die Umsetzung hervorragend funktionieren. Der Positronaufzug stellt darüber hinaus eine Neuentwicklung dar, die von großer Bedeutung für die Konstruktion und den Betrieb zukünftiger Positronenstrahlsysteme ist, da sich die Möglichkeit eröffnet, sowohl Quelle, als auch Probe auf das gleiche elektrische Potential zu legen.

Contents

Abbreviations

ACAR — Angular Correlation of Annihilation Radiation
ADC — Analogue Digital Converter
AMOC — Age Momentum Correlation
CDB(S) — Coincidence Doppler Broadening (Spectroscopy)
CP — Charge Parity
DB(S) — Doppler Broadening (Spectroscopy)
DC — Direct Current
DHS — Downhill Simplex Algorithm
FRM II — Forschungsreaktor München II
FWHM — Full Width at Half Maximum
HPGe — High Purity Germanium
LINAC — Linear Particle Accelerator
MCA — Multichannel Analyzer
MCP — Micro-channel Plate
MCPII — Micro-channel Plate image intensifier
NEPOMUC — Neutron Induced Positron Source Munich
OP — Open Port
PAES — Positron-induced Auger Electron Spectroscopy
PALS — Positron Annihilation Lifetime Spectroscopy
PAS — Positron Annihilation Spectroscopy
PLEPS — Pulsed Low-energy Positron System
RF — Radio Frequency
RLC — Electric Circuit Composed of Resistors, Inductors and Capacitors
SPM — Scanning Positron Microscope
VME — Versa Module Eurocard

1 Introduction

The investigation into atomic disorders like precipitates or open-volume-defects, e.g., vacancies, grain boundaries, dislocations or vacancy clusters is fundamental for the development of materials like semiconductors, alloys, polymers, etc. Positrons behave as an ideal probe for these kinds of defects due to their positive charge. By analyzing the annihilation radiation of positrons, we can obtain information about defect types, their concentration and distribution for a particular material. An extremely sensitive and non-destructive method to characterize defects is Positron Annihilation Lifetime Spectroscopy (PALS). In this method, we implant positrons into a sample and measure the time they take to annihilate with electrons. The positron lifetime changes with the electron density, and thus, with the occurrence of defects.

PALS is a well known technique in material science and often performed using radioactive sources, which emit positrons of several 100 keV resulting in position ranges of several 100 µm to mm. The capability of PALS increase considerably using a monoenergetic positron beam of variable energy. The Pulsed Low Energy Positron System (PLEPS) benefits from the intensive beam of NEPOMUC (NEutron induced POsitron source MUniCh) at the research reactor FRM II for PALS. A variable implantation energy between 1 to 20 keV enables this outstanding system depth-resolved measurements in thin films of mm to µm thickness with a time resolution in the order of 200 ps.

However, PLEPS can not be used to investigate inhomogeneous defect distributions on the sub-millimeter scale, since the positron beam has a diameter of 1 - 2 mm. Therefore, the Scanning Positron Microscope (SPM) was developed at the Universität der Bundeswehr München. Equipped with a ^{22}Na positron emitter and several pulsing components, it provides a pulsed positron microbeam, which can be scanned over a sample in order to measure spatially resolved PALS. The technique of positron re-moderation increases the beam brightness being necessary to create a microbeam of sufficient positron intensity. For re-moderation the positrons are implanted into a mate-

rial with a negative positron work function. Here, they are thermalized and a fraction of about 20 % is re-emitted from the surface. Due to the low positron yield of the SPM's conventional positron source and therefore exceedingly long measurement times, we decided to replace the radioactive source with NEPOMUC. By combining the capabilities of the SPM with the power of NEPOMUC, we expec to improve the count rate and the spatial resolution simultaneously.

However, the beam quality of NEPOMUC does not fulfill the stringent requirements of the SPM. The transverse phase space volume of the NEPOMUC primary beam is about 5300 mm^{2}eV$\cdot m_\mathrm{e}$, and therefore, much higher than the 0.67 mm^{2}eV$\cdot m_\mathrm{e}$ of the SPM primary beam. A precise discussion of positron beam emittances is presented in Chapter 3. Another problem is that the maximum achievable electric potential of the NEPOMUC source is not sufficient to reach the desirable beam quality by re-moderation. As a consequence, several re-moderation stages have been set into operation. The first one is the NEPOMUC remoderator, which increases the brightness of the primary beam. It is possible with only one re-moderation to generate a beam of about 4.2 mm^{2}eV$\cdot m_\mathrm{e}$ transverse phase space volume, which is well-suited for most devices connected with NEPOMUC. However, the SPM requirements are much higher (see above). Because of that, a special interface has been built, which pulses the beam and increases its brightness with an additional re-moderation stage. Unfortunately, after a first test cycle it has been dismantled and stored. During the four years of work for this thesis, this interface has been set up again with improved components.

Moreover, the SPM operation at NEPOMUC differs totally from the laboratory. Up to five experiments are connected to NEPOMUC but they can not be supplied with positrons simultaneously. This means that the beam time for each instrument is limited and that the beam transport through the whole setup must be readjusted in every new measurement period. To accelerate this, additional components have been included, where we can measure the beam properties directly. In addition, we programmed a new software, which offers the possibility to optimize the beam transport automatically. The goal is to reduce the time for the adjustment and to focus on material physics.

Although the beam brightness increases by re-moderation, every re-moderation step destroys several keV of kinetic beam energy. It is not possible to increase the kinetic energy by acceleration, if we want to retain the achieved, high beam quality. To avoid sample voltages of more than 20 keV, we developed a new device, which compensates the losses. This final component of the SPM interface, called positron elevator, is necessary to operate the SPM at NEPOMUC. The elevator uses electric RF fields, which

raise the positron beam over a potential step of 10 keV without any change in other beam characteristics. To check the fulfillment of these requirements, we must provide additional ports for beam monitoring.

In this work we describe how the NEPOMUC beam is converted into a high brightness pulsed microbeam. The thesis is structured as follows:

In Chapter 2 we describe briefly the interaction between positrons and matter. Based on these fundamental processes we explain established positron annihilation techniques, particularly PALS. In addition, a brief selection of devices that use positron annihilation are presented. We explain the SPM setup and particular applications in more detail, together with the limits of the SPM in the laboratory configuration.

Chapter 3 contains common techniques for positron beam creation and preparation. In the beginning we explain various positron sources and their characteristics. After that, the method of positron moderation is described which enables to generate a monoenergetic positron beam of reduced emittance compared to the incoming beam. The following sections concentrate on the beam transport and manipulation. We describe the fundamentals to transport and focus a charged beam. Based on these principles we introduce the capability to enhance the brightness of a positron beam with a remoderator. Since the SPM requires a pulsed beam, we explain the techniques of beam bunching and chopping. At the end of the chapter we discuss physical limits for the SPM resolution.

In Chapter 4 we present the final status of the SPM interface at NEPOMUC as achieved in our work. We show several positron lifetime spectra, which show the performance of the pulsing system. An analysis of detected annihilation radiation for different settings demonstrates the efficiency of the additional interface re-moderator. We describe the new beam optimization software, which simplifies the beam adjustment considerably. In order to determine the beam quality a special sample chamber has been built, which enables the first spatial resolved PALS measurements at NEPOMUC. In addition, it was possible to obtain the worldwide first four-dimensional positron age momentum correlation (4D AMOC) spectra.

Chapter 5 explains the whole positron elevator concept. We describe the functional principle of beam elevation and discuss the requirements on the beam itself as well as on the elevator. Since the setup is widely determined by constructional confinements and limits due to particle optics, we explain the chosen design and the associated settings. The performance is shown by the analysis of many measurements with the dedicated beam

monitor. Lifetime spectra of the elevated and non-elevated beam show the influences of the elevator on the beam's time structure. Furthermore, we apply a special setup to determine the transverse phase space volume of the beam after an energy elevation by 1 keV.

Based on the results of the previous sections, we discuss the future performance of the SPM at NEPOMUC in Chapter 6. The expected count rate, as well as the spatial resolution is approximated. In addition, we present how the beam intensity and quality can be increased in future.

2 Positron Annihilation Spectroscopy (PAS)

This chapter explains briefly the fundamental processes of positron-matter-interaction. It is shown why positrons are an ideal probe for open volume defects. Different fields and the special techniques of positron annihilation spectroscopy are briefly reviewed. Based on the process of positron-electron annihilation, we discuss which investigations can be done using positrons as a microprobe. Additionally, we review a selection of devices and discuss their capabilities and limits. Next to that, we present a PALS investigation of a fatigue crack in order to explain the goals of the Munich scanning positron microscope (SPM). This example indicates the relevance of the SPM for modern material science as well as the importance to operate the SPM at the positron source NEPOMUC at the Munich research reactor FRM II.

2.1 Fundamental Properties of the Positron

In 1930 Paul Dirac postulated the positron, as a consequence of his relativistic electron theory [1]. Two years later, Carl David Anderson observed the positron in a cloud chamber. After investigation of its mass and charge he identified the newly found particle as the antiparticle of the electron [2, 3]. While the positron is stable in vacuum, its lifetime in matter is limited due to the presence of electrons. In fact, the positron lifetime is material dependent. In Table 2.1 we present a selection of fundamental positron properties.

Property	Value	Unit
charge e	$1.602176487(40) \cdot 10^{-19}$	C
rest mass m_e	$9.10938215(45) \cdot 10^{-31}$	kg
	0.510998910(13)	MeV/c^2
spin s	1/2	
magnetic moment $\lvert\vec{\mu}\rvert$	1.00115965218111(74)	μ_B

Table 2.1: Fundamental properties of the positron: The values are taken from [4] (c = speed of light).

2.2 Positrons in Matter

Today, the application of positrons as a microprobe is well established in material science [5]. Since positrons are trapped in defects, they are sensitive for various defect types, e.g., precipitates, vacancy clusters, interface misfits or dislocations [6]. In order to investigate these defects we have to implant positrons into a sample. There, they undergo various processes, which we describe in the following sections.

2.2.1 Implantation and Thermalization

After implantation into matter the positron loses its kinetic energy mainly by positron-electron scattering until it reaches thermal equilibrium. This thermalization process lasts several picoseconds depending on the implantation energy and various material properties like density or elemental composition [7]. Note, that not all positrons reach thermal energies; up to 40 % of them are already reflected at the surface [8] or they are re-emitted as epithermal positrons. In Figure 2.1 we present different processes, which positrons can undergo in a solid.

After thermalization the positrons diffuse freely. Some of them annihilate on the surface or leave the solid as epithermal positrons [9, 10]. In addition, there is the possibility for positrons to form bound surface states [11]. Another process is the formation of positronium (Ps), a hydrogen-like exotic atom consisting of a positron and an electron. We briefly discuss positronium in the next section. Additionally, there are some materials with a negative positron work function Φ_+. These materials emit thermalized positrons and provide the basis for positron moderation and re-moderation. This tech-

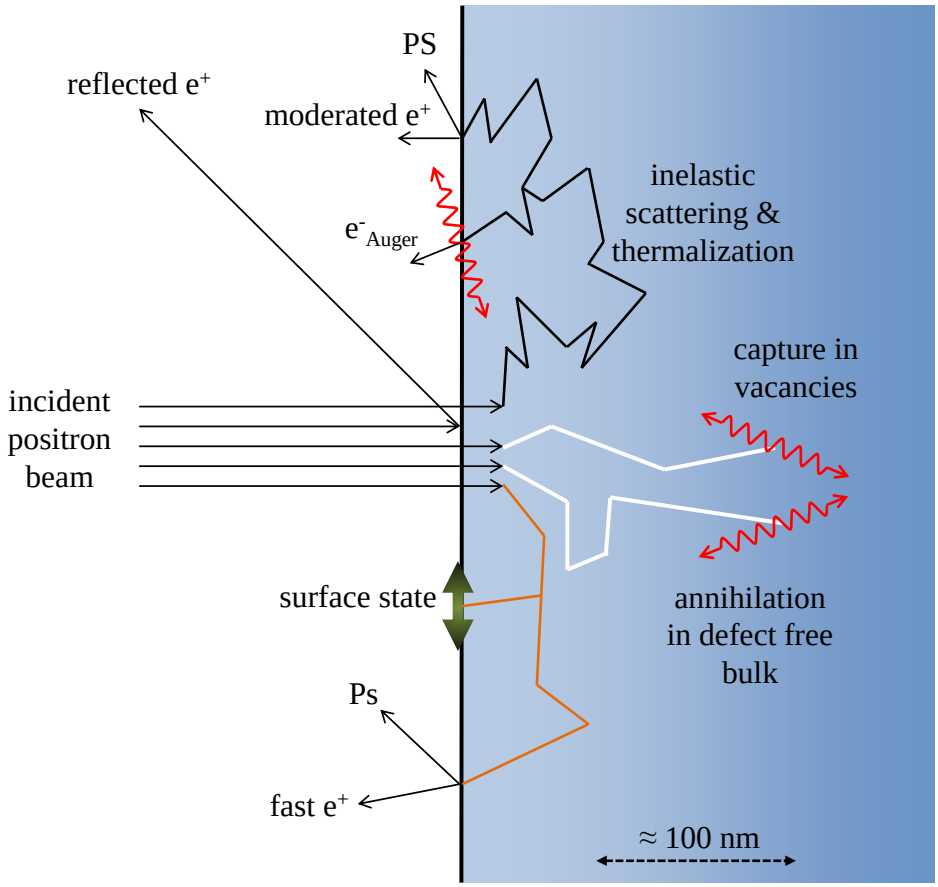

Figure 2.1: Diagram of possible processes for positrons implanted into a solid: The relevant processes for positron annihilation lifetime spectroscopy are the annihilation in the defect free bulk material and the annihilation while the positron is captured in a defect (processes with white lines).

nique is described in Chapter 3.2 and 3.4.3. However, the relevant process for positron annihilation spectroscopy (PAS) is the annihilation inside the bulk material.

We can describe the implantation profile $P(z)$ for positrons with a kinetic energy of E by a Makhovian profile [12]:

$$P(z) = \frac{m\, z^{m-1}}{z_0^m} \exp\left[-\left(\frac{z}{z_0}\right)^m\right] \tag{2.1}$$

Using the mean implantation depth $\bar{z}$, we can write the parameter z_0 as

$$z_0 = \frac{\bar{z}}{\Gamma\left(\frac{1}{m}+1\right)}\,, \tag{2.2}$$

where Γ denotes the gamma function

$$\Gamma(x) = \int_0^\infty t^{x-1}\, \mathrm{e}^{-t} \mathrm{d}t\,. \tag{2.3}$$

The parameter m in Equation 2.1 and Equation 2.2 is a material dependent parameter that can be determined by Monte Carlo simulations [13]. The mean implantation depth $\bar{z}$ is often approximated as

$$\bar{z} = \frac{A}{\rho} E^{\,n} \tag{2.4}$$

and therefore a fuction of the material densitiy ρ. A and n are material dependent parameters that have been determined via simulations and estimated in many experiments (e.g., [14–16]). In Table 2.2 we present a selection of calculated mean implantation depths $\bar{z}$ for different materials and implantation energies; Figure 2.2 depicts some calculated implantation profiles for pure copper.

2.2.2 Positronium

The bound state of an electron and a positron is called positronium, with energy levels similar to those of hydrogen. The main difference between the systems is the reduced mass μ that differs approximately by a factor of 0.5 with respect to hydrogen. This leads

Mat.	A	n	ρ	$\bar{z}$ (nm)				Ref.
	(μg·cm^{-2}·keV^{-n})		(g·cm^{-3})	2 keV	5 keV	10 keV	18 keV	
Al	2.62	1.71	2.70	31.7	152	498	1360	[17]
	3.32	1.60	2.70	37.3	161	490	1250	[18]
Al_2O_3	3.8	1.62	3.94	29.6	131	402	1040	[19]
Au	8.31	1.42	19.3	11.5	42.3	113	261	[17]
	6.58	1.49	19.3	9.5	37.5	105	253	[20]
Cu	3.78	1.61	8.92	12.9	56.6	173	445	[20]
PMMA	2.81	1.71	1.19	77.3	370	1210	3310	[14]

Table 2.2: Selection of implantation parameters A, n. The mean implantation depth $\bar{z}$ is calculated with Equation 2.4 for different implantation energies.

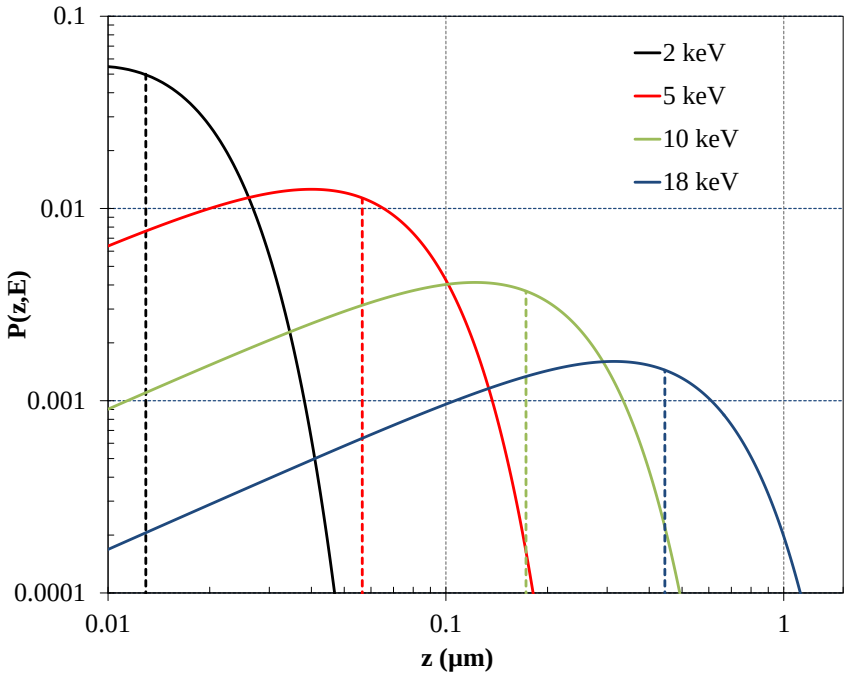

Figure 2.2: Energy dependend Makhovian implantation profiles for positrons in pure copper. The curves are calculated with the material dependent constants A, m and n taken from [20]. The corresponding mean implantation depths $\bar{z}$ are indicated as dashed lines.

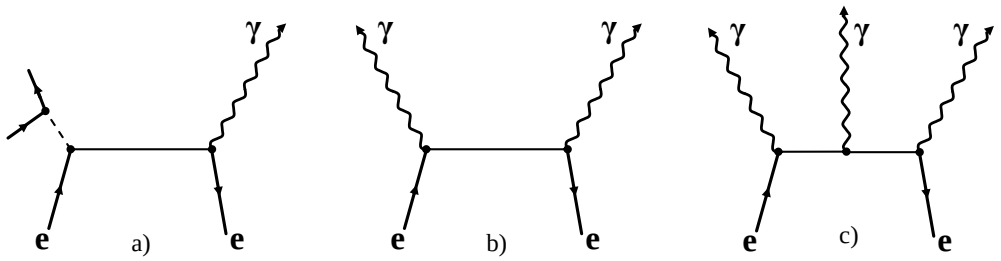

Figure 2.3: Feynman diagrams of common annihilation channels for positron and electron: a) Single photon annihilation only occurs if a third body (electron or nucleus) absorbs the recoil momentum. b) Two-γ-decay is the most possible annihilation process. c) Three-γ-decay dominates the decay of ortho-positronium.

to a larger binding length of about the double Bohr radius and a factor 0.5 in scale for the energy levels [21]. The total spin of positronium ads up to S = 0 (singlet state $\rightarrow$ para-positronium) or S = 1 (triplet state $\rightarrow$ ortho-positronium).

Electromagnetic transitions between the two states are forbidden as a consequence of the quantum mechanical selection rule $\Delta l = \pm 1$. Therefore, these states do not mix and, for non-polarized positrons, they occur according to their spin multiplicitiy [21]:

$$\frac{N_{\mathrm{para}}}{N_{\mathrm{ortho}}} = \frac{1}{3} \tag{2.5}$$

Since electron and positron annihilate after some time, the lifetime of positronium is finite. As a consequence of energy and momentum conservation at least two particles have to be created in the case of free positronium. Because of CP (Charge Parity) conservation para- and ortho-positronium form different eigenstates and can not decay in the same number of photons. Para-positronium decays in an even number, ortho-positronium in an odd number of photons [22, 23]. In Figure 2.3 we present the Feynman diagrams of the most common annihilation channels for positron and electron.

The occurrence of an additional vertex in a Feynman diagram multiplies the cross section for this process by a factor of the fine structure constant $\alpha \approx 1/137$. Thus, the ratio of the cross sections for these processes is [23]:

$$\frac{\sigma_{3\gamma}}{\sigma_{2\gamma}} \approx \alpha \tag{2.6}$$

Since the cross section for two-γ-decay is more than two orders of magnitude larger than that for the three-γ-decay, the lifetimes for both differ considerably. Positronium is often formed at the surface of metals or semiconductors. The lifetime of the two states can be found together in positron annihilation lifetime spectra of materials, which encourage the formation of free positronium [24, 25]:

$$\tau_{\mathrm{Para}} = 125 \text{ ps} \tag{2.7}$$

$$\tau_{\mathrm{Ortho}} = 142 \text{ ns} \tag{2.8}$$

Note that we can find these lifetimes only for completely free positronium. Although ortho-positronium is formed three times as much as para-positronium, the dominating annihilation process in matter is the two γ-decay. Since τ_{Para} is by a factor 1/1000 lower than τ_{Ortho}, the positron will mainly annihilate with an electron from the surrounding matter of equal probability for parallel and anti-parallel spin alignment. Therefore, in matter the 3-γ-decay is heavily suppressed and most PAS techniques observe the 2-γ-decay.

2.2.3 Diffusion and Trapping

After implantation and thermalization positrons are scattered quasi-elastically by phonons until they annihilate with electrons. The diffusion length L_{e^+} in a solid is defined by

$$L_{\mathrm{e}^+} = \sqrt{\frac{D_+}{\kappa_{\mathrm{d}} + \lambda_{\mathrm{b}}}} = \sqrt{D_+ \tau} \tag{2.9}$$

where D_+ is the diffusion coefficient [7]. It depends on different scattering processes, which the positrons can undergo during diffusion. For metals of temperature T, where the main scattering process depends on longitudinal-acoustic phonons, D_+ is proportional to $T^{-1/2}$. The parameters κ_{d} and λ_{b}, which appear in Equation 2.9, are the defect trapping rate and the annihilation rate in a defect free bulk material, respectively. λ_{b} is correlated with the positron bulk lifetime $\tau_b = 1/\lambda_{\mathrm{b}}$. Both quantities are explained in more detail in Section 2.4.

In a defect free lattice we can describe the positron as a wave packet of delocalized Bloch states, which diffuses randomly through the solid. The diffusion process is determined by phonon scattering and lasts for some hundred picoseconds. Typical diffusion lengths are in the range of 100 nm. Diffusion can be terminated when the positron reaches an open-volume defect, where the energy level is lower than in the delocalized state. Such an attractive potential leads to a localization of the wave function, which means that the positron is trapped. From shallow traps with a binding energy up to several kT, positrons can escape due to thermal excitation. However, typical defect potentials are in the range of some eV, so that most thermal positrons annihilate inside the defect after they are captured. The trapping process causes the high sensitivity of positrons for defects. As a consequence, we can use positrons as microprobes for defect spectroscopy.

2.3 Investigation of the Electron Momentum (ACAR/DBS/CDBS)

In the center of mass system the positron and the electron annihilate into two γ-quanta of 511 keV energy each, where γ-rays propagate in opposite directions. However, the annihilation in the laboratory system differs, if the momentum of the annihilating positron-electron system is not zero. As a consequence of momentum conservation the energies of the photons and their propagation directions change. To describe this behavior we look at the electron momentum and split it in a transverse component p_T and a longitudinal component p_L. The notations *transverse* and *longitudinal* refer to the propagation direction of the annihilation γs. The transverse electron momentum leads to an angular deviation Θ from 180°:

$$\Theta = \frac{p_\mathrm{T}}{m_\mathrm{e} c} \tag{2.10}$$

The longitudinal momentum component causes a Doppler shift and therefore a change of each γ-energy:

$$\Delta E = \frac{1}{2} p_\mathrm{L} c \tag{2.11}$$

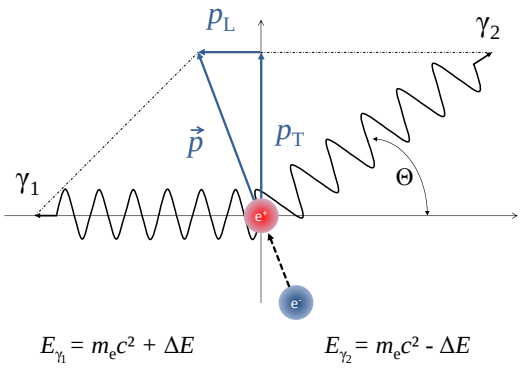

Figure 2.4: Scheme of the positron electron annihilation in the laboratory system: The longitudinal component of the electron momentum p_L leads to a Doppler shift of the γ-energy. The transverse component p_T causes an angular deviation Θ of the two γ-quanta.

The process leads to a symmetrical broadening of the 511 keV peak in the corresponding energy sprectrum. We depict the mechanism in Figure 2.4.

A technique to measure the angular deviation of the two γs is called Angular Correlation of Annihilation Radiation (ACAR). Beside a high angular resolution it requires the feasibility to detect both annihilation γ-quanta at the same time. With ACAR it is possible to investigate the structure of Fermi surfaces [5].

High Purity Germanium (HPGe) detectors are commonly used to measure the Doppler broadening of annihilation γs, due to their high energy resolution in the range of 1 keV. In Figure 2.5 we illustrate a spectrum, which can be obtained by Doppler Broadening Spectroscopy (DBS). With this technique we are able to determine defects by the use of two line shape parameters: S (shape) and W (wing). We define them as areas under the broadened 511 keV peak in relation to the whole area. They are located symmetrically to the center of the peak. The regions for S and W can be adapted with respect to different materials or required measurement statistics. Commonly used values for a reference measurements (e.g., the Doppler broadened peak of a defect-free solid) are $S \approx 0.50$ and $W \approx 0.25$. [5]. We can extend the DBS technique using two HPGe in coincidence, to obtain both annihilation γs. This leads to a considerable reduction of the annihilation background in the spectra and is called Coincidence Doppler Broadening Spectroscopy (CDBS).

The electron-positron interaction causes a much higher probability for the annihilation with a valance electron, than with a core electron. Core electrons own a higher mo-

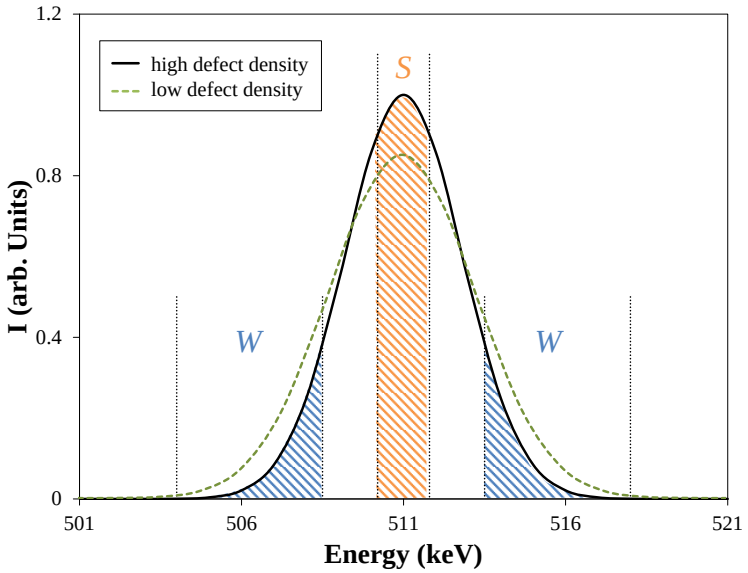

Figure 2.5: Scheme of a Doppler broadened 511 keV peak: The regions to determine the S and W parameter are indicated. The regions are set symmetrically with respect to the peak where the exact borders can vary in size and location. The green dotted line indicates a spectrum with lower S, but higher W parameter with respect to the black reference curve.

mentum than valence electrons. Missing core electrons in a defect lead to a sharper 511 keV peak and therefore a rise of the S parameter with respect to a defect-free material. Simultaneously the W parameter decreases.

2.4 Positron Annihilation Lifetime Spectroscopy (PALS)

The lifetime of a positron is finite in matter due to the electrons present and therefore it is material dependent. The cross section for annihilation in two γ-quanta can be written as

$$\sigma_{2\gamma} = \pi r_0^2 \, c \left(\frac{2\,E}{m_\mathrm{e}}\right)^{-1/2} = \pi r_0^2 \frac{c}{v_{\mathrm{e}^+}} \,, \tag{2.12}$$

with the classical electron radius $r_0 = e^2/(4\pi\epsilon_0 m_e c^2)$ and the positron velocity $v_{e^+} << c$ [23]. In the case of a two-γ-decay, the annihilation rate is proportional to the mean electron density n_{e^-}:

$$\Gamma_{2\gamma} = \frac{1}{\tau_{2\gamma}} = \sigma_{2\gamma} v_{e^+} n_{e^-} = \pi r_0^2 c n_{e^-} \tag{2.13}$$

Since the positron lifetime depends on the overlap between positron and electron wave function, τ is a function of the local electron density $n_{e^-}(\mathbf{r})$:

$$\tau_{2\gamma}^{-1} = \lambda_{2\gamma} = \pi r_0^2 c \int n_{e^+}(\mathbf{r}) n_{e^-}(\mathbf{r}) \gamma_E \mathrm{d}\mathbf{r} \tag{2.14}$$

Here, $\lambda_{2\gamma}$ is the annihilation rate, $n_{e^+}(\mathbf{r})$ is the local positron density and γ_E is the enhancement factor, which takes the distortion of $n_{e^-}(\mathbf{r})$ into account due to Coulomb interactions with present positrons. If $n_{e^-}(\mathbf{r})$ is known, we are able to deduce the positron bulk lifetime of a certain material via Equation 2.14. It is evident that the occurrence of defects changes $n_{e^-}(\mathbf{r})$, so we can observe the positron lifetime to identify defects.

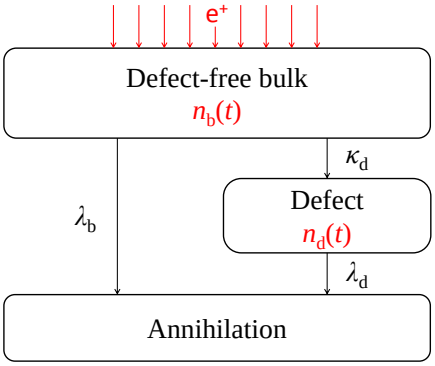

Figure 2.6: Diagram of a simple trapping model with one defect type and without detrapping.

In Figure 2.6 we depict a simple trapping model [26] containing only one type of defect. Here, the positron has the opportunity to annihilate in two ways: either it annihilates directly in the defect-free bulk material or after trapping in a defect. Assuming a ho-

mogeneous defect distribution and no escape from defects, we can set up the following rate equations:

$$\frac{\mathrm{d}n_\mathrm{b}(t)}{\mathrm{d}t} = -(\lambda_\mathrm{b} + \kappa_\mathrm{d})\, n_\mathrm{b}(t) \tag{2.15a}$$

$$\frac{\mathrm{d}n_\mathrm{d}(t)}{\mathrm{d}t} = -\lambda_\mathrm{d}\, n_\mathrm{d}(t) + \kappa_\mathrm{d}\, n_\mathrm{b}(t) \tag{2.15b}$$

The number of positrons in the bulk material $n_\mathrm{b}(t)$ changes either by direct annihilation with rate λ_b or by trapping in defects with rate κ_d. Assuming that trapped positrons cannot leave a defect, the number of captured positrons in defects $n_\mathrm{d}(t)$ is reduced only by annihilation in the trapped state with rate λ_d. Simultaneously this number increases by positrons, captured from the bulk. If we use the following expressions

$$\tau_1 = \frac{1}{\lambda_\mathrm{b} + \kappa_\mathrm{d}} \qquad \tau_2 = \frac{1}{\lambda_\mathrm{d}} \tag{2.16a}$$

$$I_1 = 1 - I_2 \qquad I_2 = \frac{\kappa_\mathrm{d}}{\lambda_\mathrm{b} - \lambda_\mathrm{d} + \kappa_\mathrm{d}} \tag{2.16b}$$

and solve the rate Equations 2.15a and 2.15b, we obtain the positron lifetime spectrum:

$$N(t) = \frac{I_1}{\tau_1}\exp\left(-\frac{t}{\tau_1}\right) + \frac{I_2}{\tau_2}\exp\left(-\frac{t}{\tau_2}\right) \tag{2.17}$$

We can extend the simple trapping model in Figure 2.6 for an arbitrary number of defect types j. This leads to $j + 1$ coupled differential equations with the solution

$$N(t) = \sum_{i=1}^{1+j} \frac{I_i}{\tau_i}\exp\left(-\frac{t}{\tau_i}\right) \ . \tag{2.18}$$

In general, $N(t)$ contains, for each defect type i, a lifetime term with a corresponding positron lifetime τ_i and an intensity I_i. In a defect-free material ($j = 0$), Equation 2.18 contains only the positron bulk lifetime $\tau_1 = \tau_b$. Note that this model represents only a simplified trapping process; it does not include other possible mechanism like de-trapping or hopping of positrons between defects.

In order to obtain $N(t)$, it is necessary to measure the time between positron implantation and annihilation for many positrons. However, we are not able to measure $N(t)$ directly. The obtained spectrum $Z(t)$ is always a convolution of $N(t)$ with the resolution function $R(t)$ plus an additional background B.

$$Z(t) = R(t) \bigotimes \left[\sum_{i=1}^{1+j} \frac{I_i}{\tau_i} \exp\left(-\frac{t}{\tau_i}\right) \right] + B \tag{2.19}$$

The resolution function depends on different parameters and is influenced by the detector resolution and the accuracy of the measurement electronics. There are several ways to determine $R(t)$, but in general, we measure $Z(t)$ for a material with a well-known positron lifetime. In this case we also know $N(t)$ and are able to obtain $R(t)$ via a numerical de-convolution.

2.5 Age Momentum Correlation (AMOC)

As mentioned in the previous sections, beside the positron lifetime it is possible to investigate the momentum of the annihilated electron. While we use PALS to obtain a lifetime spectrum, we apply DBS/CDBS and ACAR to investigate the longitudinal and transverse electron momentum, respectively. A combination of these methods provides more information than is obtainable from each individual measurement. The technique to investigate lifetime and (full) electron momentum at the same time is called Age Momentum Correlation (AMOC) [5]. In Figure 2.7 we present a two-dimensional AMOC spectrum measured by B. Loewe et al [27].

In the context of this work we have been able to perform first measurements of 4D-AMOC spectra, worldwide. For each event, the individual positron lifetime and electron momentum was measured with the pulsed beam of the SPM interface and with a pixelated HPGe detector in combination with a segmented scintillation detector, respectively. We describe this measurement in Chapter 4.5.3.

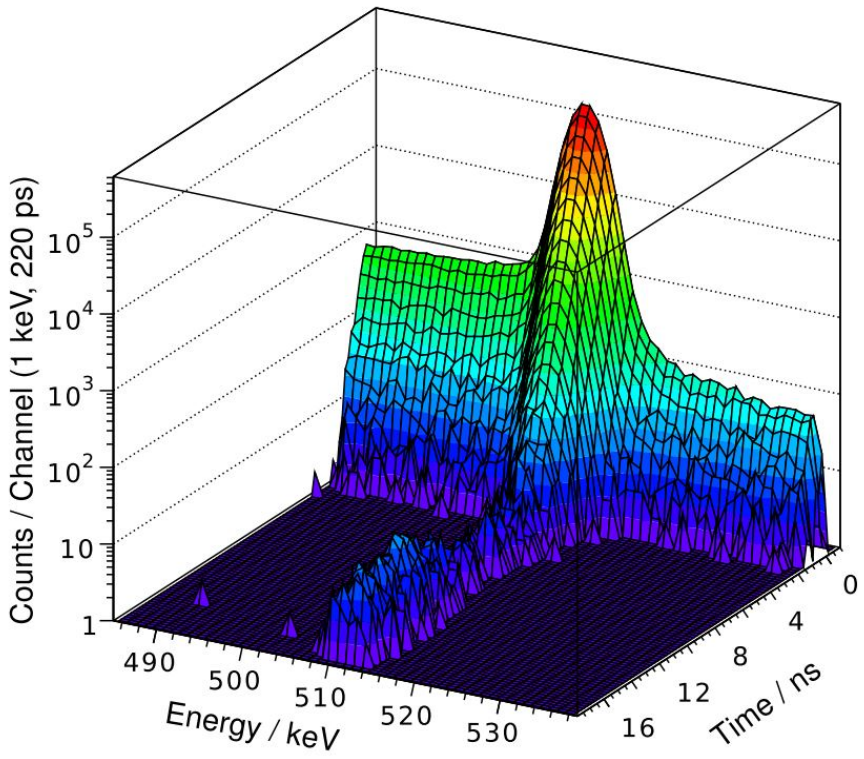

Figure 2.7: AMOC spectrum of Kapton measured with a high purity germanium detector and a BaF_2 scintillator photomultiplier detector in coincidence at PLEPS [27].

2.6 Spatial Resolved Positron Annihilation Spectroscopy

In general defects are not distributed homogeneously. A large part of material science is concerned with structures on the micrometer scale or below. If we want to realize material investigations with positrons in this field, we will need a monoenergetic positron microbeam of high brightness. Then, the lateral resolution will be achieved by scanning the microbeam and a depth resolution by variation of the beam energy. There are several experiments, which generate such a beam using the technique of re-moderation [5]. In 1987, K. F. Canter et al developed one of the first high-brightness positron beams at Brandeis University [28]. At Delft University of Technology a positron microbeam was combined with a conventional electron microscope in 1995 [29] and, two years later, a similar device was developed at Bonn University [30, 31]. In 1995, A. Zecca et al described a device to generate the first pulsed positron microbeam with positron energies in the range of keV [32]. The setup and the results were used to built the Munich Scanning Positron Microscope [33, 34].

Nowadays, there are several instruments that uses a positron microbeam for material science. Beside the SPM we present another spatial resolved positron spectrometer in the following sections.

2.6.1 The CDBS Spectrometer at NEPOMUC

The Munich Coincidence Doppler broadening Spectrometer (CDBS) uses the monoenergetic NEPOMUC beam to investigate defect distributions in three dimensions. Therefore, the 0.3 mm beam FWHM[1] can be scanned over an area of 20×20 mm^2 with step sizes between 0.1 and 10 mm and a variable energy between 1 to 30 keV. Eight HPGe detectors observe the Doppler-shifted annihilation radiation with an energy resolution of 1.4 keV (at 477.6 keV) [35]. At the moment, an upgrade of the device is under construction. The new CDBS setup contains an additional re-moderation stage, a heatable Ni(100) foil, which increases the beam brightness. First simulations show that it is possible to achieve beam spot sizes in the range of 10 µm [36].

[1] FWHM = Full Width at Half Maximum

2.6.2 The Munich Scanning Positron Microscope (SPM)

The Munich Scanning Positron Microscope (SPM) is a unique device for spatial resolved PALS. It was developed at the Universität der Bundeswehr München with the intention to investigate defect distributions in the µm-range. A. David performed first measurments as part of his PhD thesis [37]. We present a selection of measurement results obtained with the SPM in the following sections. Up to now, it operated in a laboratory equipped with a 0.5 GBq ^{22}Na source. However, the low count rate of several 100 Hz leads to exceedingly long measurement times. However, the results obtained with the SPM demonstrate the enormous potential of a pulsed positron microbeam in material science.

The SPM Setup

Figure 2.8 presents a sketch of the microscope. There are two main sections. The first section starts with the positron source and ends with the remoderator. The second part is the optical column of the microscope, where the focused beam ends on the specimen.

To generate a monoenergetic beam we use a 0.5 GBq ^{22}Na source in combination with a tungsten moderator foil. Source and foil are biased on a static potential of $\approx$ +5 kV. R. S. Brusa et al. constructed these components at the University of Trento. It delivers a continuous beam of 20 eV kinetic energy [33, 38] and a positron yield of $\approx 2 \cdot 10^5$ e^+/s [39]. The following prebuncher pulses the beam with a 50 MHz sawtooth signal of 2 V amplitude. A static magnetic field of 0.5 mT transports the beam inside the prebuncher. It behaves like a magnetic lens and images the beam from the tube entrance to its exit [33]. Afterwards, we accelerate the beam to 800 eV and transport it into a chopper, which reduces the positron background between the pulses. The 100 MHz sine wave buncher is based on the buncher of PLEPS [40] and compresses the 2 ns FWHM prebunched beam with an amplitude of $\approx$ 100 V to pulses of 200 ps FWHM [33]. P. Sperr et al. explain the pulsing system in detail in [41]. The following acceleration system increases the kinetic beam energy to 4.8 keV before the beam arrives at the remoderator on a static potential of $\approx$ +200 V. Here, we focus the beam magnetically. The beam spot on the tungsten single crystal is in the range of 20 µm FWHM [33], which is 100 times smaller in size compared to the primary source [32].

The remoderator crystal is positively biased on +200 V. Thus, the re-moderated beam can leave the remoderator and pass the beam switch again, which is biased to ground.

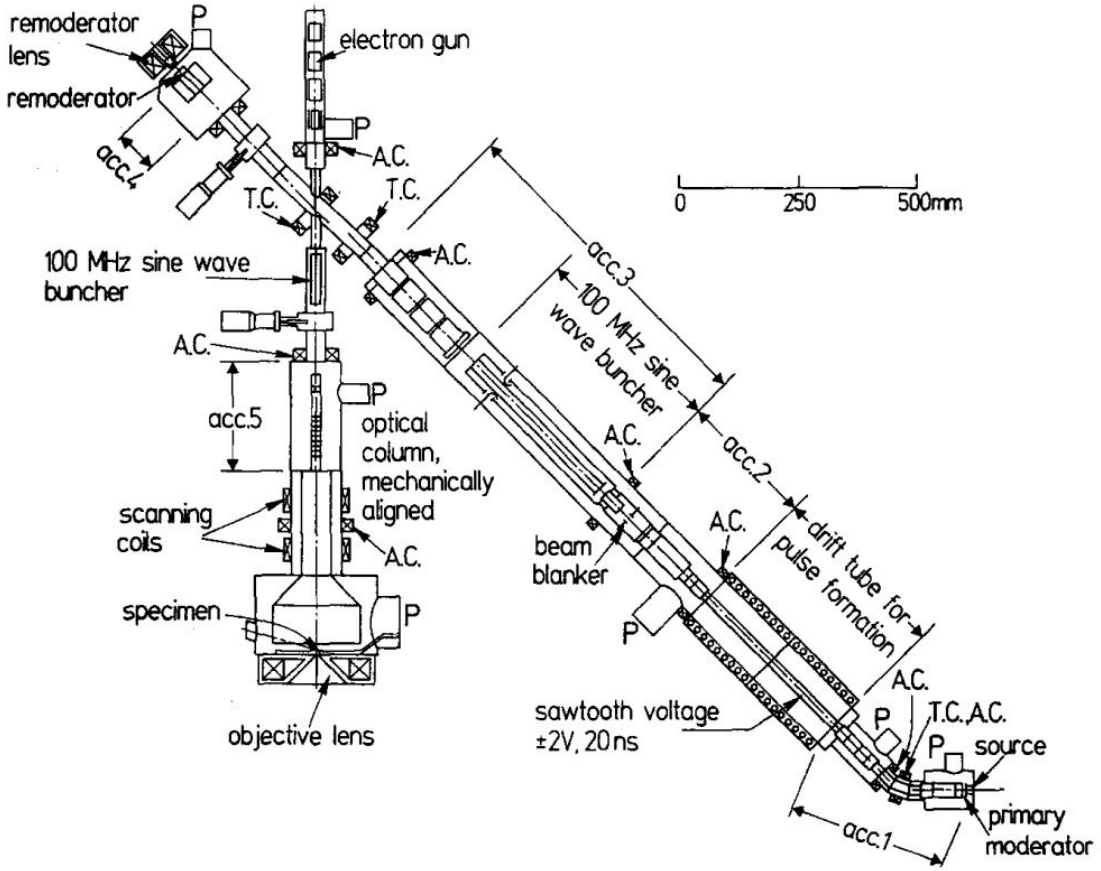

Figure 2.8: The SPM laboratory setup: A 0.5 GBq ^{22}Na source in combination with a tungsten moderator foil produces a monoenergetic positron beam. Several bunching components generate beam pulses in the range of 100 ps FWHM. The remoderator increases the beam brightness. We are able to scan the ≈ 1 µm FWHM beam in an area of about 600×600 µm^2. The annihilation radiation is recorded with a BaF_2 scintillator detector. [33]

There, we separate primary and secondary beam by toroidal deflection coils so that the re-moderated beam enters the optical column of the microscope. The second sine wave buncher further compresses the pulsed beam to $\approx$ 100 ps FWHM and the last accelerator increases the kinetic beam energy up to 20 keV. The beam is deflected via two pairs of scanning coils and demagnified by a magnetic objective lens. That way we are able to achieve a beam spot size on the specimen surface of $\approx$ 1 µm FWHM [33] including about $2 \cdot 10^4$ e^+/s [39]. It is possible to scan an area of about 600 $\times$ 600 µm^2 without moving the specimen [34]. To achieve positron lifetime spectra we use a BaF_2 scintillator detector, which is placed inside the pole shoe of the single pole objective lens.

Additionally, the positron microscope includes an electron gun, which enables to use the device as a scanning electron microscope. We are able to obtain an overview image of 1 $\times$ 1 mm^2 in 2 minutes with an electron current of 500 µA [37]. A positron lifetime map of the same sample area would take 1 day, assuming a measurement time of 30 s per pixel [37].

Applications and present limits of the SPM

A. David et al published first spatial resolved PALS measurements obtained with the SPM in 2001. Besides a test chip to determine the spatial resolution, he presented a two-dimensional positron lifetime map of a scratched GaAs sample [42]. These measurements show a spatial resolution of about 5 µm for a positron implantation energy of 8 keV and a count rate of about 100 Hz, which corresponds to a beam intensity of about $4 \cdot 10^3$ e^+/s. Near the GaAs scratch they found large vacancy clusters extending from the surface down to 0.76 µm. However, due to the low count rate and, therefore, low statistical quality of the data, it was not possible to analyze these results quantitatively.

In 2002, W. Egger et al presented 2D PALS maps of a fatigue crack in technical copper [43]. They investigated a total sample region of about 200 $\times$ 400 µm^2 with 5, 8 and 16 keV positron implantation energies and found large vacancy clusters in a zone along the crack. The results experimentally confirmed the existence of such clusters and extend the understanding of crack formation and propagation. Figure 2.9 shows an optical image and an SPM image of the crack. The complete lifetime map includes 600 single spectra, where each spectrum includes $\approx$ 1.5 $\times 10^5$ counts and represents one image pixel. The measurements for the whole picture took about one week.

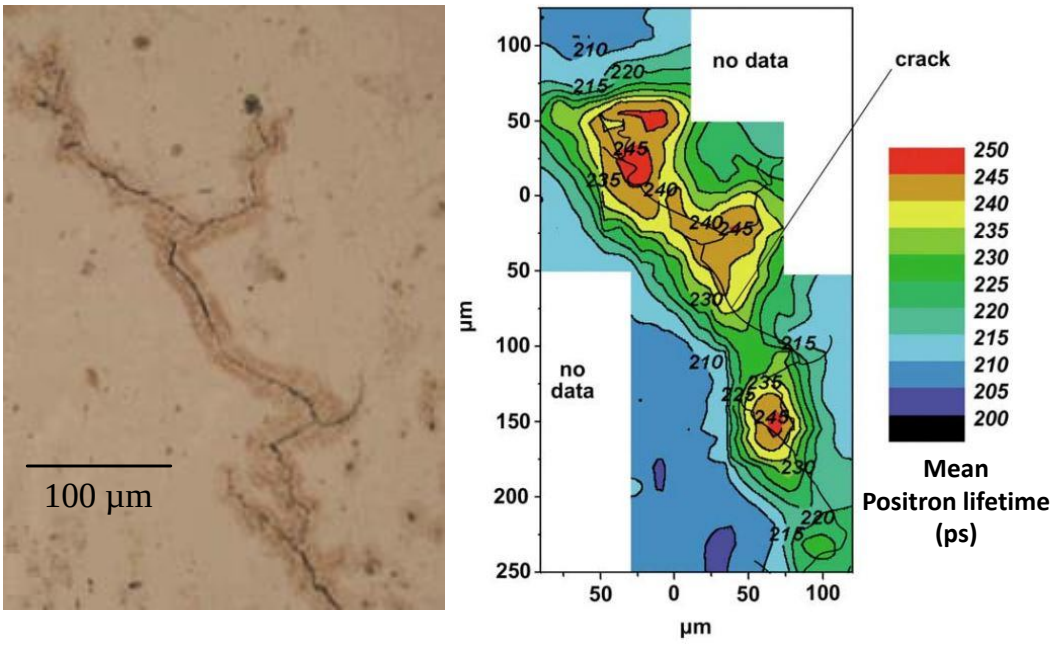

Figure 2.9: Fatigue crack in technical copper: Optical image (left) and mean positron lifetime map, obtained with the SPM at 16 keV implantation energy and a beam spot size of 5 µm. The picture is taken from [43].

Up to now, SPM measurements have been published, e.g., [44–46]. However, the low count rate restricts the application of the SPM considerably. Since we can not increase the yield of a conventional positron source as desired, the SPM will be connected to NEPOMUC. We explain the NEPOMUC source and the necessary beam preparation later in Chapter 4. However, we can do a first approximation for the count rate, which we can expect at the FRM II: The intensity of the re-moderated NEPOMUC beam is about $3 \cdot 10^7$ e^+/s. We have to apply two more re-moderation stages to achieve a necessary beam quality. The efficiency of one stage can be estimated as ≈ 20 %. Assuming an additional positron loss of 70 % caused by the pulsing system and the beam transport, we obtain for the SPM at NEPOMUC a beam intensity of $3.6 \cdot 10^5$ e^+/s. This implies that we will increase the count rate by a factor ≈ 18, which reduces the measurement time for one sample to less than a half day. Simultaneously, we want to improve the spatial resolution of the microscope to < 1 µm. However, the well-balanced column of the SPM should remain unaltered, since a future improvement seems not to be substantially possible.

Note that it is not the purpose of the SPM to compete with electron microscopes. Although both systems work with equivalent methods of particle optics, the resolution of an electron microscope will be always better due to the very much higher brightness

of its source. The great advantage of the SPM is the generation of the image contrast, which render vacancy type objects on the nanometer-scale, at low concentrations that cannot be imaged by electrons.

3 Positron Beam Techniques

In this chapter we discuss common techniques to generate and manipulate a positron beam. First, the principles and the properties of available positron sources are explained. We describe the method of positron moderation, which is essential to create a monoenergetic beam. Afterwards, we describe the motion of a charged particle beam in a homogeneous magnetic field. The positron re-moderation technique is explained; an essential method to increase the beam brightness. We describe capabilities to focus a charged particle beam, based on the fundamentals of particle optics. Since it has been necessary for this work to pulse the continuous NEPOMUC beam, we discuss bunching and chopping.

3.1 Positron Sources

In general, there are two different ways to produce positrons: β^+ decay of radioactive isotopes or production via pair production. Basically, the source properties determine most capabilities of a positron experiment. We can increase or decrease the quality of the results by changing the source. Therefore, the choice is made due to source properties like positron yield, the energy range or source handling. In addition, we have to consider the costs for source operation and maintenance.

3.1.1 Radioactive Sources

An established way to provide positrons for laboratory experiments is the β^+ decay of radioactive isotopes. In β^+ decay, a proton decays in a neutron n, a positron e^+ and an electron neutrino ν_e inside the atomic nucleus:

$$\mathrm{p} \longrightarrow \mathrm{n} + \mathrm{e}^+ + \nu_\mathrm{e} \,. \tag{3.1}$$

We can denote the β^+ decay for an initial nuclide X, with Z protons and a muss number A, which decays in a progeny Y as

$$ {}^{A}_{Z}X \longrightarrow {}^{A}_{Z-1}Y + \mathrm{e}^+ + \nu_\mathrm{e} \, . \tag{3.2} $$

Because of the three decay products, fractions of the proton binding energy are transferred into as kinetic energy of positron and neutrino. Therefore, the energy spectra of all β^+ emitters are continuous, with kinetic energies from 0 to MeV. In Table 3.1 we present a selection of commonly used β^+-sources for laboratory experiments.

Nuclide	$\tau_{1/2}$	E_mean (keV)	E_max (keV)	I_{e^+}	E_γ (keV)	I_γ
$^{18}\mathrm{F}$	110 min	249.8	633.2	0.967		
$^{22}\mathrm{Na}$	2.60 a	215.5	545.4	0.898	1275	0.999
		835.0	1819.7	0.001		
$^{58}\mathrm{Co}$	70.8 d	201.3	475.2	0.150	811	0.994
$^{64}\mathrm{Cu}$	12.7 h	278.1	652.5	0.179	1346	0.005

Table 3.1: Commonly used β^+ emitters with specific half life $\tau_{1/2}$, average positron energy E_mean, end-point energy E_max of the emitted positron spectrum, positron yield I_{e^+} and the dominant γ-energy E_γ with its corresponding intensity I_γ. The data have been taken from [47].

Most PAS studies use the sodium isotope $^{22}\mathrm{Na}$, with a half life of 2.6 years. By β^+ decay it is transformed into an excited neon state $^{22}\mathrm{Ne}^*$, which emits a 1275 keV promt γ-quant. This photon can be detected to generate a start signal for conventional PALS [5]. We depict the process of the $^{22}\mathrm{Na}$ decay in Figure 3.1.

3.1.2 Pair Production

Pair production is, beside radioactive sources, an alternative to supply positrons for various kinds of experiments. In contrast to β^+ sources, the positron yield in pair production is not limited by self absorption. The basic principle of this method is the conversion of γ-quanta into electron-positron pairs. For that, we need a minimum γ-energy

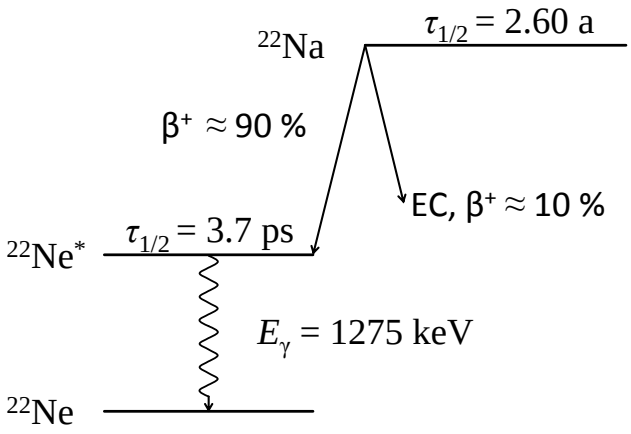

Figure 3.1: The diagram explains the decay of $^{22}\mathrm{Na}$ under emission of a positron. This process occurs with a probability of approximately 90 percent in contrast to other mechanism (e.g. electron capture). The excited daughter nuclide $^{22}\mathrm{Ne}^*$ falls to the ground state by emitting a 1275 keV γ-quant.

of $E_{\gamma,\mathrm{min}} = 2 \cdot m_\mathrm{e}c^2 = 2 \cdot$ 511 keV and a converter material of a high atomic number Z. We can write the pair production as

$$\gamma \longrightarrow \mathrm{e}^+ + \mathrm{e}^- \,. \tag{3.3}$$

Usually, the γ-energy E_γ is higher than $E_{\gamma,\mathrm{min}}$. In this case, the excess energy that is not spend for the pair production process is transferred into kinetic energy of the products and the involved converter nucleus. One can calculate the cross section of pair production σ by quantum electrodynamics as

$$\sigma = 4\alpha Z^2 r_0^2 f(E_\gamma, Z) \,, \tag{3.4}$$

where α is the fine structure constant, r_0 the classical electron radius and $f(E_\gamma, Z)$ a complex function, which increases continuously with E_γ [48]. In addition, a huge number of cross sections has been already determined in experiments. L. Strom and H. I. Israel published a very sophisticated table with cross section for photon energies from 1 keV to 100 MeV and elements with atomic number from 1 to 100 [49].

One of the first slow positron beams was generated via pair production, using the bremsstrahlung of an electron LINAC [50]. The intensive positron source NEPOMUC

delivers up to $1 \cdot 10^9$ slow positrons per second by pair production in a platinum converter [51]. We explain NEPOMUC in more detail in Chapter 4.1.

3.2 Positron Moderation in Solids

We described in the previous sections the generation of positrons by pair production or by using radioactive sources. The kinetic energy of these positrons differ enormously. While $^{22}\mathrm{Na}$ provides positrons with energies up to 545 keV [52], pair production positrons can reach energies of several MeV [53]. Most PAS techniques, however, increase considerably when using a monoenergetic low-energy positron beam.

Fortunately, there is a technique to equalize positron energies called moderation. It is based on the discovery of materials with a negative positron workfunction ϕ_+. After a positron is implanted into such a material, it looses its kinetic energy until it reaches thermal equilibrium and diffuses through the lattice. Positrons close to the surface can be re-emitted with a kinetic energy in the order of magnitude of ϕ_+.

In 1950 L. Madansky and F. Rasetti first described the idea to use materials with $\phi_+ < 0$ as positron moderators [54]. Since then, several groups have investigated various materials' moderation efficiency (e.g. [55–57]). Typical values are in the range of 10 - 20 %. C. A. Murray and A. P. Mills obtained that moderated positrons are emitted perpendicular to the crystal surface in 1980 [58]. In 1986 D. A. Fischer et al confirmed this behavior [59]. Additional experiments show an angular spread for the re-emitted positrons, which is a function of the temperature [5]. Thus, we are able to minimize this spread by cooling the moderator material.

Because of annihilation, the positron diffusion time is limited. Therefore a moderator never reaches 100 % efficiency. In fact, there are a lot of processes, which limit the efficiency. As an example, positrons can leave the moderator before they reach thermal energies or they are trapped in a defect and annihilate inside the solid. We present a selection of moderator efficiencies, measured by various groups, in Table 3.2. Note that positron moderation is also possible in gases. In the context of this work, only solid state moderators are applied.

Material	Geometry	E (keV)	ϕ_+ (eV)	η_{mod} (%)	Reference
W(100)	transmission	5.0	-3.0	18	[60]
W(110)	reflection	2.0	-3.0	33	[55]
W(poly)	transmission	1.0	not specified	26	[61]
6H-SiC	reflection	1.0	-3.0	40	[62]

Table 3.2: A selection of moderator properties: The moderator efficiency η_{mod} is a function of various parameters, e.g., temperature, moderator geometry or positron implantation energy. Therefore, it is difficult to compare the values. However, we can estimate an order of magnitude.

3.3 Beam Transport and Manipulation

Since the positron is a charged particle, we are able to influence its motion via magnetic and electric fields. Similar to light optics we can focus, reflect, refract, etc. a positron beam. Today, particle optics is a highly sophisticated discipline for specialists. For convenience, we present here an elementary discussion to facilitate the understanding of the subsequent sections. There are a huge number of textbooks, which describe the mathematics of particle optics. Therefore, several mathematical expressions differ between the authors. The following sections discuss some basics, which are necessary in the context of this work. We follow the books 'Principles of Electron Optics' by P. W. Hawkes and E. Kaspers [63], and 'Electron Optics' by P. Grivet et al [64].

3.3.1 Motion of Charged Particles in Electromagnetic Fields

The motion of a free charged particle in an electromagnetic field is determined by the Lorentz force:

$$\vec{F} = q\left(\vec{E} + \vec{v} \times \vec{B}\right) \tag{3.5}$$

Here, q is the charge of the particle, which moves with velocity $\vec{v}$ through an electric field $\vec{E}$ and a magnetic induction $\vec{B}$. We can calculate the momentum $\vec{p}$ for a relativistic particle as

$$\vec{p} = \gamma m_0 \vec{v}\,, \tag{3.6}$$

where m_0 represents the particle's rest mass and $\gamma = (1-\beta^2)^{-1/2}$ is the Lorentz factor with $\beta = v/c$. By differentiating $\vec{p}$ with respect to time, we obtain, in combination with the Lorentz force, the equation of motion:

$$\frac{\mathrm{d}\vec{p}}{\mathrm{d}t} = \dot{\gamma} m_0 \dot{\vec{x}} + \gamma m_0 \ddot{\vec{x}} = q\left(\vec{E} + \dot{\vec{x}} \times \vec{B}\right) \tag{3.7}$$

A transformation into cylindrical coordinates r, φ and z leads to:

$$\frac{\mathrm{d}}{\mathrm{d}t}(\gamma m_0 \dot{r}) - \gamma r \dot{\varphi}^2 = q(E_r + r\dot{\varphi}B_z - \dot{z}B_\varphi) \tag{3.8a}$$

$$\frac{1}{r}\frac{\mathrm{d}}{\mathrm{d}t}(\gamma m_0 r^2 \dot{\varphi}) = q(E_\varphi + \dot{z}B_r - \dot{r}B_z) \tag{3.8b}$$

$$\frac{\mathrm{d}}{\mathrm{d}t}(\gamma m_0 \dot{z}) = q(E_z + \dot{r}B_\varphi - r\dot{\varphi}B_r) \tag{3.8c}$$

We can solve the equation of motion using the Lagrange formalism and generalized coordinates $q_i(t)$ and $\dot{q}_\mathrm{i}(t)$. Therefore, we need the Lagrangian $\mathcal{L}$, which can be found in many textbooks, however, the definitions can vary. In the case of relativistic particles, a very useful expression is:

$$\mathcal{L} = -\frac{1}{\gamma} m_0 c^2 + q\left(\vec{v} \cdot \vec{A} - \Phi\right) \tag{3.9}$$

Here, Φ is the electric potential and $\vec{A}$ the vector potential, which belongs to a magnetic field $\vec{B}$, so that $\vec{B} = \mathrm{curl}\vec{A}$. We obtain the particle trajectories by solving the Euler-Lagrange equation:

$$\frac{\mathrm{d}}{\mathrm{d}t}\left(\frac{\partial \mathcal{L}}{\partial \dot{q}_\mathrm{i}}\right) - \frac{\partial \mathcal{L}}{\partial q_i} = 0 \tag{3.10}$$

The term $\partial\mathcal{L}/\partial\dot{q}_\mathrm{i}$ is called the 'canonical momentum' P_{q_i} and is defined as

$$P_{q_i} = \frac{\partial \mathcal{L}}{\partial \dot{q}_\mathrm{i}} = p_{q_i} + qA_{q_i}(\vec{x}, t)\ . \tag{3.11}$$

In this expression, p_{q_i} is the ordinary kinetic momentum. Some textbooks call $qA_{q_i}(\vec{x}, t)$ the 'potential momentum'. Using cylindrical coordinates, we can rewrite Equation 3.11:

$$P_r = \frac{\partial \mathcal{L}}{\partial \dot{r}} = \gamma m_0 \dot{r} + qA_r \tag{3.13}$$

$$P_\varphi = \frac{\partial \mathcal{L}}{\partial \dot{\varphi}} = \gamma m_0 r^2 \dot{\varphi} + qrA_\varphi \tag{3.14}$$

$$P_z = \frac{\partial \mathcal{L}}{\partial \dot{z}} = \gamma m_0 \dot{z} + qA_z \tag{3.15}$$

If the Lagrangian does not explicitly depend on q_i, Equation 3.10 simplifies to

$$\frac{\mathrm{d}}{\mathrm{d}t}\left(\frac{\partial \mathcal{L}}{\partial \dot{q}_\mathrm{i}}\right) = \frac{\mathrm{d}}{\mathrm{d}t} P_{q_i} = 0 \tag{3.16}$$

and the corresponding canonical momentum P_{q_i} is a constant in time. In the case of one parameter changing adiabatically (slowly), we are able to observe the behavior of the physical system, using the one-dimensional action:

$$J_{q_i} = \oint P_{q_i} \mathrm{d}q_i \tag{3.17}$$

Here, we integrate over a full cycle of motion. If a quantity exists that stays constant, we call it 'adiabatic invariant' with respect to the corresponding canonical momentum P_{q_i}. F. S. Crawford explains the action of various physical systems in [65], where we can also find the action for charged particles in an electromagnetic field.

3.3.2 Motion in a Homogeneous Magnetic Field

A special case for the motion of a charged particle is the presence of a homogeneous magnetic field, orientated in its propagation direction z. If there is no electric field and the magnetic induction is $\vec{B} = (0, 0, B_0)$, we can write Equation 3.5 as:

$$\gamma m_0 \ddot{x} = qB_0 \dot{y} \tag{3.17a}$$
$$\gamma m_0 \ddot{y} = -qB_0 \dot{x} \tag{3.17b}$$
$$\gamma m_0 \ddot{z} = 0 \tag{3.17c}$$

We denote the particle velocities in x- and y-directions as $\dot{x} = v_x$ and $\dot{y} = v_y$, respectively, and write for Equation 3.17ba and 3.17bb:

$$\dot{v}_x = \frac{q}{m_0}\frac{B_0}{\gamma} v_y \tag{3.18}$$
$$\dot{v}_y = -\frac{q}{m_0}\frac{B_0}{\gamma} v_x \tag{3.19}$$

Consequently, we can calculate the derivatives:

$$\ddot{v}_x = -\left(\frac{q}{m_0}\frac{B_0}{\gamma}\right)^2 v_x \tag{3.20}$$
$$\ddot{v}_y = -\left(\frac{q}{m_0}\frac{B_0}{\gamma}\right)^2 v_y \tag{3.21}$$

Together with Equation 3.17b we obtain the particle velocity:

$$\vec{v}(t) = \begin{pmatrix} -iv_\perp \exp(i\omega_g t) \\ v_\perp \exp(i\omega_g t) \\ v_\parallel \end{pmatrix} \tag{3.22}$$

It includes the transverse particle velocity $v_\perp = \sqrt{v_x^2 + v_y^2}$, the velocity $v_\parallel = v_z$ parallel to the magnetic field direction and the gyration frequency $\omega_g = qB_0/(\gamma m_0)$. By integration, we find the particle trajectory $\vec{r}$, which describes a helix:

$$\vec{r}(t) = \begin{pmatrix} -\frac{v_\perp}{\omega_g} \exp(i\omega_g t) \\ -i\frac{v_\perp}{\omega_g} \exp(i\omega_g t) \\ v_\parallel \, t \end{pmatrix} \tag{3.23}$$

Using the expression

$$E_\perp := \frac{p_\perp^2}{2m} = \frac{1}{2} m v_\perp^2 \tag{3.24}$$

$$E := \frac{p_\parallel^2}{2m} = \frac{1}{2} m v_\parallel^2 \tag{3.25}$$

with the momentum $p_\perp$ and $p_\parallel$ in transverse and longitudinal beam direction, respectively, we obtain for the helix' gyration radius r_g and gyration length l_g:

$$r_g = \frac{v_\perp}{\omega_g} = \frac{v_\perp \gamma m_0}{qB_0} = \frac{p_\perp}{qB_0} = \frac{\sqrt{2\,\gamma m_0\, E_\perp}}{q\, B_0} \tag{3.26}$$

$$l_g = 2\pi \frac{v_\parallel}{\omega_g} = 2\pi \frac{v_\parallel \gamma m_0}{qB_0} = 2\pi \frac{p_\parallel}{qB_0} = 2\pi \frac{\sqrt{2\,\gamma m_0\, E}}{q\, B_0} \tag{3.27}$$

In the case of a homogeneous magnetic field in z-direction, we obtain the vector potential as $\vec{A} = (0, rB_0/2, 0)$. Therefore, the Lagrangian does not explicitly depend on the coordinates φ and z and we can write the canonical momentum P_φ as:

$$P_\varphi = \gamma m_0 r^2 \dot{\varphi} + qrA\varphi = \gamma m_0 r^2 \dot{\varphi} + q\frac{r^2 B_0}{2} \tag{3.28}$$

Since the generalized canonical coordinate φ is periodic, we can integrate the action integral on the path along one gyration to obtain the adiabatic invariants. With $\mathrm{d}\varphi = r\,\mathrm{d}l$ we can write:

$$J_\varphi = \oint P_\varphi \mathrm{d}\varphi = \oint (\gamma m_0 r\dot{\varphi} + qA_\varphi)\,\mathrm{d}l \tag{3.29}$$

To solve this equation, we split the integral in $J_\varphi = J_{\varphi,1} + J_{\varphi,2}$ and calculate the addends separately:

$$J_{\varphi,1} = \oint \gamma m_0 r\dot{\varphi}\mathrm{d}l = (\gamma m_0 r\dot{\varphi})2\pi r = 2\pi\gamma m_0 r_g^2 \omega_g \tag{3.30}$$

We apply Stokes' theorem to the second part of J_φ:

$$\begin{aligned} J_{\varphi,2} &= \oint qA_\varphi\,\mathrm{d}l = q\int \mathrm{curl}\vec{A}\,\mathrm{d}(\mathrm{area}) \\ &= q\int \vec{B}\,\mathrm{d}(\mathrm{area}) = -\pi q r_g^2 B_0 = -\pi\gamma m_0 r_g^2 \omega_g \end{aligned} \tag{3.31}$$

Note that $J_{\varphi,2}$ is negative. We can explain this result using the right-hand rule. If we add Equation 3.30 to 3.31, we obtain for the action:

$$J_\varphi = \pi\gamma m_0 r_g^2 \omega_g = \pi q r_g^2 B_0 \tag{3.32}$$

Evidently, the action integral is constant in time. In this case, $r_g^2 B_0$ is an adiabatic invariant. We can conclude that the gyration radius r_g is proportional to $B^{-1/2}$, if the magnetic field changes slowly. As a consequence, the gyration radius of a charged particle will change from $r_{g,1}$ to $r_{g,2}$, if the magnetic field varies adiabatically from $\vec{B_1} = (0, 0, B_1)$ to $\vec{B_2} = (0, 0, B_2)$:

$$r_{g,2} = r_{g,1}\sqrt{\frac{B_1}{B_2}} \tag{3.33}$$

3.3.3 Electric and Magnetic Beam Focusing

In the following sections we discuss how to focus a charged particle beam electrostatically and magnetically. Again, we follow the 'Principles of Electron Optics' by P. W. Hawkes and E. Kaspers [63] and, in addition, the book 'Einführung in die Teilchenoptik' by J. Großer [66].

Electrostatic Lenses

In this subsection, we discuss the behavior of a charged particle beam that moves in an electrostatic field, where it changes its velocity. Since the beam consists of many particles, each particle's velocity and trajectory is altered. As a results, we can use electric fields to focus the beam. The perceptions found by H. Busch and E. Brüche in the 1920s, provide the base of modern electron optics [67]. Later in 1931, C. J. Davisson and C. J. Calbick noticed the lens behavior of electric fields on an electron beam, passing round openings and slits [68,69]. A few years later, in 1939, J. Picht described such lenses in a paraxial approximation [70]. Based on these results, J. Gratsiatos published a more detailed calculation in 1940 [71].

We can create a very simple geometry for electrostatic lenses by combining two cylindrical tubes on different electric potentials Φ. We depict such an optical system in Figure 3.2. Here, the beam direction follows the tubes' axis z. We can calculate the focal length f_i of this rationally symmetric system as [63]:

$$\frac{1}{f_\mathrm{i}} = \frac{3}{16}\left|\frac{\Phi_a}{\Phi_b}\right|^{1/4} \int \left(\frac{\Phi'(z)}{\Phi(z)}\right)^2 \mathrm{d}z \tag{3.34}$$

The electric potential $\Phi(z)$ on the z-axis changes from Φ_a to Φ_b. If we know $\Phi(z)$ and its derivative $\Phi'(z) = \mathrm{d}\Phi/\mathrm{d}z$, we are able to determine f_i. By increasing the potential difference $\Delta\Phi = |\Phi_a - \Phi_b|$ between the tubes, f_i reduces. If the lens is not excited ($\Delta\Phi = 0$), the focus is placed at infinity. Note that f_i represents the focal length on image side. We can calculate the focal length on object side f_o by switching Φ_a to Φ_b. However, Equation 3.34 is a special case. We assume that the kinetic energy of the beam changes from $e\Phi_a$ to $e\Phi_b$. In general, it is possible that $E \neq 0$ for $\Phi_a = 0$ or $\Phi_b = 0$. In this case we calculate the modified potentials as

$$\Phi'_a = \left(E(0) - E(\Phi_a)\right)/e \tag{3.35}$$

$$\Phi'_b = \left(E(0) - E(\Phi_b)\right)/e \tag{3.36}$$

and use them instead of Φ_a and Φ_b.

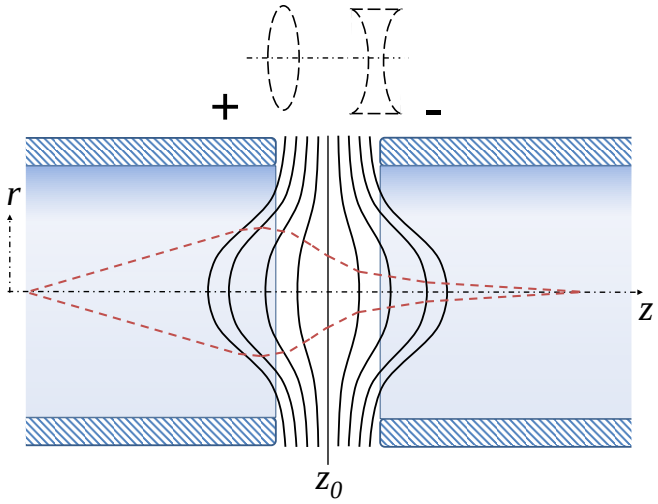

Figure 3.2: Scheme of a simple electrostatic lens, consisting of two cylindrical tubes on different electric potentials: Positive particles like positrons are always attracted in the direction of a negative potential, which leads to a focusing of the beam. However, a region of convergence is always accompanied by a region of divergence. The positron velocity is slower in the divergent region and, therefore, the convergent effect exceeds the divergent.

In reality it can be very difficult to determine $\Phi(z)$ and, therefore, $\Phi'(z)$. Thus, the electric field and the corresponding particle trajectories are often calculated by numerical computer simulations. However, it is possible to estimate $\Phi(z)$. In the simple case of two cylindrical tubes with identical radii R and a negligible gap $S << R$ in between, we can approximate $\Phi(z)$ by a $\tanh$ function [72, 73]:

$$\Phi(z) = \frac{\Phi_a + \Phi_b}{2}\left(1 + \frac{1-\gamma}{1+\gamma}\tanh\left(\frac{\omega z}{R}\right)\right) , \tag{3.37}$$

with the parameters

$$\gamma = \left|\frac{\Phi_a}{\Phi_b}\right| \qquad \text{and} \qquad \omega = \frac{1}{\pi}\int_{-\infty}^{+\infty}\frac{\mathrm{d}t}{I_0(t)} = 1.318 \tag{3.38}$$

Here, I_0 is the zero-order modified Bessel function. If there is a gap of length S that cannot be neglected but is still small compared to the radius, we can approximate $\Phi(z)$ as [63]:

$$\Phi(z) = \frac{\Phi_a + \Phi_b}{2}\left(1 + \frac{1-\gamma}{1+\gamma}\frac{R}{\omega S}\ln\frac{\cosh\left(\frac{\omega}{R}(z+S/2)\right)}{\cosh\left(\frac{\omega}{R}(z-S/2)\right)}\right) \tag{3.39}$$

This equation transfers to Equation 3.37, if S approaches zero.

In practice, the knowledge of the focal length alone is useless, since it represents the distance of the focus, measured from the principal plane. However, in most cases we are interested in the focus position measured from the gap. Nevertheless, if we know f_o and f_i, we are able to calculate the mid-focal lengths z_{f_o} and z_{f_i} [73]:

$$z_{f_\mathrm{o}} = z_0 - \left(\frac{\Phi_b}{\Phi_a}\right)^{1/4} f_\mathrm{o} \tag{3.39a}$$

$$z_{f_\mathrm{i}} = z_0 + \left(\frac{\Phi_a}{\Phi_b}\right)^{1/4} f_\mathrm{i} \tag{3.39b}$$

Here, z_0 is the reference plane of the lens; usually a plane of reflection symmetry, if such a plane exists. E. Harting and F. H. Read present a very useful selection of cardinal elements for different lens geometries in their book 'Electrostatic Lenses' [74]. We give an overview for some values, calculated with the Equations 3.34, 3.39a and 3.39b in Table 3.3.

Magnetic Lenses

Similar to electrostatic beam focusing, we can use magnetic fields to focus a charged particle beam. The pioneers of electron microscopy M. Knoll and E. Ruska proposed the application of magnetic lenses for electron imaging for the first time in 1932 [75].

E_a/E_b	f_o (mm)	f_i (mm)	z_{f_o} (mm)	z_{f_i} (mm)
1.00	∞	∞	∞	∞
1.25	1384.5	1563.0	1463.9	1478.2
1.50	399.8	498.4	442.5	456.3
1.75	201.8	273.5	232.1	237.8
2.00	127.2	185.3	151.2	155.9
2.50	68.9	113.3	86.6	90.1
3.00	45.9	83.3	60.4	63.3
4.00	27.0	57.2	38.1	40.4
5.00	19.0	45.5	28.4	30.4
10.00	9.0	27.9	14.3	15.7

Table 3.3: Selection of focal lengths $f_{\mathrm{o,i}}$ and mid-focal length $z_{f_{\mathrm{o,i}}}$ for a two cylinder lens with equal radii: The kinetic beam energy is changed from E_a to E_b, when the beam passes the lens. The values are calculated with the Equations 3.34 and 3.39. Here, $z_0 = 0$, so that $z_{f_{\mathrm{o,i}}}$ is the focus positions, measured from the gap. The values are calculated for a gap to radius ratio of $S/R = 0.2$.

The lens effects base on the Lorentz force (Eq. 3.5), which acts on the particles. Depending on the beam characteristics and the desired focusing, there are various designs to realize a magnetic lens, e.g., quadrupole doublet, quadrupole triplet, quadruplet, solenoid, etc. Since all magnetic lenses of the SPM and interface are solenoid lenses, realized by current-carrying coils, we describe only those below.

A rotationally symmetric, magnetic lens causes a magnetic induction B symmetric to its axis z. The field can be concentrated in a small region by iron cladding of the coils. We can calculate the focal length f_i for a charged particle beam, which propagates in direction of this axis as [64]:

$$\frac{1}{f_\mathrm{i}} = A \int B^2(z)\mathrm{d}z \tag{3.40}$$

The parameter A depends on the type of particles and their kinetic energy. We find [64]:

$$A = \frac{1}{8}\frac{e}{m_\mathrm{e}\Phi_0} = \frac{1}{4}\left(\frac{e}{m_\mathrm{e}v}\right)^2 = \frac{1}{8}\frac{e^2}{m_\mathrm{e}E} \tag{3.41}$$

Here, Φ_0 is the constant electric potential and $E = \Phi_0 e$ the kinetic energy for a positron of velocity v. The focal length f_i represents the distance between focus position and principal plane h_i. In general, we do not know the position of h_i, but there is a method, according to [64], to approximate it. Therefore, we denote the magnetic field on axis z as:

$$B(z) = B_0 f(z) \tag{3.42}$$

Here, $f(z)$ is a real function with values of $|f(z)| \leq 1$. B_0 represents the maximum of the magnetic field. If it is possible to determine $B(z)$, i.e., from measurements of simulations, we know B_0 and $f(z)$ as well. To calculate the cardinal elements (see Figure 3.4), we replace the real lens by a rectangular field B_0 of effective length L. According to [64], the effective length is:

$$L = \frac{1}{B_0} \int B(z) \mathrm{d}z \tag{3.43}$$

By placing the model lens between $z = 0$ and $z = L$, we can calculate the principal plane position $h_\mathrm{i} = L/2$ and, therefore, the mid-focal length as:

$$z_{f_\mathrm{i}} = \frac{L}{2} + f_\mathrm{i} \tag{3.44}$$

Figure 3.3 depicts several focus positions of the SPM remoderator lens, calculated for a 5 keV positron beam. Therefore, we measured $B(z)$ for various currents and determined f_i and z_{f_i} according to Equation 3.40 and 3.44, respectively.

We can use magnetic lenses for charged particle beams, as optical lenses for light. However, the magnetic field leads to a rotation $\Delta\theta$ of the meridian plane. If θ_o is the angle between object plane and an arbitrary reference plane and θ_i is the angle between image plane and the same reference plane, we can calculate the image rotation as [64]:

$$\Delta\theta = \theta_i - \theta_o = \sqrt{\frac{e}{8 m_\mathrm{e} \Phi_0}} \int_{z_o}^{z_i} B(z) \mathrm{d}z \tag{3.45}$$

In positron beam techniques, the short focal length of magnetic lenses is advantageous to focus the beam on remoderators or samples. Single-pole lenses [76] can be mounted

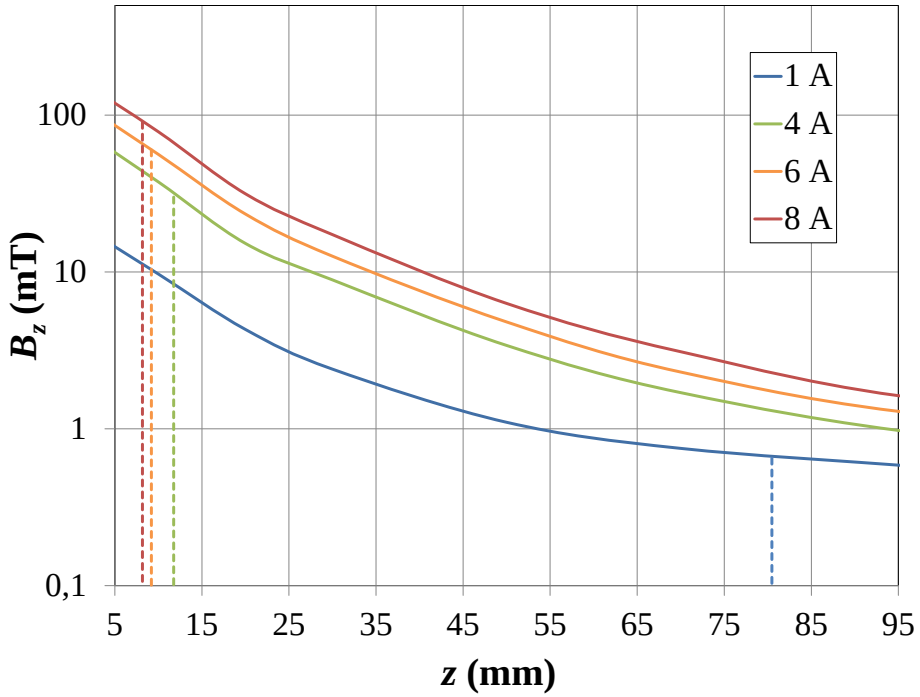

Figure 3.3: Axial magnetic field of the SPM remoderator lens, measured for different currents: The dashed lines represent the focal planes for a beam of 5 keV kinetic energy. We set the zero plane $z = 0$ on the tip of the lens pole shoe.

outside the ultra-high vacuum (UHV). In all remoderator stages (see Figures 2.8, 4.3, 4.21) as well as for the final focus at the sample of the SPM (see Figure 2.8) magnetic single-pole lenses are applied. We are also able to adjust the focus position without changing the beam energy. In addition, the application of singe-pole lenses keeps the second half space free for backscattered positrons, which can move away so that their annihilation radiation is kept from the detector.

Optical Aberrations

So far, we have discussed the paraxial optics of particles, which move permanently close to the optical axis. As in light optics, for real beams there are various aberrations from paraxial behavior. Spherical aberrations are due to larger distances to the axis. Velocity deviations of the particles lead to chromatic aberration. Furthermore, space charge effects can cause additional aberration, e.g. inside positron traps.

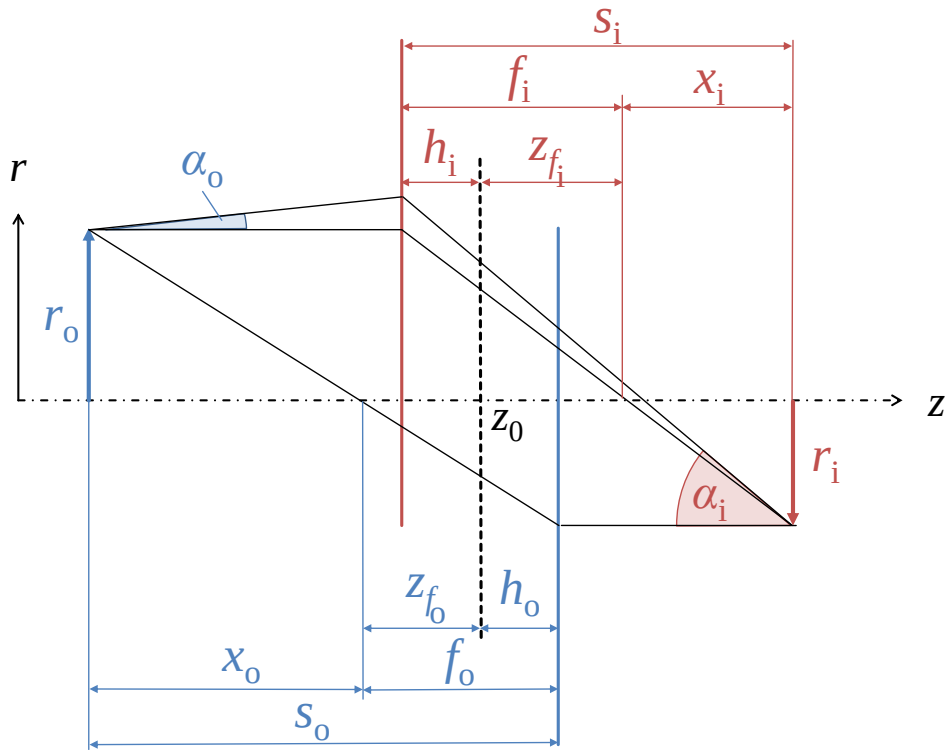

Figure 3.4: Cardinal elements of a beam focusing lens: The object size r_o is imaged to size r_i. The reference plane z_0 is placed between the two principal planes in distances of h_o and h_i. The focal lengths are denoted as $f_{o/i}$ for the object and image side, respectively. The similar denotation is used for the aperture angles $\alpha_{o/i}$ and the mid-focal lengths $z_{f_{o/i}}$.

In Figure 3.4 we find the cardinal elements for an ideal optical system. These quantities can be calculated as [63]:

$$\frac{f_\mathrm{o}}{s_\mathrm{o}} + \frac{f_\mathrm{i}}{s_\mathrm{i}} = 1 \qquad \text{Lens equation} \tag{3.46}$$

$$x_\mathrm{o} x_\mathrm{i} = f_\mathrm{o} f_\mathrm{i} \qquad \text{Newton's lens equation} \tag{3.47}$$

$$M = \frac{r_\mathrm{i}}{r_\mathrm{o}} = \frac{f_\mathrm{o}}{f_\mathrm{i}} \frac{s_\mathrm{i}}{s_\mathrm{o}} \qquad \text{Magnification} \tag{3.48}$$

$$M_\alpha = \frac{\alpha_\mathrm{i}}{\alpha_\mathrm{o}} = \frac{1}{M} \frac{f_\mathrm{i}}{f_\mathrm{o}} \qquad \text{Angular magnification} \tag{3.49}$$

The equations describe the behavior of a paraxial, ideal Gaussian beam. Particles, which are away from the optical axis z, will be refracted too strong. This leads to a reduction of the focal length and therefore a blur of the image. This effect is caused by higher order

terms, which are neglected in the paraxial approximation. Assuming that the object is a spot, we can calculate the radius of the blurred image spot for a round, rotationally symmetric lens, using the spherical aberration coefficient C_s [63]:

$$r_b = C_s \alpha_\mathrm{i}^3 \tag{3.50}$$

It can be shown that there is another plane in front of the Gaussian image plane, where the beam radius is smaller than on all other planes. This plane is called 'plane of least confusion'. Here, we can approximate the beam cross section as a disc with radius

$$r_s = \frac{1}{4} C_s \alpha_\mathrm{i}^3 \,. \tag{3.51}$$

We find that r_s is four times smaller than r_b. The position of the least confusion plane is between the focal plane f_i and the Gaussian image plane s_i in a distance of $0.75 \cdot \overline{f_\mathrm{i} s_\mathrm{i}}$ from the principal plane h_i [63].

According to Equation 3.34, 3.40 and 3.41, the focal length is a function of the kinetic particle energy. In reality, the particle velocities differ from each other, even in the case of a monoenergetic beam, which leads to chromatic aberration. We can calculate the image radius as [63]:

$$r_c = C_c \frac{\Delta E}{E} \alpha_\mathrm{i} \tag{3.52}$$

Here, ΔE is the energy spread of a beam with a kinetic energy E. In practice, we must determine the coefficients for chromatic aberration C_c and spherical aberration C_s from tables [74] or numerical computer simulations.

Minimum Achievable Spot Sizes

To determine a minimum achievable beam spot, we can combine Equation 3.48 with Equation 3.49. This leads to a spot size on image side for an aberration-free lens of

$$r_\mathrm{i} = \frac{f_\mathrm{i}}{f_\mathrm{o}} \frac{\alpha_\mathrm{o}}{\alpha_\mathrm{i}} r_\mathrm{o} \,. \tag{3.53}$$

In the case of a thin lens, the focal length on object side is equal to the focal length on image side and the expression simplifies to

$$r_\mathrm{i} = \frac{\alpha_\mathrm{o}}{\alpha_\mathrm{i}} r_\mathrm{o} \,. \tag{3.54}$$

We can approximate the divergence angle α_o, using the longitudinal particle momentum $p_\parallel$ and the transverse momentum $p_\perp$:

$$\tan(\alpha_\mathrm{o}) = \frac{p_\perp}{p_\parallel} \approx \alpha_\mathrm{o} \tag{3.55}$$

With the kinetic beam energy E and $E_\perp$ we obtain

$$\alpha_\mathrm{o} \approx \sqrt{\frac{E_\perp}{E}} \tag{3.56}$$

and r_i can be written as:

$$r_\mathrm{i} = \frac{1}{\alpha_\mathrm{i}} \sqrt{\frac{E_\perp}{E}} r_\mathrm{o} \tag{3.57}$$

To calculate the minimum achievable beam spot size r_min, we have to consider the blurring by spherical and chromatic aberrations. Since these aberrations are independent from each other and from r_i, they add up geometrically:

$$r_\mathrm{min}^2 = r_\mathrm{i}^2 + r_s^2 + r_c^2 = \frac{E_\perp}{E} \left(\frac{r_\mathrm{o}}{\alpha_\mathrm{i}} \right)^2 + \frac{1}{16} C_s^2 \alpha_\mathrm{i}^6 + C_c^2 \alpha_\mathrm{i}^2 \left(\frac{\Delta E}{E} \right)^2 \tag{3.58}$$

Note that the aberration coefficients C_s and C_c are determined for an optical system and they are independent from the beam properties. If we know the aberration coefficients, we can calculate r_min for different beam characteristics with the same lens system.

3.4 Brightness Enhancement

The brightness is the most common parameter to compare the characteristics of different particle beams. It specifies the beam's quality. For positron beams the special technique of re-moderation enables to enahce the brightness. This method was proposed by A. P. Mills in 1980 [77] and later discussed in more detail by C. F. Canter and A. P. Mills in 1982 [78]. In general the main characteristics of a positron beam are determined by its source. With common positron source it is not possible to create a positron microbeam, since the beam brightness is to low. If we want to achieve beam spot sizes in the µm-range, we have to enhance the brightness for several times by re-moderation. In the following sections, we describe the principles of this technique.

3.4.1 Brightness of a Positron Beam

There are different definitions for the brightness B in literature, depending on the field of research, the corresponding institute or the author. A very common definition for non-relativistic positron beams is used by A. P. Mills [77]:

$$B = \frac{I}{\alpha^2 d^2 E} \tag{3.59}$$

Here, B includes the beam intensity I (positrons per second), the divergence angle α, the beam diameter d and the kinetic beam energy E. We can rearrange this expression for small divergence angles $\alpha = \tan(p_\perp/p_\parallel) \approx p_\perp/p_\parallel$, using the transverse and the parallel momentum $p_\perp$ and $p_\parallel$:

$$B = \frac{2m_\mathrm{e} I}{d^2 p_\perp^2} \tag{3.60}$$

C. F. Canter introduced another definition for the brightness, which just differs from the 'conventional' definition by a factor $4/\pi^2$:

$$R_v = \frac{4}{\pi^2} B = \frac{4I}{\pi^2 \alpha^2 d^2 E} \tag{3.61}$$

Note that both definitions can be found in literature and sometimes it is not absolutely clear, how the brightness was calculated.

3.4.2 Liouville's Theorem

To describe all characteristics of a beam, we need beside the intensity I the complete occupied phase space volume Ω_{xyz}, which can be split in three components:

$$\Omega_x = \pi\,\Delta x \cdot \Delta p_x \qquad \text{(transverse phase space volume in x)} \tag{3.62}$$

$$\Omega_y = \pi\,\Delta y \cdot \Delta p_y \qquad \text{(transverse phase space volume in y)} \tag{3.63}$$

$$\Omega_z = \pi\,\Delta E \cdot \Delta t \qquad \text{(longitudinal phase space volume)} \tag{3.64}$$

These phase space volumes represent the areas of ellipses, where $\Delta x, \Delta p_x, \Delta y, \Delta p_y, \Delta E$ and Δt denote the lengths of the respective semi axes. In general, the volume of an n-dimensional ellipsoid is

$$V_n = \frac{2}{n}\frac{\pi^{n/2}}{\Gamma(n/2)}(a_1 \cdot a_2 \cdot a_3 ... a_n)\,, \tag{3.65}$$

where $a_1 ... a_n$ are the semi axes and Γ denotes the gamma function. The volume Ω_{xyz} of the complete phase space is therefore:

$$\Omega_{xyz} = \frac{1}{6}\,\pi^3\,\Delta x \cdot \Delta p_x \cdot \Delta y \cdot \Delta p_y \cdot \Delta E \cdot \Delta t = \frac{1}{6}\,\Omega_x \cdot \Omega_y \cdot \Omega_z \tag{3.66}$$

The full transverse phase space Ω_{xy} is therefore a subspace of Ω_{xyz} and represents the volume of a four-dimensional ellipsoid:

$$\begin{aligned}\Omega_{xy} &= \frac{1}{2}\,\pi^2\,\Delta x \cdot \Delta p_x \cdot \Delta y \cdot \Delta p_y = \frac{1}{2}\,\Omega_x \cdot \Omega_y \\ &= \frac{1}{2}\,\pi^2\,\Delta r^2 \cdot \Delta p_\perp^2 = \Omega_{rr}\end{aligned} \tag{3.67}$$

Here, $\Delta r = \sqrt{\Delta x \cdot \Delta y}$ and $\Delta p_\perp = \sqrt{\Delta p_x \cdot \Delta p_y}$ denote the geometric mean of the transverse beam size and momentum, respectively, and together with Equation 3.60 we obtain:

$$\Omega_{rr} = \frac{\pi^2 m_\mathrm{e} I}{4\,B} \tag{3.68}$$

The theorem of Liouville implies that the occupied phase space volume of non-interacting particles stays constant under the influence of conservative forces. This means that we are not able to increase the phase space density, and therefore the beam brightness, using conservative forces. The phase space can be reduced without violating Liouville's theorem by removing fractions of the beam, e.g. by the use of apertures. However, this does not enhance the beam brightness and leads to intensity losses.

Using Liouville's theorem, we can point out the limits of the NEPOMUC primary beam, as the following example shows: The complete transverse phase space for a beam of $d = 9.3$ mm FWHM and $E_\perp = 50$ eV FWHM is $\Omega_{rr} = 5.3 \cdot 10^3$ mm^{2}eV$\cdot m_\mathrm{e}$. Since Ω_{rr} stays constant under the influence of conservative forces, we can calculate the necessary value for $E_\perp$ to achieve a beam spot diameter of 1 µm by focusing.

$$E_\perp = 2 \cdot \frac{\Omega_{rr}}{\pi^2 \cdot \Delta r^2 \cdot m_\mathrm{e}} = 2 \cdot \frac{6.2 \cdot 10^3 \text{ mm}^2\text{eV} \cdot m_\mathrm{e}}{\pi^2 \cdot (0.5\ \mu\text{m})^2 \cdot m_\mathrm{e}} = 4.3 \text{ GeV FWHM} \tag{3.69}$$

The result shows that in reality this is not feasible. The only way to reach a beam spot size in the µm-range is to reduce Ω_{rr}. The most primitive method is to cut Ω_{rr} using apertures, which means a considerable loss of beam intensity. Therefore, the only suitable way to create a positron microbeam with NEPOMUC is the enhancement of the beam brightness by re-moderation.

3.4.3 Re-Moderation

The characteristics of a beam are mainly determined by its source. Electron guns with ultra-thin LaB_6 cathodes reach a beam brightness, which exceeds the brightness of a positron beam, generated with a ^{22}Na source and a tungsten moderator foil in combination, by a factor of 10^{16} [79]. Due to Liouville's theorem, we are not able to enhance the brightness using conservative forces. The example in the last section shows that it is

not feasible to achieve beam spot sizes in the µ-range, using a positron beam of several mm in size.

However, as mentioned in Chapter 3.2, there are materials with a negative positron work function, which we can use for brightness enhancement. For this purpose, the beam is focused on a remoderator crystal, which can be treated as a new source. The re-emitted beam is smaller in size and phase space volume and, therefore, higher in brightness. We present a diagram of the re-moderation process in Figure 3.5. In general, we can repeat this process over and over again. However, every re-moderation step entails a loss of several keV total beam energy and a decrease of intensity.

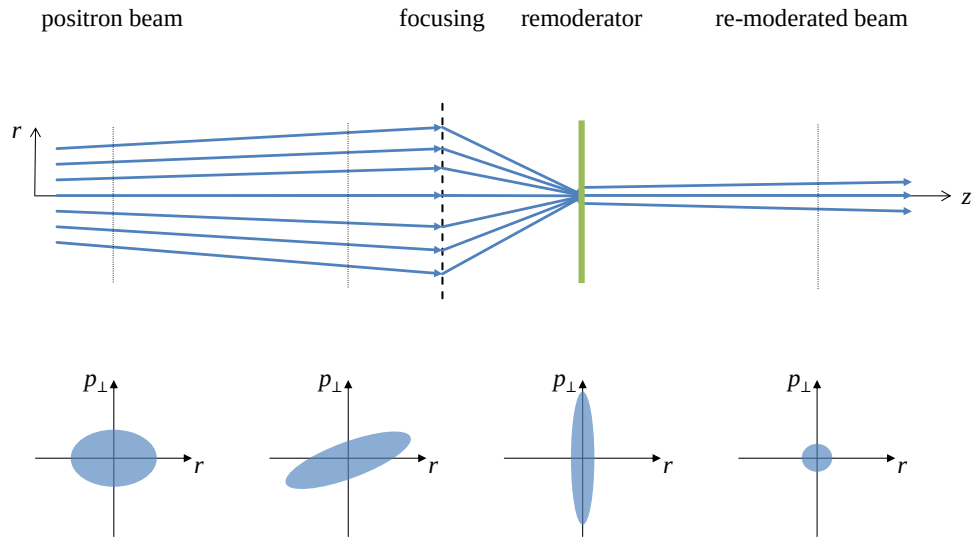

Figure 3.5: The principal of re-moderation: The transverse phase space of the beam is defined by its size and its momentum space. The propagation of the beam leads to a rotation and distortion of the phase space ellipse. The transverse momentum reaches a maximum at the focus position on the remoderator. The re-emitted beam is smaller in size and in divergence angle and therefore higher in brightness.

3.5 Beam Pulsing

If we want to obtain positron lifetime spectra, we have to measure the time between implantation and annihilation. Since we can use the 511 keV annihilation γ as a stop signal, the prompt 1275 keV of ^{22}Na provides the start signal for conventional lifetime spectroscopy. However, a continuous positron beam contains no information about the point in time of implantation. We can solve this problem, if we pulse the beam. Then, positrons will only arrive at a narrow time interval on the sample. If this time interval is small enough, it presents a reasonable start signal for PALS.

In the context of this work, we use two different ways to pulse the NEPOMUC beam: chopping and bunching. Both methods, which own advantageous and disadvantageous, are explained in the following sections.

Note that the positron elevator, explained in Chapter 5, requires a pulsed positron beam. The created pulsed beam, described in this work, has been optimized for a desired operation of the elevator instead of performing PALS. Nevertheless, the pulsed beam will be further compressed in time after the elevator, so that the effort of pulse creation will be advantageous for PALS as well.

3.5.1 Bunching Techniques

The aim of beam pulsing is to bring as much beam intensity as possible in a short time interval. The continuous, re-moderated NEPOMUC beam provides $3.0 \cdot 10^7$ positrons per second. This means that the average time between two positrons is 100 ns. The idea of bunching is to periodically modulate the kinetic energy of every beam particle by a oscillating electric field such that they reach a certain position within a small phase interval of the oscillation. This defines a short time interval of arrival; the 'time focus' modulo the oscillation time.

Prebunching

We can use electric fields to modulate the kinetic energy of positrons, for instance by means of the field between cylindrical electrodes at different potentials. There, the kinetic energy is changed at the gap between the tube. If both electrodes are on a static potential, the velocity of all particles is equal after passing the gap. However, we can

modulate the kinetic energy of every particle differently, if we use dynamic, electric potentials. We show this basic principle of positron beam bunching in Figure 3.6.

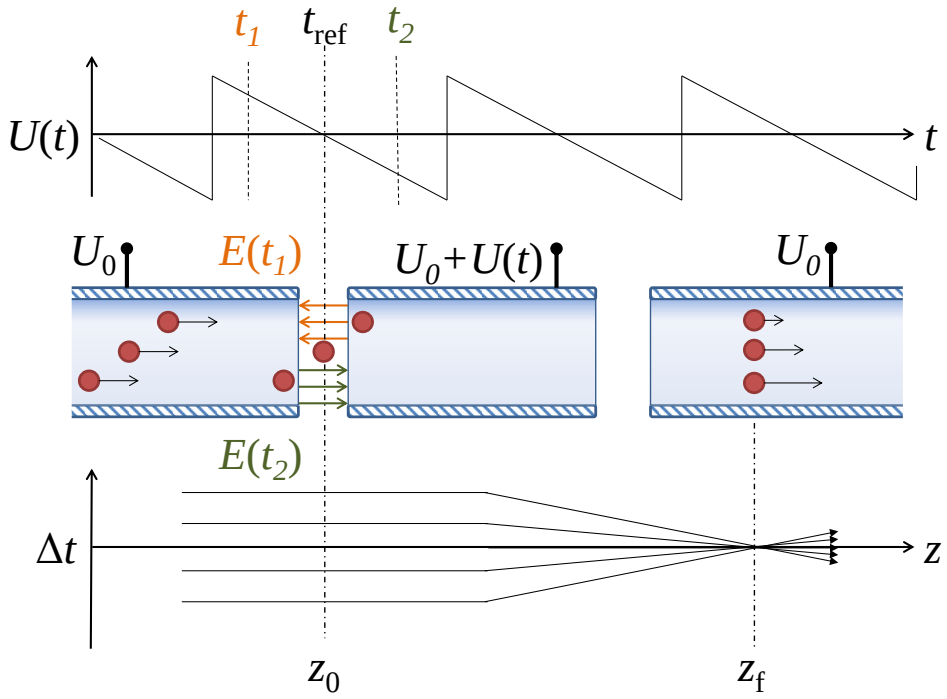

Figure 3.6: The principle of positron beam bunching: The gap between two tube electrodes is field-free for a reference particle at the point in time t_{ref}. Particles before or after this particle are decelerated or accelerated by the electric field $E(t)$, respectively.

The monoenergetic, continuous beam enters a gap between two electrodes. The electric potential of the first electrode stays constant, the potential of the second electrode is changed periodically in time. Therefore, also the electric field at the gap alters in time. The kinetic energy of a beam particle changes, dependent at the point in time when it passes the gap. We can define a reference particle, which enters the gap at t_{ref}, when the gap is field-free. The point in time $t_{\mathrm{ref},z_{\mathrm{f}}}$ when the reference positron appears at position z_{f} is then

$$t_{\mathrm{ref},z_{\mathrm{f}}} = t_{\mathrm{ref}} + t' = t_{\mathrm{ref}} + \frac{L}{v_0} \,. \tag{3.70}$$

In this expression $L = z_\mathrm{f} - z_0$ is the distance between gap and z_f, v_0 is the velocity of the reference particle and t' the time of flight. In general, we can write the velocity of an arbitrary positron after the gap as:

$$v_m = \sqrt{\frac{2e}{m_\mathrm{e}}(U_0 + U(t))} \tag{3.71}$$

The velocity for the reference particle simplifies for $U(t_\mathrm{ref}) = 0$ to

$$v_0 = \sqrt{\frac{2e}{m_\mathrm{e}}U_0}\,, \tag{3.72}$$

where U_0 is the static electric potential. An arbitrary positron reaches position z_f at the point in time $t_{z_\mathrm{f}} = t + L/v_m$. If we want to achieve a time focus at this position, all positron have to appear at the same time:

$$t_{\mathrm{ref},z_\mathrm{f}} = t_{z_\mathrm{f}} \tag{3.74}$$

$$t_\mathrm{ref} + t' = t + t'_m \tag{3.75}$$

$$t_\mathrm{ref} + t' = t + \frac{L}{\sqrt{\frac{2e}{m_\mathrm{e}}(U_0 + U(t))}} \tag{3.76}$$

Here, a positron passes the gap at time t and needs a time t'_m to reach z_f. We can define a time deviation $\Delta t = t - t_\mathrm{ref}$ for a particle, which appears at the gap at another point in time, with respect to the reference particle. Now we write for Equation 3.76

$$t' = \Delta t + \frac{L}{\sqrt{\frac{2e}{m_\mathrm{e}}(U_0 + U(t))}} \tag{3.77}$$

and rearrange it:

$$U(t) = \frac{m_\mathrm{e}}{2e}\left(\frac{L}{t' - \Delta t}\right)^2 - U_0 \tag{3.79}$$

$$= \underbrace{\frac{m_\mathrm{e}}{2e}\left(\frac{L}{t'}\right)^2}_{U_0}\left(\frac{1}{1 - \Delta t/t'}\right)^2 - U_0 \tag{3.80}$$

$$= U_0\left(\left(\frac{1}{1 - \Delta t/t'}\right)^2 - 1\right) \tag{3.81}$$

Assuming that Δt is small with respect to the time of flight t' of the reference positron, this equation simplifies to

$$U(t) \approx 2U_0\frac{\Delta t}{t'} = \sqrt{\frac{8e}{m_\mathrm{e}}}\frac{U_0^{3/2}}{L}t\,. \tag{3.82}$$

We find that $U(t)$ is linear and point-symmetrical to $t = t_\mathrm{ref} = 0$. A periodic sawtooth voltage fits these requirements best. The sawtooth period T determines the repetition rate of the positron pulses. Since the energy modulation leads to different velocities for the positrons, the pulse width will spread after the time focus z_f. We can accelerate the beam at z_f, so that the energy deviation is small with respect to the kinetic beam energy. Therefore, the pulse spreads more slowly.

A serious problem is the exit of the beam from the RF-driven electrode, since there the sawtooth signal de-bunches the beam. In Chapter 4.3.1 the solution for this problem will be presented. A further problem is that commercial waveform generators deliver only amplitudes of a few volts. For higher amplitudes expensive broadband power amplifiers are required. Therefore, we use in practice a sawtooth buncher only to pre-bunch the beam. The next section shows another bunching technique, which overcomes several sawtooth problems. However, this method requires a pre-bunched beam for proper work.

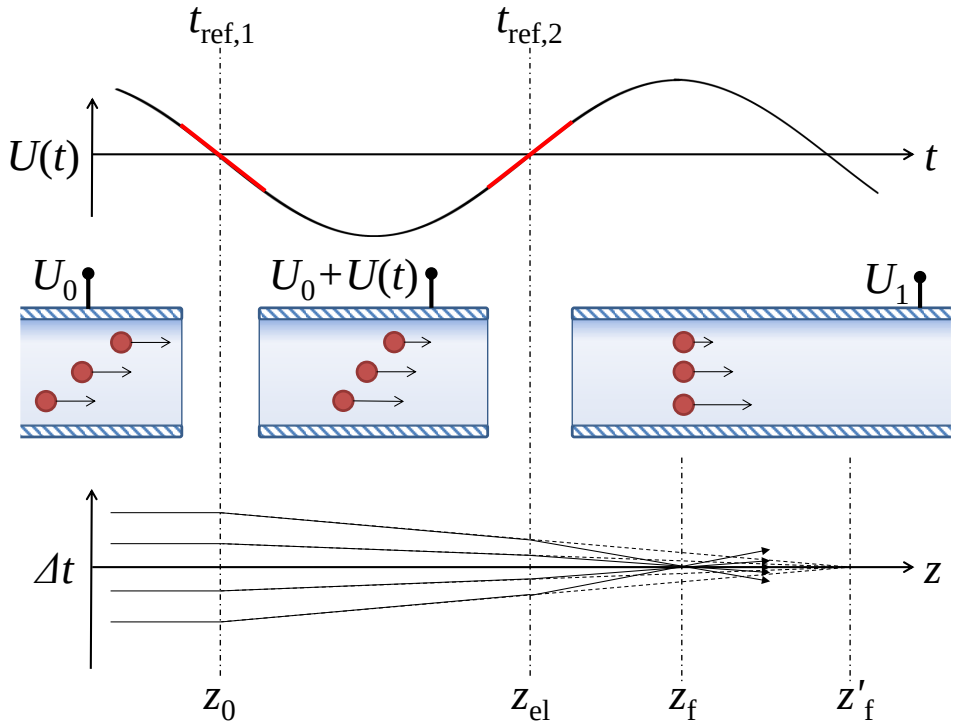

Figure 3.7: Scheme of a sine wave double-gap buncher: We use the sine wave voltage to modulate the kinetic positron energy at both gaps. The time focus is reached at positon z_f. To ensure that we use only the linear part of the sine wave signal (red), the beam is pre-compressed in a prebuncher.

Sine Wave Bunching

The main bunchers of the SPM and the interface are sine wave double-gap bunchers. We present a diagram of the working principle in Figure 3.7. The buncher consists of three electrodes. Entrance and exit electrode are set on a static potential. The voltage of the central electrode $U_0 + U(t)$ alters periodically with a sine wave frequency. The length of this electrode z_{el} is precisely adapted to the kinetic beam energy and the frequency $f = 1/T$:

$$z_{el} = v_0 \frac{T}{2} = \sqrt{\frac{E}{2m_\mathrm{e}}} T \tag{3.83}$$

We adjust the sine wave phase with respect to a reference positron, which passes the first gap at $t_{\mathrm{ref},1}$, so that $U(t_{\mathrm{ref},1}) = 0$. Therefore, the reference positron is neither accelerated nor decelerated. It reaches the second gap after a time

$$t_{\mathrm{ref},2} = t_{\mathrm{ref},1} + \frac{T}{2} \,. \tag{3.84}$$

Then, the sine wave voltage is $U(t_{\mathrm{ref},2}) = 0$ and the positron also passes the second gap without any energy modulation. The velocity of particles before, or after the reference particle, will be changed. The linear part of the sine wave signal leads to an energy modulation similar to a sawtooth voltage. The nonlinear part, however, causes a wrong energy modulation, which increases the pulse background. Therefore, it is necessary to operate the sine wave buncher with a pre-bunched beam that fills only the linear part of the signal.

The advantage of a sine wave double-gap buncher is the energy modulation at both gaps. Whereas the exit gap is a serious problem for sawtooth bunching, we bunch here at both gaps and achieve therefore the time focus z_{f} within a smaller distance. In addition, it is easier to amplify a sine wave voltage by resonance transformation, whereas a sawtooth voltage requires a broadband amplifier. A higher amplitude means that we can achieve short focal lengths z_{f}, or modulate the kinetic energy sufficiently, even at a higher kinetic beam energy.

3.5.2 Beam Chopping

Chopping is a very simple way to imprint a time stamp on a continuous beam. As shown in Figure 3.8, the continuous beam passes a time dependent electric field $E(t)$ between two plates. If the value of this field is zero, the beam is not deflected and can pass an aperture behind the plates. The deflected parts annihilate on the aperture and do not appear in the corresponding time spectra.

We can adjust the pulse widths by altering the electric field. In addition, the beam velocity, the position of the aperture and its diameter affect the pulse shape. It is evident that we lose a lot of beam intensity, if we want to achieve short pulse widths by chopping. Therefore, it is useful to bunch the beam, before it enters the chopper. Then, we can adjust the chopper field $E(t)$ to the pulse frequency and length. In this way, we remove only background positrons from the spectra.

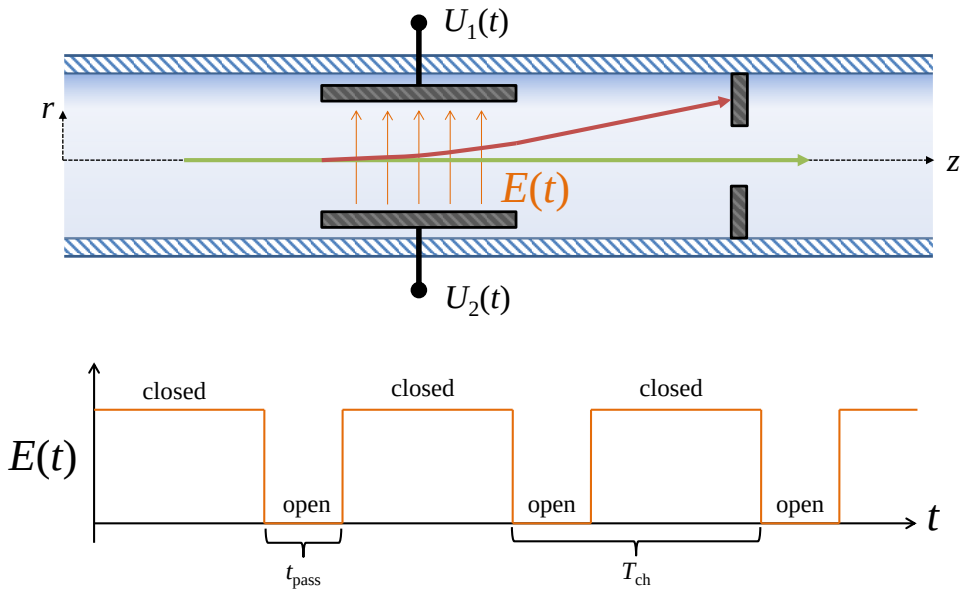

Figure 3.8: Chopping of a pulsed positron beam: The incident pulsed beam enters the chopper plates with an electric field $E(t)$. If the amplitude and the period T_{ch} of this field is adjusted to the pulse width and the passing time t_{pass}, we cut only background positrons out of the time spectra.

3.6 Radio Frequency Perturbation

We discuss in the following subsections the perturbations of radio frequency (RF) electric fields on a pulsed beam with a finite pulse duration $\Delta t_{\text{P}} \neq 0$. Some components of the SPM interface, i.e. buncher, chopper and elevator, use RF fields to change certain beam characteristics. However, these fields can also cause unwanted influences on the beam, which we study in first order perturbation theory.

3.6.1 Perturbation at Nearly Field-Free Gaps

We discuss the positron elevator in detail in Chapter 5. One basic principle is that the pulsed beam has to pass two gaps when they are free of electric fields. However, the time dependent RF field influences the pulses, since they are temporally extended. Figure 3.9 shows two particle trajectories in the x-z plane. The corresponding positrons

pass a gap with an electric field $\vec{E}$. We assume that $\vec{E}$ occurs only close to the gap. Therefore, we can approximate the particle trajectory as a straight line:

$$x(z) = x_0 + \alpha z \tag{3.85}$$

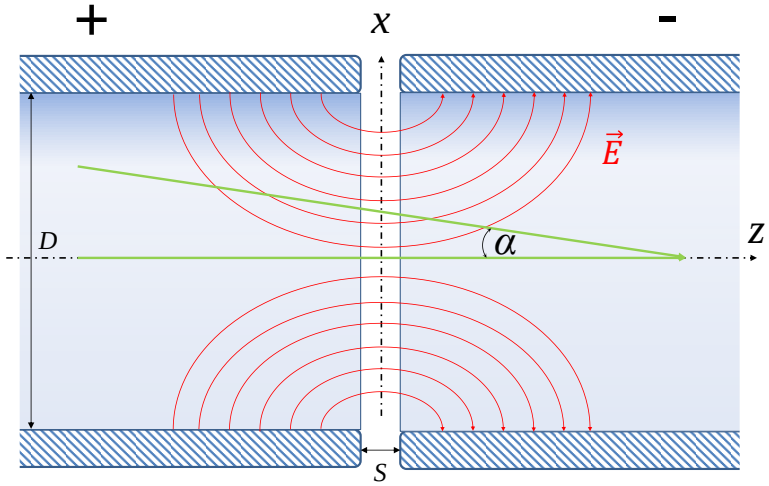

Figure 3.9: Trajectories of positrons at a gap with an electric field $\vec{E}$: Since the particle moves from field-free space into field-free space, we can approximate its trajectory as a straight line.

Furthermore, we can write for the electric field components in x and z direction

$$E_x(t, x, z) = F(t)E_x^0(x, z) \tag{3.86}$$
$$E_z(t, x, z) = F(t)E_z^0(x, z)\ . \tag{3.87}$$

Here $E_x^0(x, z)$ and $E_z^0(x, z)$ are the static electric fields at $t = 0$. If we assume that the gap size is small, with respect to the electrode diameter, and the particles move close to the optical axis z, then we can write for the static field in z direction:

$$E_z^0(x, z) \approx E(z) \tag{3.88}$$

Since the electric field inside the cylinders is source-free, we approximate the field in x direction for a round, rotationally symmetric lense, from the series expansion [63] in lowest order:

$$E_z^0(x,z) \approx -\frac{x}{2}\frac{\partial E(z)}{\partial z} \tag{3.89}$$

We obtain from the general equation of motion $m_\mathrm{e}\vec{\dot{v}} = e\vec{E}$ the velocity change at the gap as

$$\Delta\vec{v} = \frac{e}{m_\mathrm{e}} \int_{t=-\infty}^{t=+\infty} \vec{E}(x(t),z(t),t)\,\mathrm{d}t \tag{3.90}$$

and since $\mathrm{d}t = \mathrm{d}z/v_\parallel$,

$$\Delta\vec{v} = \frac{e}{m_\mathrm{e}} \int_{z=-\infty}^{z=+\infty} \vec{E}(x(z),z,t(z))\frac{\mathrm{d}z}{v_\parallel} \tag{3.91}$$

Here, the velocity $v_\parallel$ of an undisturbed positron stays constant. To calculate the influences of the pulse duration, beam diameter and the beam distance from the optical axis, we have to specify $\vec{E}(x(z),z,t(z))$ completely. Therefore, we determine the time dependent component $F(t)$. The gap is field-free at $t = 0$, when the reference particle passes the gap, so that $F(t=0) = 0$. In addition, $F(t)$ changes periodically with a frequency $\omega = 2\pi f$. The central elevator electrode oscillates between negative and positive amplitude. Therefore, the values of $F(t)$ must change between 0 (gap is field-free) and 2 (central electrode is on exit potential). For these conditions, we can write

$$F(t) = 1 - \cos(\omega(t - t_n)) \,. \tag{3.92}$$

Here, t_n is the time between the reference particle and an arbitrary positron. For sufficiently small $|t - t_n|$, we can approximate the cosine term by a series expansion and write

$$F(t) \approx \frac{\omega^2}{2}(t - t_n)^2 \,. \tag{3.93}$$

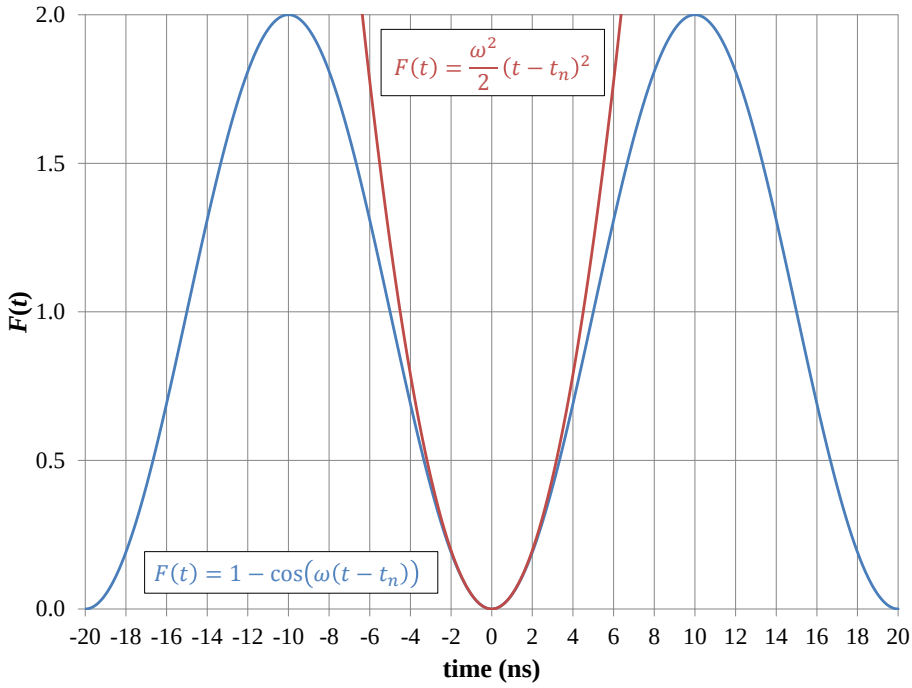

Figure 3.10: Graph of $F(t)$ calculated with $f = 50$ MHz and $t_n = 0$.

Figure 3.10 depicts $F(t)$ and its approximation. With the assumption that the velocity $v_\parallel$ in longitudinal direction stays constant, so that $z(t) = v_\parallel \cdot t$, we obtain

$$F(t) \approx \frac{\omega^2}{2}\left(\frac{z}{v_\parallel} - t_n\right)^2 . \tag{3.94}$$

Putting this in Equation 3.91, we get the velocity changes in z and x direction:

$$\Delta v_z = \frac{e\omega^2}{m_e v_\parallel} \int \left(t_n^2 - 2\, t_n \frac{z}{v_\parallel} + \frac{z^2}{v_\parallel^2} \right) E(z)\, \mathrm{d}z \tag{3.95}$$

$$\Delta v_x = -\frac{e\omega^2}{4 m_e v_\parallel} \int (x_0 + \alpha z) \left(t_n^2 - 2\, t_n \frac{z}{v_\parallel} + \frac{z^2}{v_\parallel^2} \right) \frac{\partial E(z)}{\partial z}\, \mathrm{d}z \tag{3.96}$$

For a symmetric gap, the following symmetry conditions hold [63]:

$$\text{(a)}\quad E(-z) = E(+z) \qquad \text{(b)}\quad \int z \cdot E(z)\,\mathrm{d}z = 0 \tag{3.97}$$
$$\text{(c)}\quad \frac{\partial E(-z)}{\partial z} = -\frac{\partial E(+z)}{\partial z} \qquad \text{(d)}\quad \int z^{2m} \cdot \frac{\partial E(z)}{\partial z}\mathrm{d}z = 0 \qquad (m = 0, 1, 2, ...)$$

Furthermore, the electric field is confined in a range $\pm d/2$ close to the gap , with $d^2 = D^2 + S^2$ [63]. Here, D is the tube diameter and S the gap width and we obtain finally:

$$\text{(a)}\quad \int_{-\frac{d}{2}}^{+\frac{d}{2}} E(z)\,\mathrm{d}z = \Delta U_{\mathrm{stat}} \qquad \text{(b)}\quad \int_{-\frac{d}{2}}^{+\frac{d}{2}} z \cdot \frac{\partial E(z)}{\partial z}\mathrm{d}z = -\Delta U_{\mathrm{stat}} \tag{3.98}$$

In these expressions is ΔU_{stat} the static, electric potential difference between the two cylinder electrodes. Now, we can write for the longitudinal velocity modulation:

$$\Delta v_z = \frac{e\omega^2}{m_{\mathrm{e}} v_\parallel} \left(\Delta U_{\mathrm{stat}}\, t_n^2 + \frac{1}{v_\parallel^2} \int_{-\frac{d}{2}}^{+\frac{d}{2}} z^2 E(z)\,\mathrm{d}z \right) \tag{3.99}$$

We see that the time dependent energy modulation is only zero for an infinitesimal short pulse duration ($t_n \sim \Delta t_{\mathrm{P}} \to 0$). In reality, we can reach negligible influences on the longitudinal velocity modulation, if the pulse duration is short and the gap transition time low, i.e., for a high beam energy and a narrow gap width.

With the same considerations we obtain for the velocity modulation in transverse direction:

$$\Delta v_x = \frac{e\omega^2}{m_{\mathrm{e}} v_\parallel} \cdot \Delta U_{\mathrm{stat}} \cdot \left(\frac{-t_n}{2v_\parallel} \cdot x_0 + \frac{t_n^2}{4} \cdot \alpha - \frac{d^2}{16 v_\parallel^2} \cdot \alpha \right) \tag{3.100}$$

This expression shows that the transverse velocity modulation depends not only on the pulse duration, but on the beam divergence α and the distance x_o from the optical axis z. These results are important for the construction and the desired operation of the positron elevator, since it should only increase the potential beam energy without

any alteration of other beam parameters. Therefore, we have to consider all resulting aspects of this section. We discuss the RF perturbation for the positron elevator on the basis of these calculations in Chapter 5.

3.6.2 Perturbation caused by Transverse Electric Fields

Similar to the previous considerations, we can discuss how transverse electric RF fields affect the beam. The SPM interface generates these fields to operate the chopper unit, according to the principle, explained in Section 3.5.2. Therefore, we use a time dependent voltage, which we apply to the chopper plates with opposite polarity. Figure 3.11 shows a sketch of a simple chopper geometry. The dynamic, electric field between the plates deflects parts of the positron beam on an aperture. We can write for the electric potential:

$$\phi(t,x,z) = F(t) \cdot \phi_0(x,z) = F(t) \cdot \ \widehat{U}\, g(x,z) \tag{3.101}$$

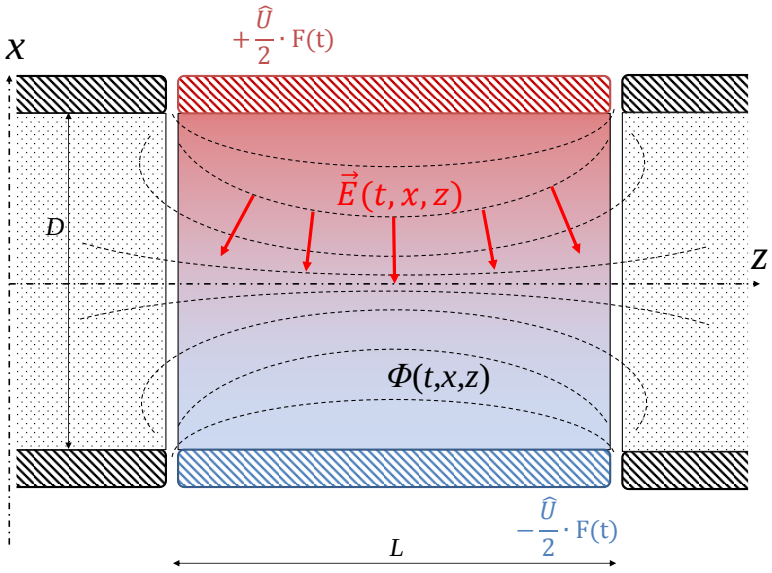

Figure 3.11: Equipotential lines and electric field between two chopper plates: The electric field component in longitudinal direction appears mainly at the edge area. It is zero in the center between the plates.

Here, $\phi_0(x, z)$ is the static electric potential at $t = 0$ and $F(t)$ a time dependent component. Since the longitudinal velocity $v_\parallel$ stays approximately constant for each particle, we can determine the transition time t_{tr} as:

$$t_{\mathrm{tr}} = \frac{L}{v_\parallel} \tag{3.102}$$

This means that a particle, which is at t_0 in the center, enters the space between the plates at $t_0 - t_{\mathrm{tr}}/2$ and leaves it at $t_0 + t_{\mathrm{tr}}/2$. We see in Figure 3.11 that a longitudinal electric field E_z appears mainly at the edge area. To first order, the energy modulation in longitudinal direction is:

$$\Delta E \approx e\,\frac{x}{D} \cdot \widehat{U} \cdot [\; F(t + t_{\mathrm{tr}}/2) - F(t - t_{\mathrm{tr}}/2) \;] \tag{3.103}$$

Figure 3.12 shows a realistic graph for $F(t)$. The function is zero at $t = 0$ and one for the time $t < t_{\mathrm{g}}/2$ and $t > t_{\mathrm{g}}/2$. In between, its shape is nonlinear. If the transition time t_{tr} is small with respect to t_{g}, we can do a second-order approximation for $F(t)$:

$$F(t) \approx \left(\frac{2}{t_{\mathrm{g}}} \cdot t\right)^2 \tag{3.104}$$

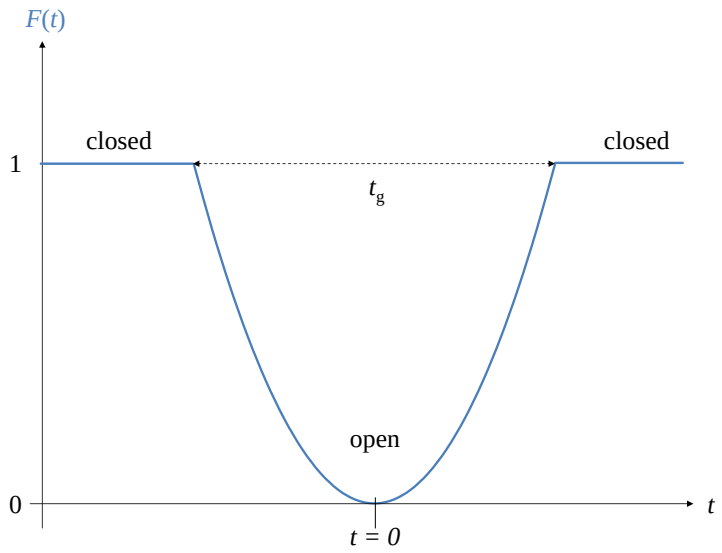

Figure 3.12: Graph of $F(t)$.

In combination with Equation 3.103 we obtain:

$$\Delta E \approx e\,\frac{x}{D}\cdot\widehat{U}\cdot\frac{8\,t\cdot t_{\mathrm{tr}}}{t_{\mathrm{g}}^2} \tag{3.105}$$

This means that the energy modulation is positive for $x \cdot t > 0$ and negative for $x \cdot t < 0$. Therefore, the part of the beam above the symmetry plane is bunched, whereas the part below is de-bunched. This means that the chopper disturbs the time structure of the beam. Furthermore, since the chopper deflects the beam in negative x direction, a greater part of the de-bunched part annihilates on the aperture, compared to the bunched part of the beam. We present a diagram of this effect in Figure 3.13. This effect leads to a bunching behavior of the chopper. On the basis of these results, we can comprehend the time spectra of the SPM interface chopper in Chapter 4.3.1.

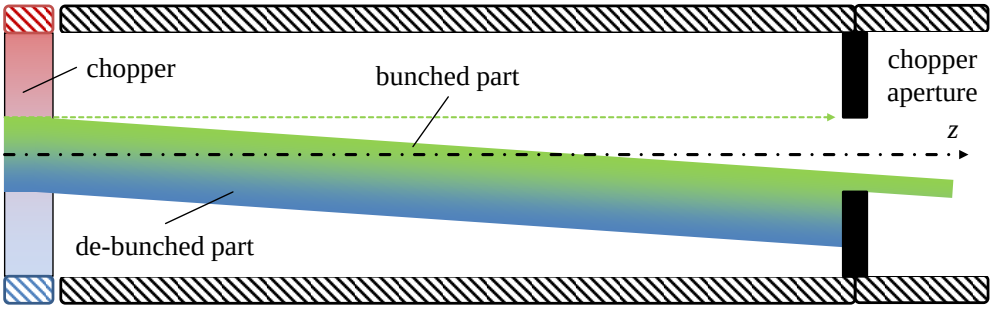

Figure 3.13: Bunching behavior of a chopper: The electric field between the chopper plates deflects parts of the beam on the aperture. The energy modulation below the z axis is negative, whereas it is positive above the axis. Since more positrons of the lower part annihilate on the aperture, the chopper bunches the beam.

3.7 Limits of the Lateral Resolution

We discussed in the previous sections the principles, how to create pulsed positron microbeam with the goal to perform spatially resolved PALS. In contrast to electron beams, a positron microbeam can only be created by several re-moderation steps, which increase the beam brightness. However, the dynamic electric fields, which are necessary for beam pulsing, decrease the brightness, since they increase the transverse momentum of the positrons. In Section 3.3.3 we calculated a minimum feasible beam spot size for an arbitrary beam, using an electrical or magnetic lens system. Nevertheless, this minimum spot is not the only limitation for the lateral resolution of spatial resolved PALS.

The beam focus is always broadened after implantation by scattering and diffusion. According to [80] and [27], we are able to approximate a minimum area of diameter d_{tot} in a sample, where most of the positrons annihilate:

$$d_{\mathrm{tot}} \approx \sqrt{d_{\mathrm{min}}^2 + 1.5\bar{z}^2 + \frac{4 \cdot D_+ \cdot \tau_{\mathrm{b}}}{1 + \tau_{\mathrm{b}} \cdot \kappa \cdot c_{\mathrm{def}} + D_+ \cdot \tau_{\mathrm{b}} / \bar{z}^2}} \tag{3.106}$$

In this expression is $\kappa \cdot c_{\mathrm{def}}$ the total trapping rate, τ_{b} the bulk lifetime $\bar{z}$ the mean implantation depth. The diffusion length D_+ is a material dependent parameter, which is in the range of 0.1 - 1 cm^2/s for metals [7]. The implantation depth $\bar{z}$ below the surface is also material dependent and usually scales with $\approx E^{1.6}$. We find a selection of calculated implantation depth $\bar{z}$ for implantation energies between 2 and 18 keV in Chapter 2.2.1, Table 2.2. There, the values for $\bar{z}$ reach from ≈ 10 nm to 3.3 µm. As a result of this, we find that the resolution is always inferior than the focus size d_{min}. Even for a negligible d_{min} it is determined by $\bar{z}$ [81].

4 The SPM Interface at NEPOMUC

In Chapter 2.6, we discussed the SPM setup and the capabilities of spatially resolved PALS for modern material science. At the moment, the insufficient positron yield of the ^{22}Na source, entailing a low count rate, is the main constraint for a proper operation of the SPM. To overcome this limitation, we will connect the SPM to the reactor-based positron source NEPOMUC. To meet the stringent requirements of the microscope, the SPM interface, which converts the NEPOMUC beam into a pulsed beam of higher brightness, was built in the context of a previous PhD work. After a first test cycle, the interface has been dismantled and stored. We re-assembled the whole device again and improved several parts. In this chapter, we describe the hardware and software components and show measurement results of the renewed system, which pulses the beam and increases its brightness by two orders of magnitude. Additionally, we characterize the beam with a specially constructed sample chamber. It has been possible for the first time to perform spatially resolved PALS at the FRM II. Furthermore, we have used the setup in combination with two newly developed detectors that enabled us to measure first four-dimensional positron age momentum correlation (4D AMOC) spectra.

4.1 The NEPOMUC Source

The worlds most intense low-energy positron beam is generated by the positron source NEPOMUC at the research reactor FRM II. After its implementation in summer 2004, it reached a yield of $1 \cdot 10^8$ slow positrons per second [82]. The NEPOMUC upgrade in 2011 increased the yield to $1.14 \cdot 10^9$ positrons per second [83]. Table 4.1 compares the characteristics of the NEPOMUC beam and a ^{22}Na-based laboratory beam in.

At NEPOMUC the underlying process of positron creation is pair production. The beam tube head is mounted inside the FRM II neutron moderator tank, close to the fuel element and surrounded by heavy water. It includes a ^{113}Cd cap, which acts as a n-γ converter, based on the nuclear reaction ^{113}Cd(n,γ)^{114}Cd. Figure 4.1 shows the neutron

	^{22}Na based	NEPOMUC	
	beam	primary	re-moderated
I (e^+/s)	$2 \cdot 10^5$	$1.14 \cdot 10^9$	$3.0 \cdot 10^7$
d (mm)	3	9.3	1.85
$E_\perp$ (eV)	0.1	50	1
B ($e^+/(mm^2 eVs)$)	$4.4 \cdot 10^5$	$5.3 \cdot 10^5$	$1.8 \cdot 10^7$

Table 4.1: Main characteristics of a laboratory beam, based on a 6 mCi ^{22}Na source, and NEPOMUC: The data are taken from [39,83,84]. The laboratory beam was constructed by the NEPOMUC group at the Technische Universität München. The values for the diameter d and $E_\perp$ are FWHM values. The brightness B is calculated with Equation 3.60 (Chapter 3.4).

capture cross section of ^{113}Cd. The nuclear reaction releases binding energy as hard γ-radiation that hits a subsequent structure of Pt foils, where positron-electron pairs are created. Since the positron work function of Pt is negative, it moderates the positrons directly after creation [85]. We present a technical drawing of the NEPOMUC source in Figure 4.2.

We call the beam, which is created by the NEPOMUC source, NEPOMUC primary beam. It is extracted by electrostatic and magnetic fields and enters the subsequent NEPOMUC beam line. By means of a beam switch, the positrons are delivered to the experiments, connected with NEPOMUC. However, most of the instruments use the brightness enhanced, re-moderated NEPOMUC beam [85]. It is created in a re-moderation unit, between source and beam switch, shown in Figure 4.3.

At the moment, NEPOMUC provides positrons for three permanently operated experiments. In addition, the facility is equipped with an open beam port for temporary experiments. The NEPOMUC beam line is biased on ground potential and transports the beam adiabatically in a magnetic field of about 4 mT. The kinetic energy of the re-moderated beam is E = 20 eV, with an energy spread of $E_\perp$ = 1 eV.

Figure 4.4 presents an overview of the NEPOMUC facility. The SPM will be the fourth permanently operated spectrometer at NEPOMUC. We find in Table 4.1 that the brightness of the NEPOMUC primary beam is in the same order of magnitude than the laboratory beam. However, this is caused by the high intensity of NEPOMUC. Since the SPM has been operated with a ^{22}Na beam, it requires a maximum $E_\perp$ in the range of 100 meV. Thus, the SPM interface is equipped with an additional re-moderation unit,

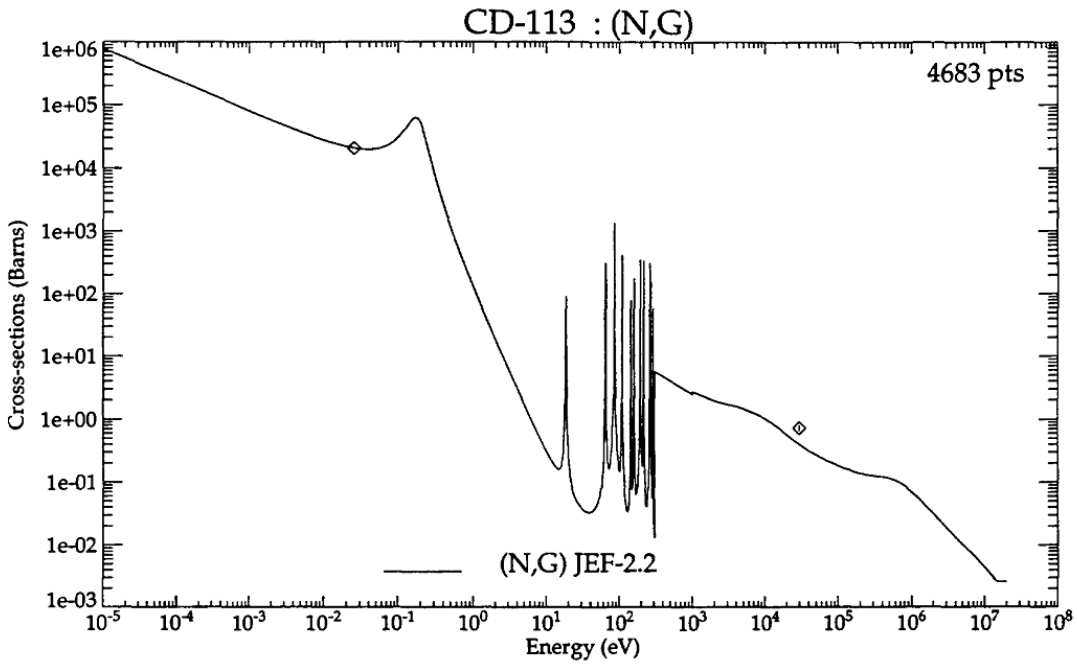

Figure 4.1: Neutron capture cross section of ^{113}Cd: The diagram is taken from [86]. The capture cross section for thermal neutrons amounts to between 10^4 and 10^5 barns. After the nuclear reaction ^{113}Cd(n,γ)^{114}Cd, the neutron binding energy of 9.05 MeV is released as γ-radiation, where an average of 2.3 γ-quanta own more than 1.5 MeV energy per capture neutron [87].

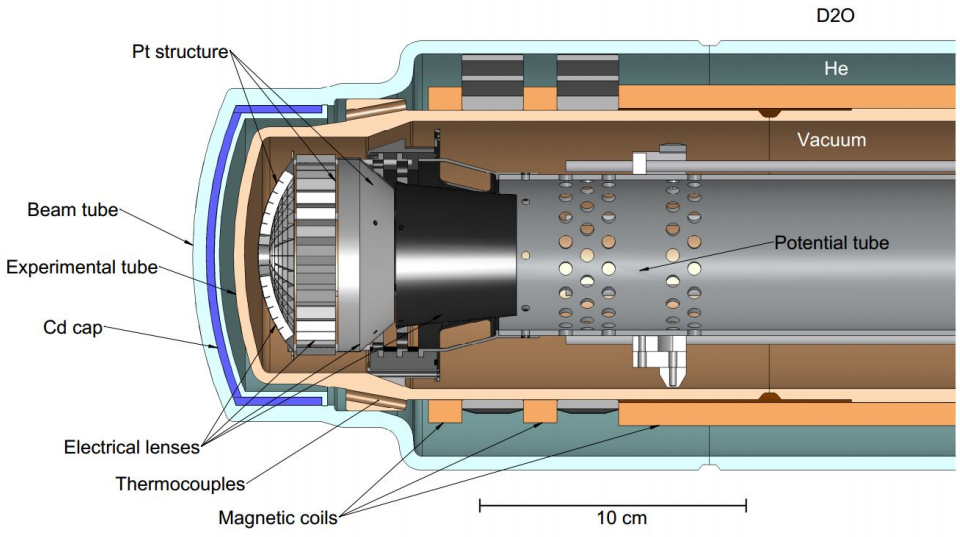

Figure 4.2: Technical drawing of the in-pile positron source NEPOMUC [88]: Thermal neutrons from the FRM II are captured in the ^{113}Cd-cap. The released hard γ-radiation leads to pair production in the subsequent Pt structure. Electrons and positrons are separated due to their charge by electrical and magnetic fields.

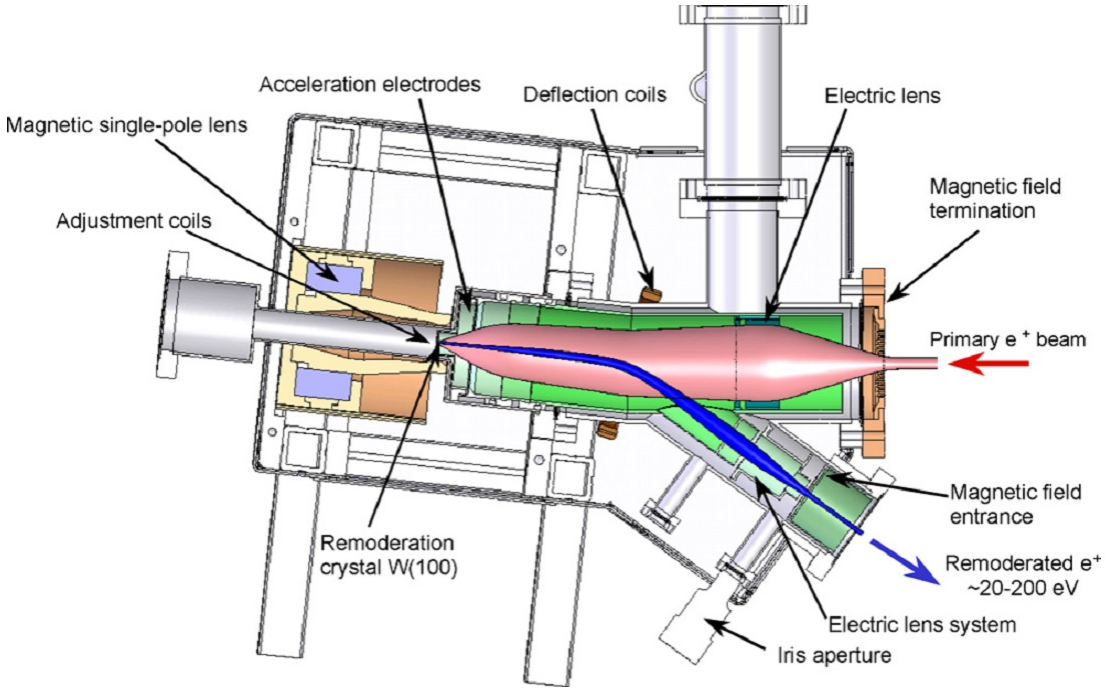

Figure 4.3: Sketch of the NEPOMUC re-moderation unit [89]: The NEPOMUC primary beam enters the device at the magnetic field terminator and is henceforth transported electrostatically to the remoderator crystal. A composition of lenses focuses the beam with an kinetic energy of $\approx$ 1 keV on the surface of a W(100) single crystal. The re-moderated beam's lower energy allows to separate it from the primary beam by deflection coils. After leaving the field-free space, the beam re-enters the NEPOMUC beam line.

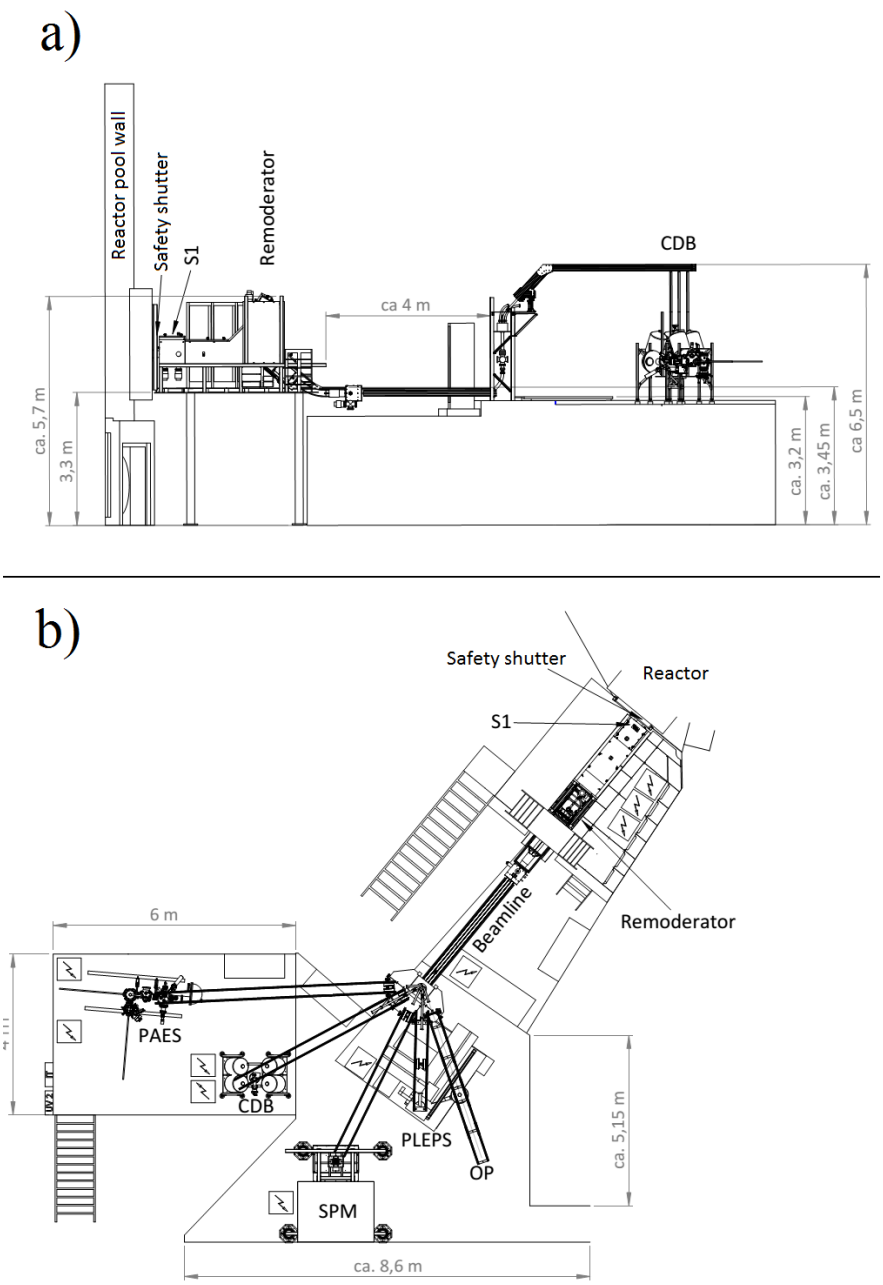

Figure 4.4: Side view a) and top view b) of the NEPOMUC facility [90]: The in-pile positron source is mounted behind the reactor pool wall. The primary beam passes the safety shutter and is either re-moderated, or directly fed in one of the connected experiments:
CDB (Coincident Doppler Broadening Spectroscope), OP (Open Port), PAES (Positron induced Auger Electron Spectroscope), PLEPS (Pulsed Low-Energy Positron System), SPM (Scanning Positron Microscope)

which increases the transverse phase space density, in order to fulfill the SPM requirements.

4.2 Measurement Electronics

4.2.1 Detection

We detect the annihilation radiation with a BaF_2 scintillator crystal, coupled on a *Photonis - XP 2020 URQ* photomultiplier with 12 dynodes. The crystal is pyramidal shaped with a height of 35 mm and an average diameter of 42.5 mm. We pick the signal from dynode 6 to obtain the γ-energy and use the signal from dynode 9 for timing. For this, we apply a base circuit that was developed at the *Institut für angewandte Physik und Messtechnik - LRT2* at the Universität der Bundeswehr. P. Sperr and U. Ackermann et al. present a detailed characterization of the whole detector system and a comparison with other detectors in [91] and [92]. For all measurements the same detector system is used, unless otherwise specified. The time resolution of the detector has been determined, as described in [92], as $\Delta t_{\mathrm{D}} = 230$ ps FWHM.

4.2.2 Data Acquisition and Processing

Figure 4.5 depicts a diagram of the electronic measurement and acquisition components. The core of this structure is a 50 MHz sine wave oscillator, which synchronizes the whole system. Since all timing components are driven by this frequency, we obtain time spectra in a window of 20 ns.

The time resolution of the complete system Δt_{T} is correlated with the detector resolution Δt_{D} and the pulse width Δt_{P} of the system. In a first approximation we consider Δt_{D} and Δt_{P} as the FWHM values of Gaussian-shaped distributions. To obtain the total time resolution, we can sum up the squares:

$$\Delta t_{\mathrm{T}}^2 = \Delta t_{\mathrm{D}}^2 + \Delta t_{\mathrm{P}}^2 \tag{4.1}$$

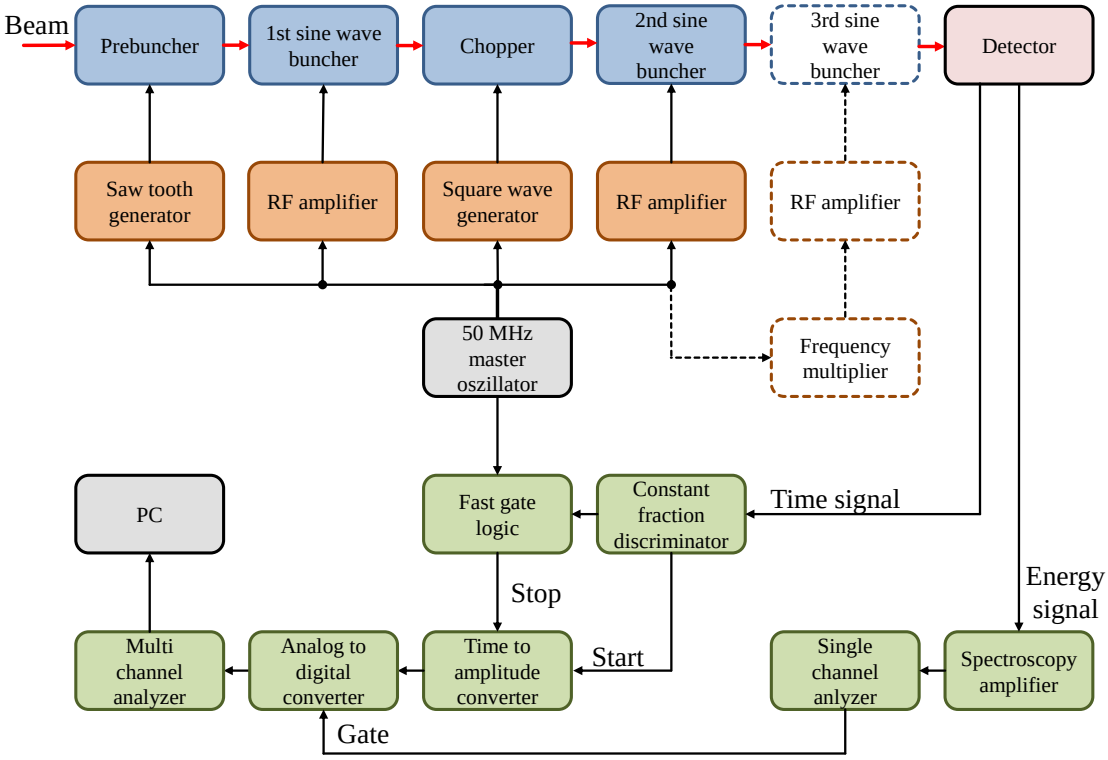

Figure 4.5: Diagram of the SPM and SPM interface measurement and acquisition components: A 50 MHz master oscillator synchronizes the pulsing electronics (orange) that themselves control the pulsing components (blue). To obtain time spectra, the detector signals are processed by nuclear electronics (green), which are also synchronized by the 50-MHz-clock. The components framed with the dashed lines are forseen for the SPM. Special components are explained in [93].

Evidently, the detector count rate C scales with the number of annihilating positrons I. In general, it is a function of the detector efficiency η_{det} and the measurement geometry:

$$C = 2I \cdot \eta_{\mathrm{det}} \cdot \mu \cdot \frac{\Omega}{4\pi} \,, \tag{4.2}$$

In this expression, Ω is the solid angle between detector and annihilation target and μ is the absorption coefficient for 511 keV γ-radiation of matter within Ω. The factor 2 originates from the annihilation in two γs per positron.

4.3 Beam Preparation

In the previous sections we mentioned the necessity to improve the quality of the NEPOMUC beam, in order to operate the SPM at the FRM II. For that purpose, C. Piochacz build the SPM interface in the context of his PhD work [94]. A labeled drawing of the interface can be seen in Figure 4.6. It includes an additional re-moderation stage to enhance the beam brightness. Additionally, the interface pulses the continuous beam with several bunching and chopping units. Up to the first sine wave buncher, the beam is transported adiabatically. Afterwards, it passes a magnetic field terminator and is after this transported electrostatically. Figure 4.7 depicts a diagram, where the treatment of the beam is shown from source to sample. Since the interface was dismantled and stored after a first test cycle, we rebuilt it and improved some components. One of those is a cylinder lens at the interface entrance, which can be used to analyze the longitudinal velocity distribution of the beam and, thus, the distribution of E. To this end, we bias this lens on a retarding potential and measure the beam intensity at the end of the interface as a function of the electric potential. Figure 4.8 shows the corresponding energy distribution of the NEPOMUC beam.

The purpose of the interface is not just to enhance the beam brightness by several orders of magnitude, but also to achieve preferably short pulse lengths. Additionally, we have to minimize the positron losses inside the system, in order to reach a high beam intensity for the microscope.

In addition, the SPM operation at the FRM II differs totally from the laboratory. The beam time with NEPOMUC is restricted and depends on the reactor cycles. Therefore, we have to transport the beam through the whole system in every new measurement

period again. Adjusting all parameters per hand would cost a lot of rare beam time. To overcome this, we programmed a new software, based on a special algorithm, which optimizes the beam transport automatically.

Figure 4.7 reveals as well some promising targets for improvements beyond the present work. For instance, if the efficiency of the first remoderator is increased to the one of the second remoderator and the spread of $E_{\perp}$ is reduced simultaneously to 100 meV, then the intensity will grow by a factor of about 10 and the final spot size decrease by a factor of 3.

4.3.1 The Pulsing System

The SPM interface pulsing system consists of a sawtooth prebuncher, two sine wave bunchers and a chopper unit. All components are driven at a working frequency of 50 MHz. With the help of this pulsing system we achieve short pulse lengths of several hundred picoseconds FWHM, enabling us to perform PALS with the microscope. Furthermore, a proper operation of the positron elevator requires short beam pulses.

The Prebuncher

After entering the SPM interface, the continuous beam is prebunched by a 50 MHz sawtooth-shaped voltage. We present a technical drawing of the prebuncher in Figure 4.9. It consists of five buncher electrodes, a drift tube and two acceleration electrodes. We mention in Chapter 3.5.1 that the exit of the beam from the sawtooth-driven electrode is a serious problem of all prebunchers. To overcome this, we apply the sawtooth voltage to a resistor network, which is connected to the buncher electrodes. The kinetic energy of the beam is modulated at the first buncher gap, where the full sawtooth voltage drops. In the second gap, the sawtooth voltage drops linearly over four electrodes, so that the force on the positrons depends only on time: $\mathrm{e} \cdot E(z,t) = \mathrm{e} \cdot E(t)$; and not on the position within the gap. Since the transit time through the four electrodes amounts to a full RF period (20 ns), the total energy transfer on the positrons will be zero, independently of the phase [39,94]. Adjusting all parameters correctly, we achieve the time focus close to the acceleration electrodes, where the kinetic beam energy is increased and the pulse spreads slower.

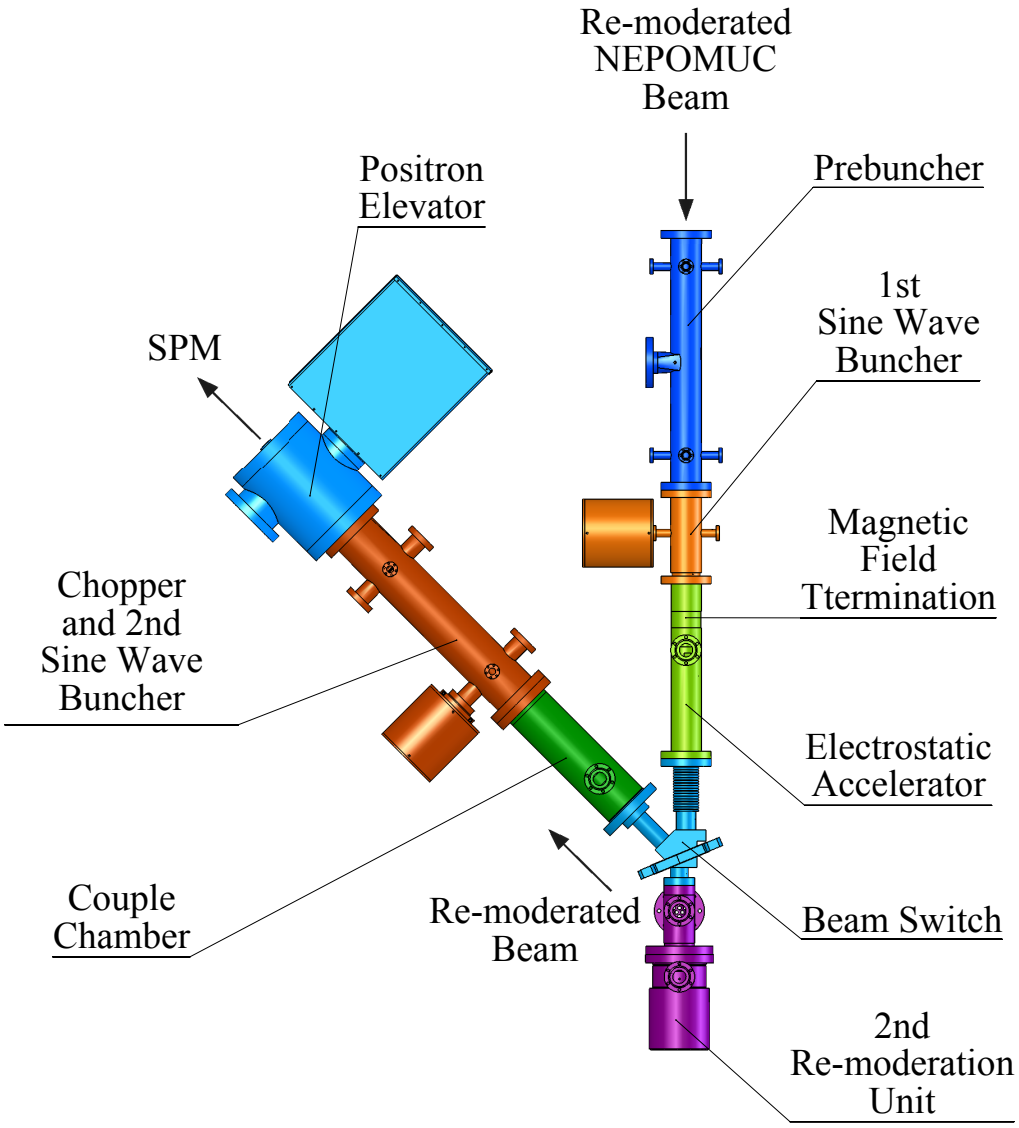

Figure 4.6: The SPM interface at NEPOMUC: The interface pulses the continuous, re-moderated NEPOMUC beam with a sawtooth buncher and two sine wave bunchers. The positron background is reduced by a chopper unit. An additional re-moderation stage increases the beam brightness. The beam switch separates the incident beam from the re-moderated beam. The last component is the energy elevator, which increases the potential beam energy by several keV.

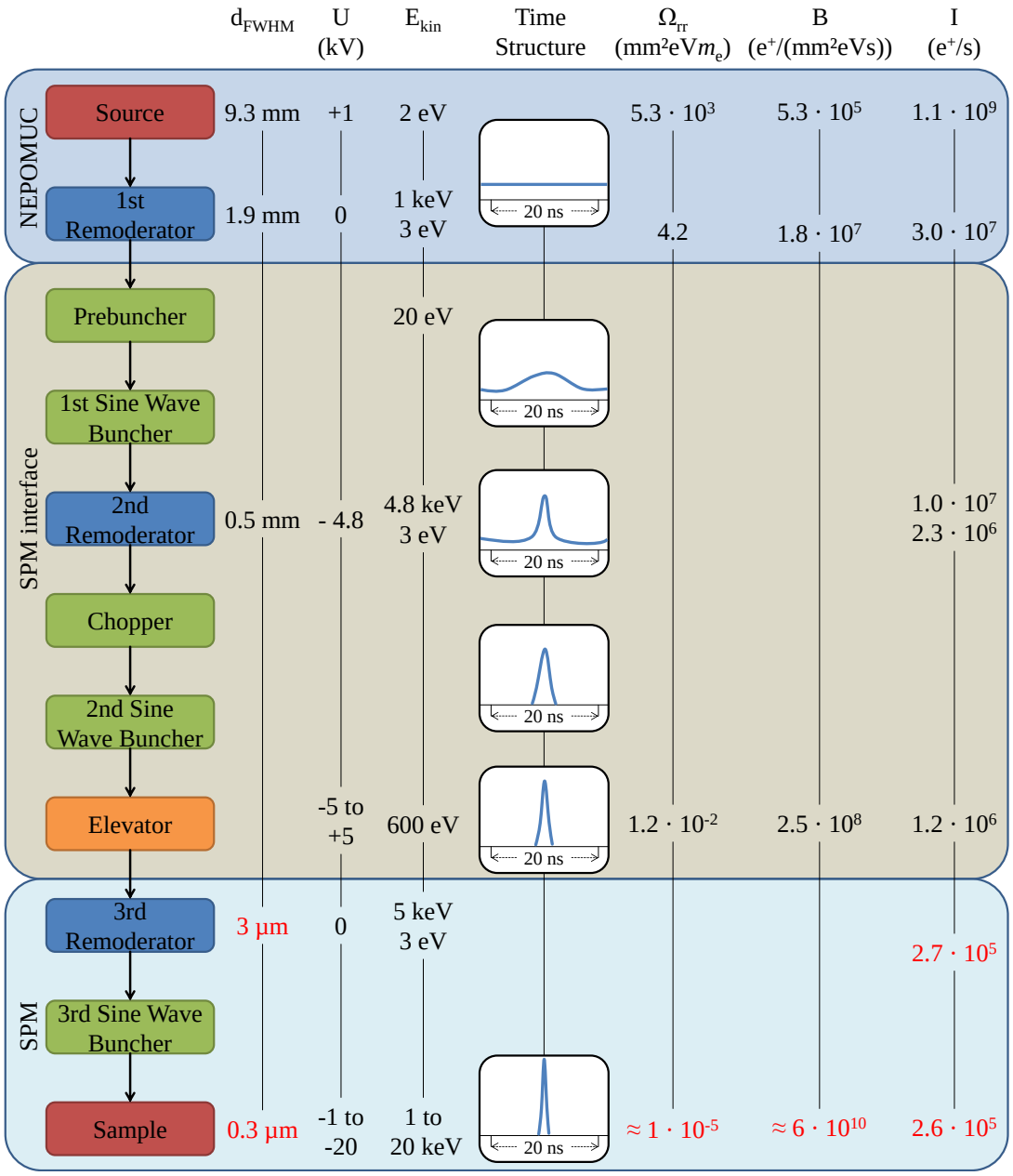

Figure 4.7: Beam preparation from source to sample: The NEPOMUC beam is re-moderated (blue) for three times, in order to reach a beam spot size in the µm-range at the sample position of the SPM. Since every re-moderation step entails a loss of several keV total beam energy, the elevator (orange) must increase the potential beam energy without altering other beam parameters. To operate the elevator properly, the SPM interface pulses the continuous beam (green components). The buncher of the SPM further compresses this pulse length in order to perform PALS. Expected values, which are predicted from measurements (see Chapter 5) are written in red.

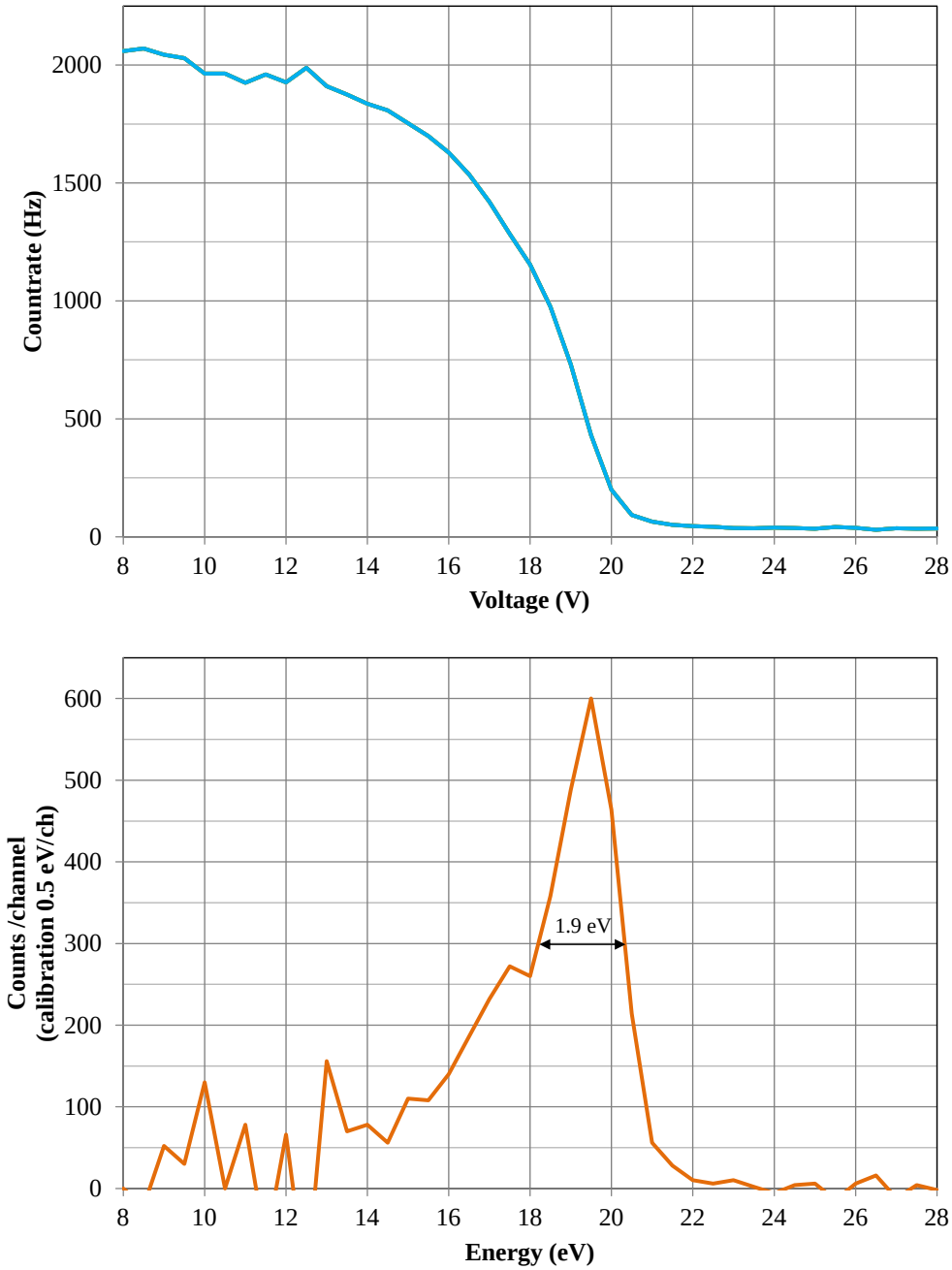

Figure 4.8: Energy distribution of the re-moderated NEPOMUC beam at the entrance of the SPM interface: For this measurement we increased a retarding field progressively at the entrance and observed the beam intensity (blue). We obtain the energy distribution (orange) by a numerical derivation and calculate the width by a Gaussian fit as 1.9 eV FWHM.

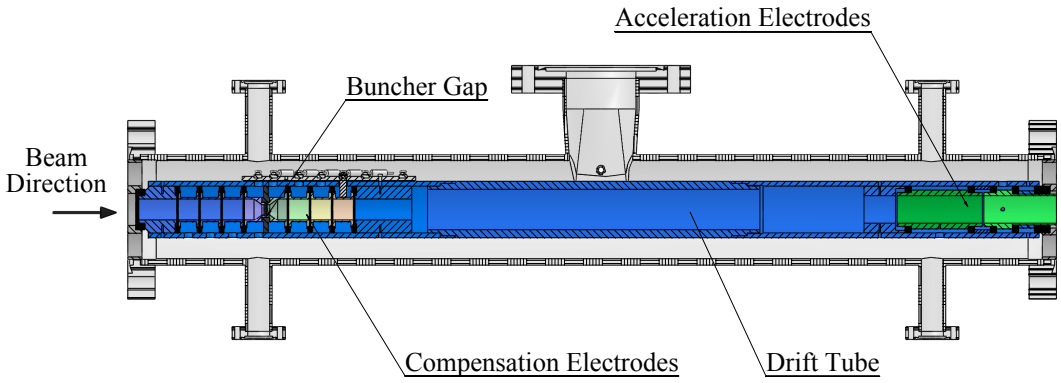

Figure 4.9: The sawtooth prebuncher: The incident beam passes the buncher gap, which modulates the kinetic energy by a dynamic, electric field of 50 MHz. To avoid an additional energy modulation at the exit gap, the sawtooth voltage is split on four electrodes. After a drift, two electrodes accelerate the beam, to reduce a pulse spread.

To characterize the electric field at the buncher gap, we measured the induction in a single-winding coil at different frequencies. The prebuncher shows a strong low-pass behavior for some frequency ranges, shown in Figure 4.10. Therefore, the applied sawtooth voltage, which consists of various frequencies, is distorted at the gap. To overcome this problem, we use a *Keysight 81160A Pulse Function Arbitrary Generator*, which enables to modify the sawtooth signal. We optimized the signal shape to receive an almost sawtooth-shaped voltage at the buncher gap. With this signal and an amplitude of 5 V, we achieve a minimum pulse duration of 3.9 ns FWHM. Figure 4.11 depicts the corresponding time spectrum.

The 1st and 2nd Sine Wave Buncher

The SPM interface contains two sine wave bunchers of almost identical design. Figure 4.12 depicts a technical drawing of the first one. Both devices are double-gap bunchers and work according to the principle, explained in Chapter 3.5.1. The length of the central electrode is 120 mm. Therefore, incident positrons must have a kinetic energy of 410 eV to pass the central electrode within a half period (10 ns). We feed the RF (Radio Frequency) voltage inductively by a coupling coil at the front side of the resonator coil. The central electrode and the resonator coil form a RLC circuit, adjusted for a resonance frequency of 50 MHz to amplify the sine wave signal. The resonator amplitude can be varied by adjusting the coupled voltage. Figure 4.13 shows the corresponding time

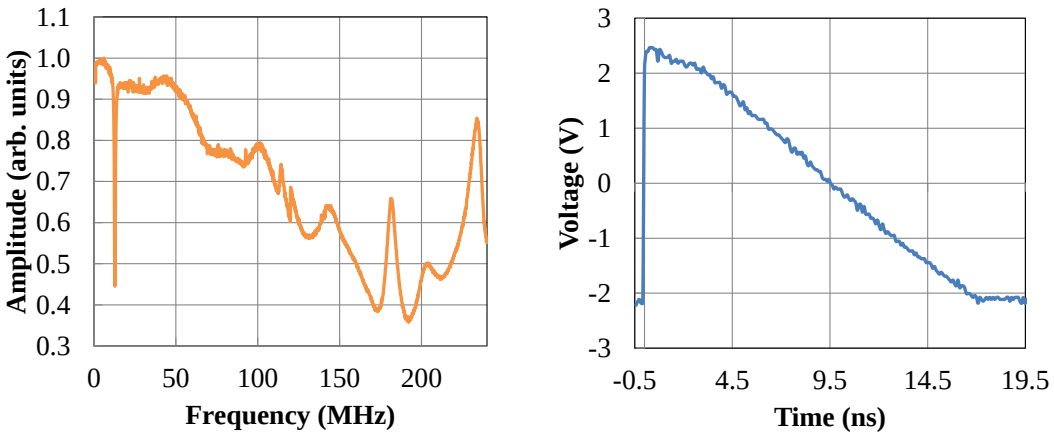

Figure 4.10: Left: Frequency depending sine wave amplitude, measured by the induction in a single-winding wire at the buncher gap. Right: Experimentally found, adapted sawtooth signal, leading to a sawtooth-shaped voltage at the gap.

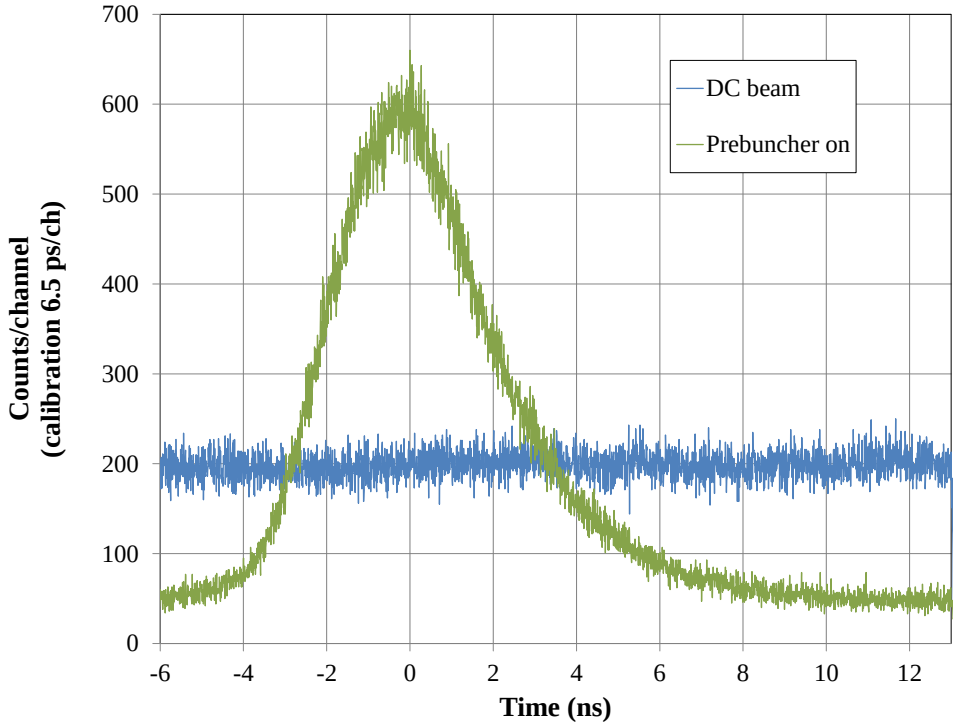

Figure 4.11: Time spectra of the continuous and prebunched beam: We achieve a pulse duration of $\Delta t_{\mathrm{P}} = 3.9$ ns FWHM and a peak to background ratio of Λ_{PBR} = 5:1. To obtain this spectrum, we apply the voltage signal that is shown in Figure 4.10. The measurement time of both spectra is 300 s.

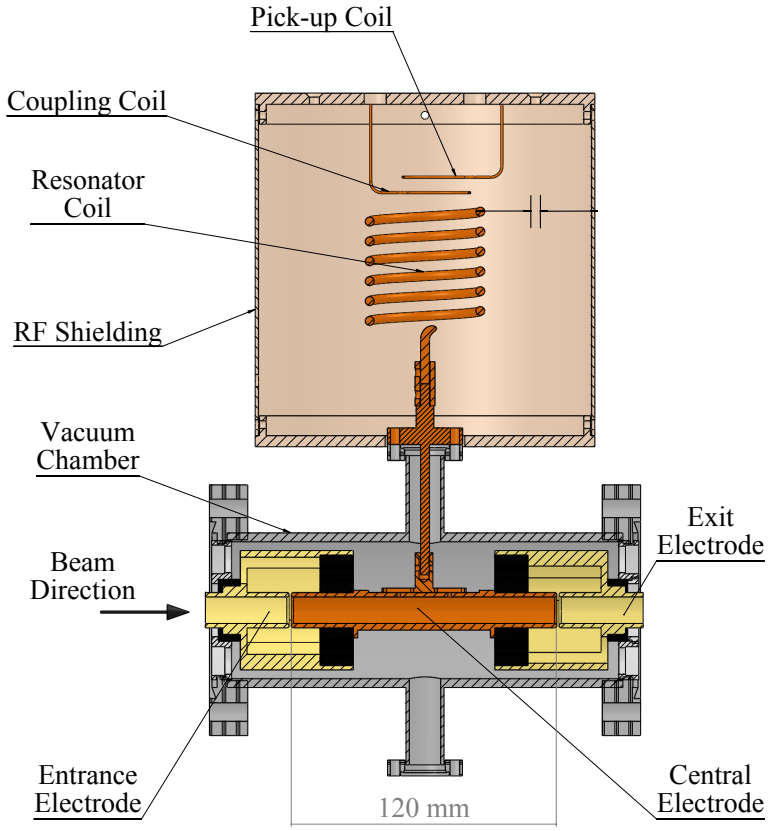

Figure 4.12: The first sine wave buncher of the SPM interface: The resonator coil and the central electrode form a RLC circuit, which amplifies the coupled 50 MHz sine wave voltage. Positrons with a kinetic energy of 410 eV need 10 ns (half signal period) to pass the 120 mm long central electrode.

spectrum. For a pre-bunched beam, the pulse width decreases while the pulse height doubles.

We present the time spectrum of the second sine wave buncher in Figure 4.14. Feeding the buncher with the continuous beam, a pulse duration of $\Delta t_{\mathrm{P}} = 640$ ps FWHM is obtained. The results of the first and the second buncher differ from each other, although their working principle and design is equivalent. However, we have to consider that the beam is re-moderated between these two components. The reduction of ΔE and the smaller transverse phase space of the re-moderated beam lead to better results.

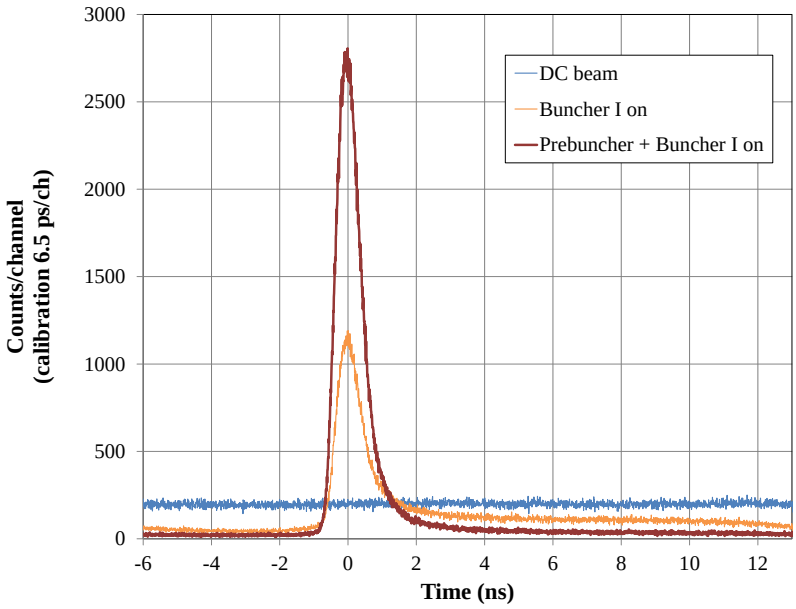

Figure 4.13: Time spectra of the first sine wave buncher: The buncher pulses the continuous beam to pulse widths of $\Delta t_{\mathrm{P}} \approx 880$ ps FWHM. With the prebunched beam we achieve pulse widths of less than 800 ps and a peak to background ratio of $\Lambda_{\mathrm{PBR}} =$ 155:1. Each spectrum is measured for 300 s.

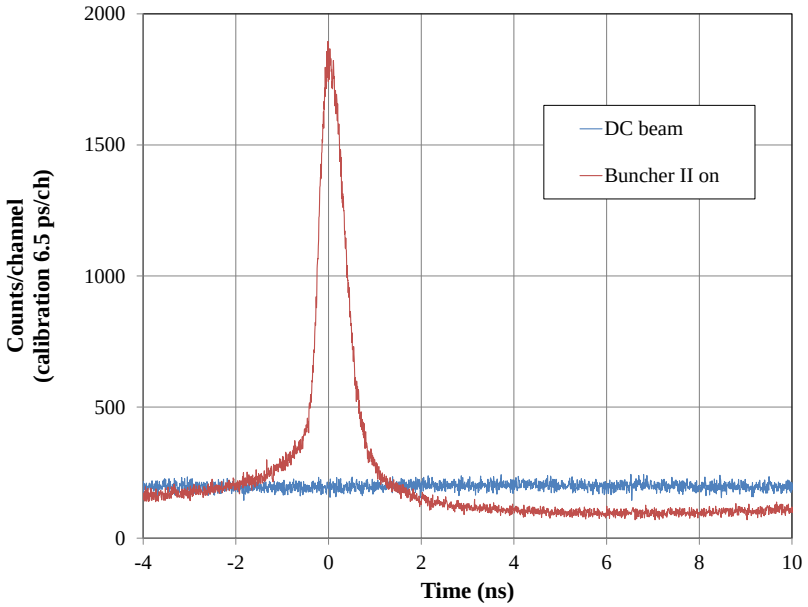

Figure 4.14: Time spectra of the second sine wave buncher, compared to the continuous beam: We achieve pulse widths of $\Delta t_{\mathrm{P}} < 640$ ps FWHM and a peak to background ratio of $\Lambda_{\mathrm{PBR}} =$ of 22:1. We measured both spectra for 300 s.

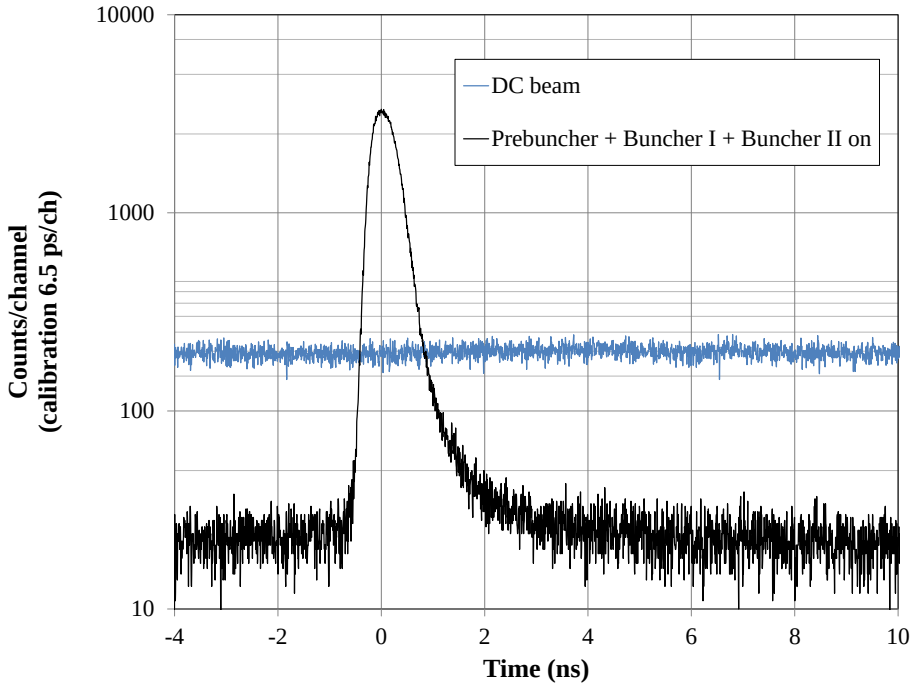

Figure 4.15: Time spectra of all bunchers in operation: We achieve a pulse duration of $\Delta t_{\mathrm{P}} = 540$ ps FWHM and a peak to background ratio of $\Lambda_{\mathrm{PBR}} = 185{:}1$. We measured the spectra for 300s.

Finally, in Figure 4.15 we show the time spectrum of all bunchers together. We achieve a pulse duration of $\Delta t_{\mathrm{P}} = 540$ ps FWHM and a peak to background ration of $\Lambda_{\mathrm{PBR}} = 185{:}1$. Since the pulsing components add transverse momentum to the beam particles, we lose about 35 % intensity with respect to the continuous beam. Nevertheless, the whole bunching system works properly and stable.

The Chopper

To reduce the positron background, the SPM interface is equipped with a chopper unit. The principle is explained in Chapter 3.5.2. The beam passes two plates with a time dependent, transverse field, which deflects the beam. The plates are field-free for a short time, when the pulse passes through. Positrons, which appear earlier or later, are deflected and annihilate on an aperture 400 mm downstream. Figure 4.16 shows a technical drawing of the unit, which includes the chopper and second sine wave buncher.

Figure 4.17 shows the chopper spectrum compared to the DC spectrum. The chopper deflects 79 % of the continuous beam and opens a time window of 2.9 ns FWHM, for

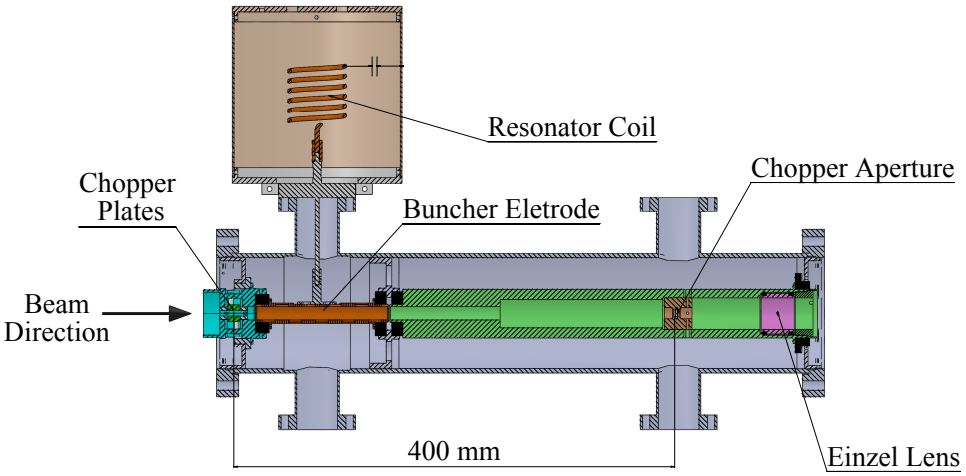

Figure 4.16: The chopper and the second sine wave buncher: The pulsed beam passes the chopper plates, where a time-dependent, electric field deflects background positrons. The undeflected part passes the tungsten aperture in a distance of 400 mm. The second sine wave buncher is identical to the first buncher.

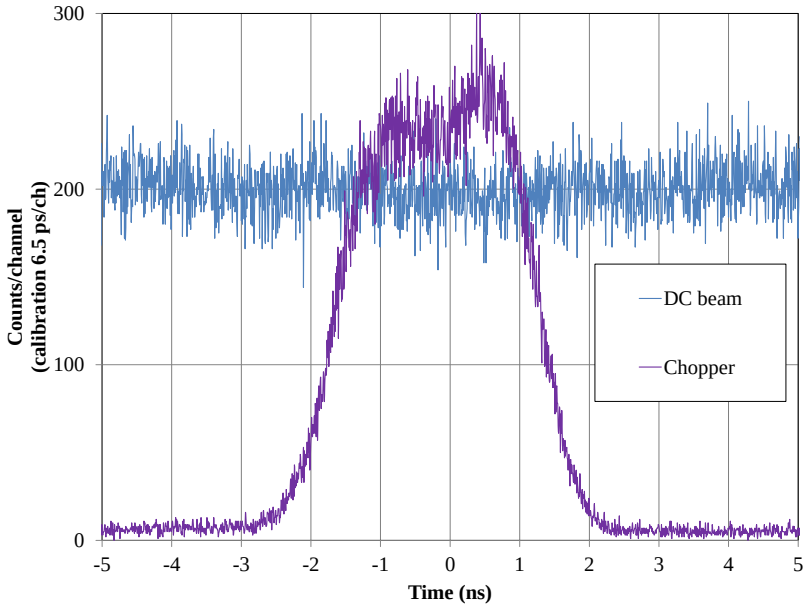

Figure 4.17: The chopper of the SPM interface supresses 79 % of the DC beam and creates a time window of 2.9 ns FWHM, where positrons can pass the chopper aperture. The RF electric field leads also to a modulation of the longitudinal beam velocity, according to Chapter 3.6.2. Therefore, the peak of the chopper spectrum exceeds the DC level, although both spectra have been measured for the same time.

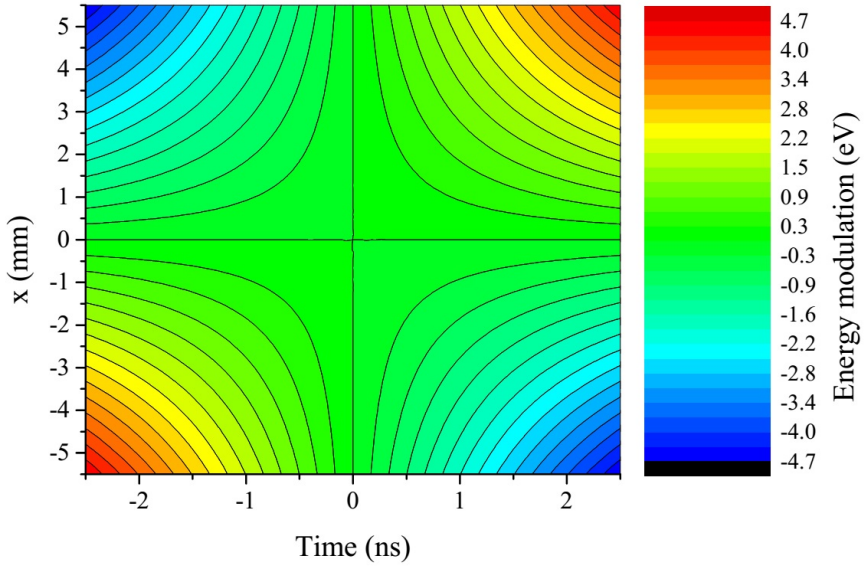

Figure 4.18: Energy modulation of the chopper: The chopper modulates the positron velocity in longitudinal direction, depending on the particle's position and passing time. The graph is calculated with Equation 3.105 and the values: $\widehat{U} = 6$ V, $t_{\mathrm{tr}} = 1.9$ ns, $t_{\mathrm{g}} = 5.0$ ns

the undeflected positrons to pass the aperture. Since both spectra have been measured for the same duration, the peak of the chopper spectrum should be on the DC level, however, it is more than 25 % higher. According to Chapter 3.6.2 we can explain this effect by a modulation of the longitudinal beam velocity and, thus, the weak additional bunching behavior caused by the transverse chopper field. Figure 4.18 shows the energy modulation of the velocity in longitudinal direction for positrons passing the chopper plates.

Since the chopper deflects a major part of the DC beam, not all positrons will pass the aperture. We can calculate the position $x_{\mathrm{ap}}(t)$ of the beam on the aperture:

$$x_{\mathrm{ap}}(t) = -\frac{\widehat{U}\, F(t)\, e}{2\, D\, E} \cdot l_{\mathrm{ch}} \left(\frac{1}{2} \cdot l_{\mathrm{ch}} + l_{\mathrm{ap}} \right) \tag{4.3}$$

Here, D is the distance between the chopper plates, l_{ch} their length and l_{ap} the distance between plates and aperture. If we insert the values $D = 11$ mm, $E = 200$ eV, $l_{\mathrm{ch}} = 16$ mm and $l_{\mathrm{ap}} = 400$ mm, we find that all positrons, appearing 1.7 ns before or after the reference positron, annihilate on the aperture. With this information, we calculate the arrival time on the annihilation target for the remaining particles. The result is shown in Figure 4.19.

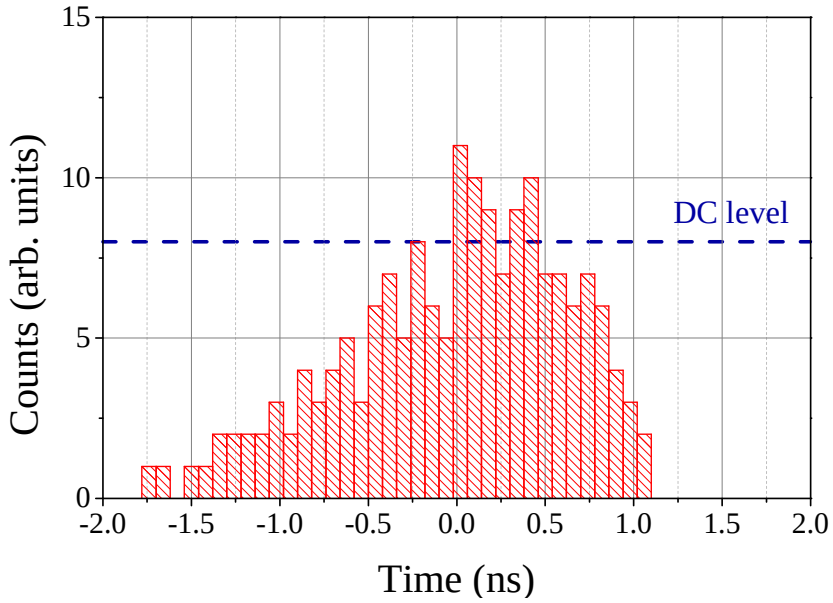

Figure 4.19: Calculated arrival times for positrons at the annihilation target: Since the chopper modulates E and, therefore, the velocity in longitudinal direction, the spectrum shows a bunching behavior.

Since the chopper modulates E, the calculated spectrum shows no evenly distributed events. We observe similar results for the measured spectrum. Therefore, the theoretical calculations match the measurement results. Although the chopper influences the longitudinal particle velocity, it disturbs neither the time structure, nor the quality of the beam.

By setting all pulsing components of the SPM interface in operation, we obtain the time spectrum, shown in Fiure 4.20. The final pulse duration is $\Delta t_{\mathrm{P}} = 362$ ps FWHM at a peak to background ratio of $\Lambda_{\mathrm{PBR}} = 993{:}1$. We present an overview of the influences on the time structure, caused by the different pulsing components, in Table 4.2. If we compare the final pulsed beam with the DC beam, we notice a loss of almost half of the positrons. This is due to transverse momentum, which all pulsing components add on the beam, leading to more annihilation at constrictions along the beam path. We are not able to compensate these effects sufficiently by adjusting the electrostatic and magnetic transport fields. However, the results are adequate to run the positron elevator as desired. Furthermore, we can already use this beam to perform PALS, which we show in the following sections.

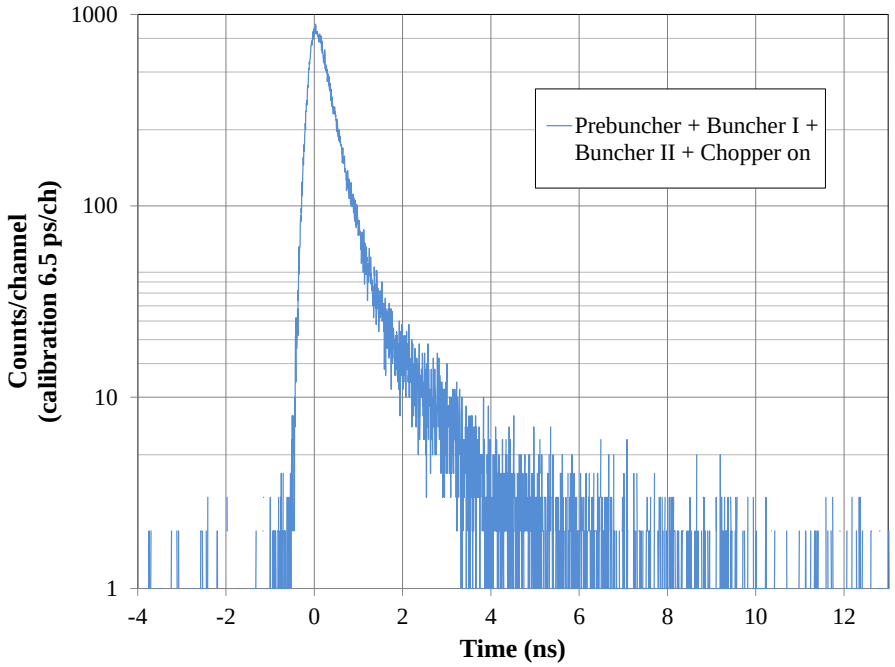

Figure 4.20: Time spectrum with all pulsing components in operation: We achieve a pulse duration of $\Delta t_{\mathrm{P}} = 362$ ps FWHM and a peak to background ratio of $\Lambda_{\mathrm{PBR}} = 993{:}1$. The spectrum was measured for 100 s and includes 110,000 counts.

4.3.2 The SPM Interface Remoderator

Figure 4.21 depicts a technical drawing of the SPM interface remoderator unit. The electrostatically transported beam is focused by a magnetic lens on a tungsten single crystal (W100). The lens consists of two current carrying coils, integrated in a μ-metal housing, which concentrates the magnetic field with a pole shoe in a small region. We bias the tungsten crystal on a potential of -4.8 kV, so that the implantation energy is 4.8 keV. Since we operate the remoderator in reflection geometry, the previous electrostatic lens system is biased on a more negative potential of $\approx$ -5 keV. In this way, it is possible to extract the re-moderated beam with the same lens system. A tungsten-copper jacket around the remoderator crystal shields the annihilation radiation of unmoderated positrons. Two slits in this structure allow to monitor the re-moderation process. In addition, we can heat and anneal the crystal by electric current.

We determine the re-moderation efficiency ε by measuring the annihilation radiation for different electric remoderator potentials. In normal operation, the crystal potential is repulsive and re-moderated positrons can leave the surface. If it is attractive, the particles are captured and annihilate, unless they are not directly reflected. According to Equa-

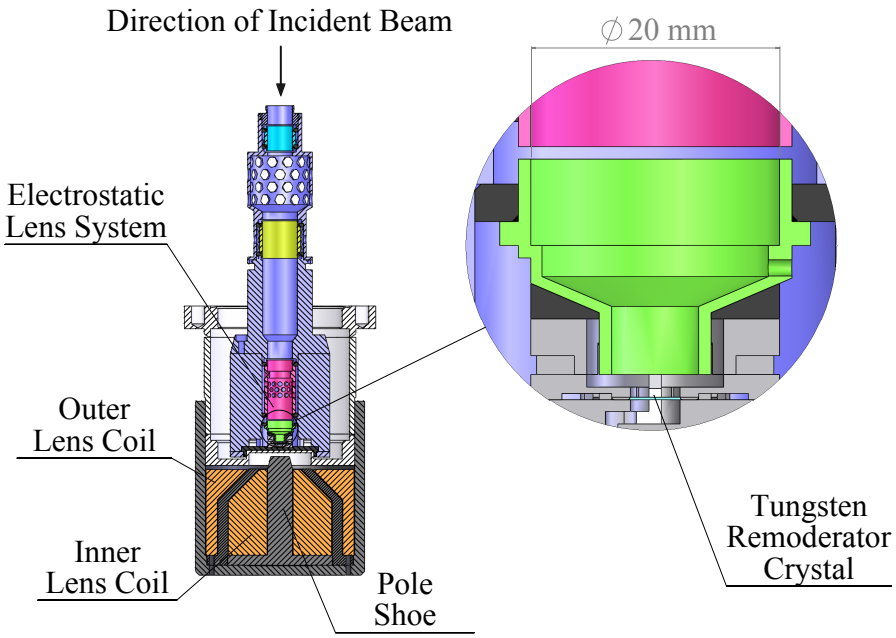

Figure 4.21: The SPM interface re-moderation unit: A magnetic singe-pole lens focuses the beam on tungsten single crystal (W100) that is biased on a potential of ≈ -4.8 kV. Re-moderated positrons are extracted by the same electrostatic lens system, which is on a more negative potential than the crystal.

Pulsing components	Δt_{T} (ps)	Δt_{P} (ps)	Λ_{PBR}	e^+-loss (%)
None	∞	∞	1:1	0
Prebuncher	3900	3893	5:1	8
Prebuncher + Buncher I	826	793	155:1	18
Prebuncher + Buncher I + Buncher II	586	539	185:1	35
Prebuncher + Buncher I + Buncher II + Chopper	429	362	993:1	47

Table 4.2: Influences on the time structure, caused by the pulsing components: We determine the total time resolution Δt_{T} for each case by a Gaussian fit of the corresponding spectrum. The pulse duration Δt_{P} is calculated with Equation 4.1 and a detector resolution of $\Delta t_{\mathrm{D}=}$ 230 ps FWHM. Δt_{T} and Δt_{P} are FWHM values.

tion 4.2, we can determine the number of positrons annihilating inside the remoderator crystal. For an attractive crystal potential, the detector count rate C_{att} is proportional to the difference of incident and reflected positrons, if the annihilation radiation of the deflected part is not measured by the detector:

$$C_{\mathrm{att}} = A(I_{\mathrm{i}} - I_{\mathrm{ref}}) \tag{4.4}$$

It is not possible to measure the number of reflected positrons I_{ref} directely, however, we can estimate it. H. H. Seeliger discusses different backscattering processes for positrons in [95]. Also, P. G. Coleman et al. measured the backscattering of 7 keV positrons as a function of the atomic number Z of the target material [96]. From these results, we can estimate a fraction of backscattered positrons f, for an implantation energy of 5 keV and $Z = 74$ for tungsten, as $f \lesssim 30$ %. We can rearrange Equation 4.4 and obtain:

$$C_{\mathrm{att}} = A(1 - f)I_{\mathrm{i}} \tag{4.5}$$

Using the same detector and the same geometry for a repulsive electric potential, we can express C_{rep} as:

$$C_{\mathrm{rep}} = C_{\mathrm{att}} - C_{\mathrm{rem}} = C_{\mathrm{att}} - AI_{\mathrm{rem}} \tag{4.6}$$

If we define the re-moderation efficiency ε as the fraction of re-moderated positrons compared to the number of incident positrons, we can write:

$$\varepsilon = \frac{I_{\mathrm{rem}}}{I_{\mathrm{i}}} = (1-f)\frac{C_{\mathrm{att}} - C_{\mathrm{rep}}}{C_{\mathrm{att}}} \tag{4.7}$$

Since f depends on different aspects, like material characteristics, implantation energy or geometric properties, ε always represents the whole re-moderation system and not only the re-moderator material. For Equation 4.7 we can also calculate the precision of the result, using Gaussian propagation of uncertainty:

$$\Delta\varepsilon = \sqrt{\left(\frac{C_{\mathrm{att}} - C_{\mathrm{rep}}}{C_{\mathrm{att}}}\Delta f\right)^2 + \left((1-f)\frac{C_{\mathrm{rep}}}{C_{\mathrm{att}}^2}\Delta C_{\mathrm{att}}\right)^2 + \left(-\frac{1-f}{C_{\mathrm{att}}}\Delta C_{\mathrm{rep}}\right)^2} \tag{4.8}$$

For the SPM interface remoderator we measured $C_{\mathrm{rep}} = 9190$ cps and $C_{\mathrm{att}} = 13750$ cps. Assuming a fraction of 30 % backscattered positrons, a standard deviation of $\Delta f = 0.05$ and $\Delta C = \sqrt{C}$ from Poisson statistics for the count rates C, we obtain for the remoderator efficiency

$$\varepsilon = (23.2 \pm 1.8)\ \% \ .$$

4.4 SPM Control and Optimization Software

The operation of the SPM at the FRM II differs entirely from the laboratory. NEPOMUC provides positrons for up to five experiments, however, they can not be operated simultaneously. Thus, the SPM beam time will also be restricted and in the beginning of every measurement cycle, we will have to calibrate the whole system again. In the context of this work, it was necessary to guide the beam through the SPM interface for several times. To achieve that, we have to adjust 68 static electric and magnetic fields properly. In addition, these setting parameters are intercorrelated, so that we have to consider the whole parameter space, in order to lose as low positrons as possible. Doing this manually takes at least several days and wastes much rare beam time.

To overcome this problem, we programmed a computer-assisted routine based on the *Nelder-Mead Method* or, also called, *Downhill Simplex Algorithm*. It optimizes each parameter p_i, of a selection, with the goal to reach a maximum number of annihilating positrons at a certain target. Therefore, the program uses the detector count rate N as a reference value, which is an unknown function of the parameter space $P_i(p_0, p_1, p_2, ..., p_k)$. To optimize k parameters, the program measures $k+1$ values for $N(P_i)$. This parameter space is necessary to specify a k-simplex, a k-dimensional polytope with $k+1$ vertices. Subsequently, the program repeats a number of steps, which we present in Table 4.3.

Step	Description
1	For a number of k parameters define $k+1$ start conditions (points $P_i \in \mathbb{R}^k$). Obtain for each point the detector count rate $N(P_i)$.
2	Order all values $N(P_i)$, beginning with the highest ($N(P_1)$), ending with the smallest ($N(P_{k+1})$).
3	Calculate the centroid P_c of all points, except the worst point P_{k+1}: $P_\mathrm{c} = \sum_{i=1}^{k} N(P_i)P_i / \sum_{i=1}^{k} N(P_i)$.
4	Reflect the worst point P_{k+1} on P_c: $P_\mathrm{r} = P_\mathrm{c} + \alpha(P_\mathrm{c} - P_{k+1})$ with $\alpha > 0$.
5	If P_r is better than P_1, calculate the expanded point $P_\mathrm{e} = P_\mathrm{c} + \beta(P_\mathrm{r} - P_\mathrm{c})$ with $\beta > 0$. If P_e is better than P_r replace P_{k+1} with P_e and go to step 2. Otherwise, replace P_{k+1} with P_r and go to step 2.
6	If P_r is better than the second worst point P_k, replace P_{k+1} with P_r and go to step 2. If P_r is not better than P_k, continue with step 7.
7	The reflected point P_r is not better than the second worst P_k! Compute the contracted point $P_\mathrm{con} = P_\mathrm{c} + \gamma(P_{k+1} - P_\mathrm{c})$ with $0 < \gamma \leq 0.5$.
8	If P_con is better than P_{k+1}, replace P_{k+1} with P_con and go to step 2. If the contracted point is not better than the worst point, go to step 9.
9	Move all points, except the best point P_1, in the direction to P_1: $P_i = P_1 + \delta(P_i - P_1)$ with $0 < \delta < 1$.
10	Go to step 2.

Table 4.3: The *Downhill Simplex Algorithm* of the SPM interface software: The program uses 10 steps, to optimize a number of k parameters.

The algorithm coefficients α, β, γ and δ can be changed manually before the program starts. Typical values for the optimization of the SPM interface are:

$$\alpha = 1.0 \text{ (reflection)}$$
$$\beta = 2.0 \text{ (expansion)}$$
$$\gamma = 0.5 \text{ (contraction)}$$
$$\delta = 0.5 \text{ (shrink)}$$

Table 4.3 shows that, in general, the *Downhill Simplex Algorithm* is an endless routine. In practice, we have to define a stop criterion. Since the detector count rate N is an unknown function of the parameter space, it is not practical to use an upper limit for N, where the program should stop. A more favorable criterion is the deviation of all $N(P_i)$. The algorithm starts with an arbitrary large simplex volume, however, step 7 - 9 lead to a decrease of it. This means that the distance of the points from each other decreases. Therefore, the values of $N(P_i)$ equalize and the standard deviation shrinks. Our software uses this fact to stop the algorithm. We can set the lower limit for the standard deviation in the beginning manually.

Figure 4.22 shows a test for the optimization of two values. Here, the algorithm optimizes the parameters with the goal to find the maximum of a two-dimensional Gaussian function. The algorithm reaches 99.7 percent of the maximum possible value for N within 18 iterations. In reality, the function for N is more complicated and it is often necessary to adjust more than two parameters. However, the picture shows that the algorithm works. Nevertheless, the program does not work completely independent of a human user. Especially the start values have to be chosen carefully to reach the desired result. If we set the start points too close to a local maximum, the simplex algorithm might have problems to find the global maximum. The same happens, if the start parameters have been chosen too far from the maximum, since $N(P_i)$ is for most parameter values zero.

With this program it has been possible to reduce the adjustment time by a factor of about 50. In the beginning, we have needed up to one week to transport the beam through the SPM interface with a sufficiently high count rate at the end. The software controlled optimization minimized this time to several hours.

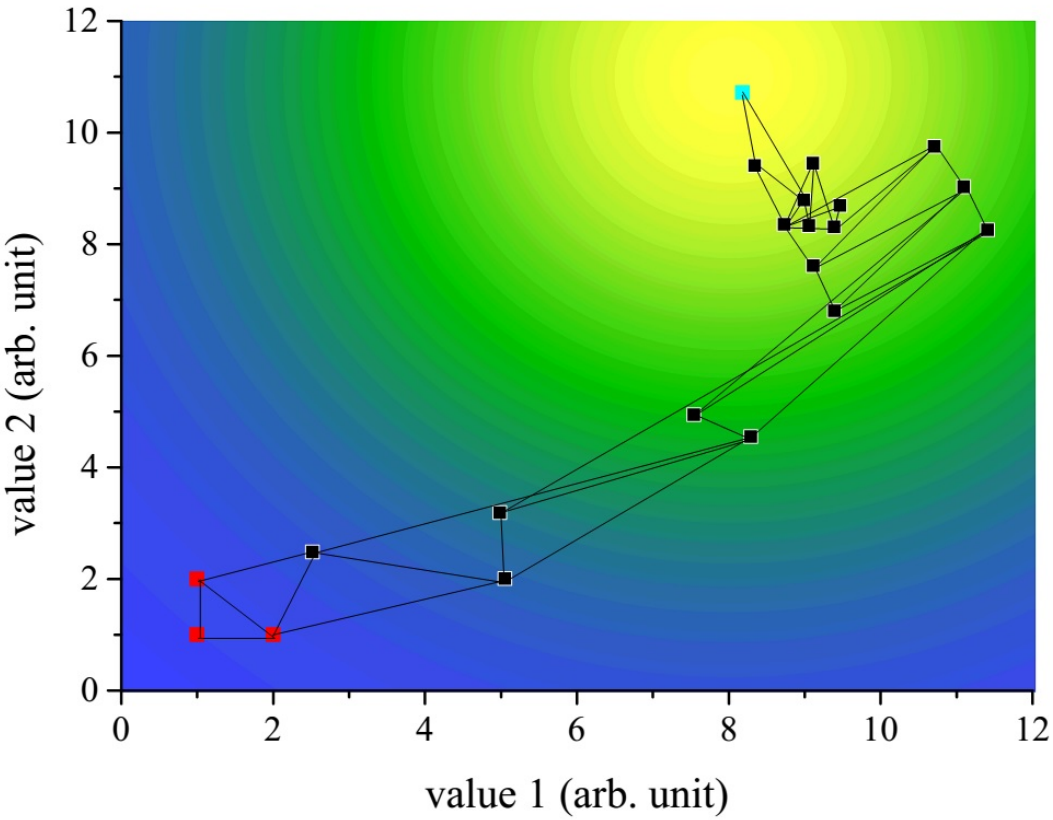

Figure 4.22: Optimization of 2 parameters by the SPM interface software: To test the algorithm, we use a two-dimensional Gaussian function. The program starts with three points (red) and reaches 99.7 percent of the maximum value within 18 iterations.

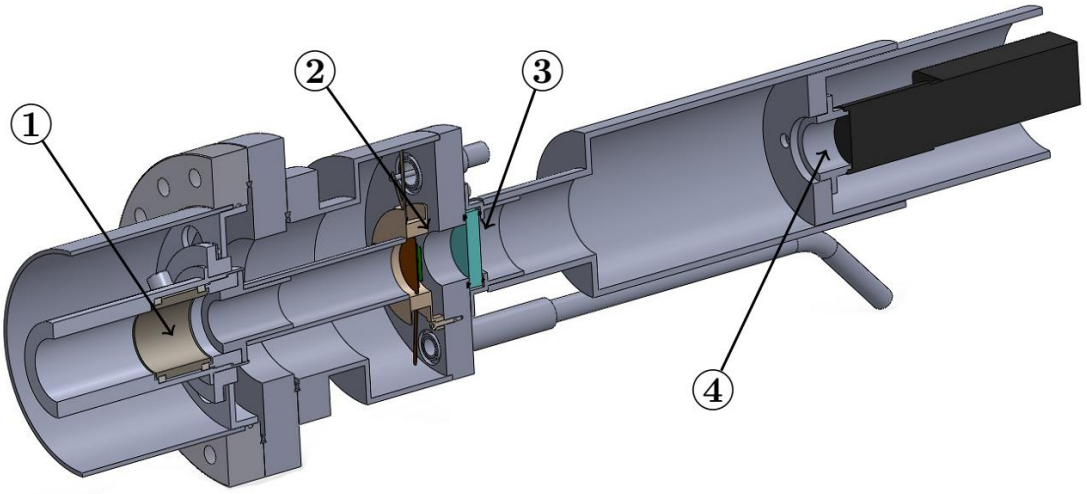

Figure 4.23: Technical drawing of the MCP detector system, mounted after the second bunching unit of the SPM interface: We focus the beam via an Einzel lens ① on the MCP surface ②. The phosphorescing layer on the backside is observed with a CCD camera ④ through a window ③ [97, 98].

4.5 Components for Beam Characterization at the SPM Interface

The key component connecting SPM and interface is the positron elevator, which increases the potential energy of the brightness enhanced, re-moderated and pulsed beam. To run the SPM properly, we must ensure that the elevator does not destroy the high beam quality. Therefore, we characterize the beam in before entering the elevator and after leaving. The results for the non-elevated beam are shown in this section. A rapid way to analyze the beam is the application of an MCP (Micro Channel Plate) detector. Figure 4.23 shows the device that has been we mounted at the end of the second bunching unit. It was constructed by T. Gigl as part of his diploma thesis [97]. With the Einzel lens at the end of the buncher drift tube, it is possible to focus the beam on the MCP surface. The arising image is shown in Figure 4.24.

In addition, we need a more sophisticated beam diagnostic. Therefore, J. Mitteneder constructed and built a special sample chamber as part of his master's thesis [98]. The thesis was supervised in the context of this work. It includes a complete description of the sample chamber, numerical simulations and measurement results. We present the most important results in the following sections. Some of the results have been already published in [99].

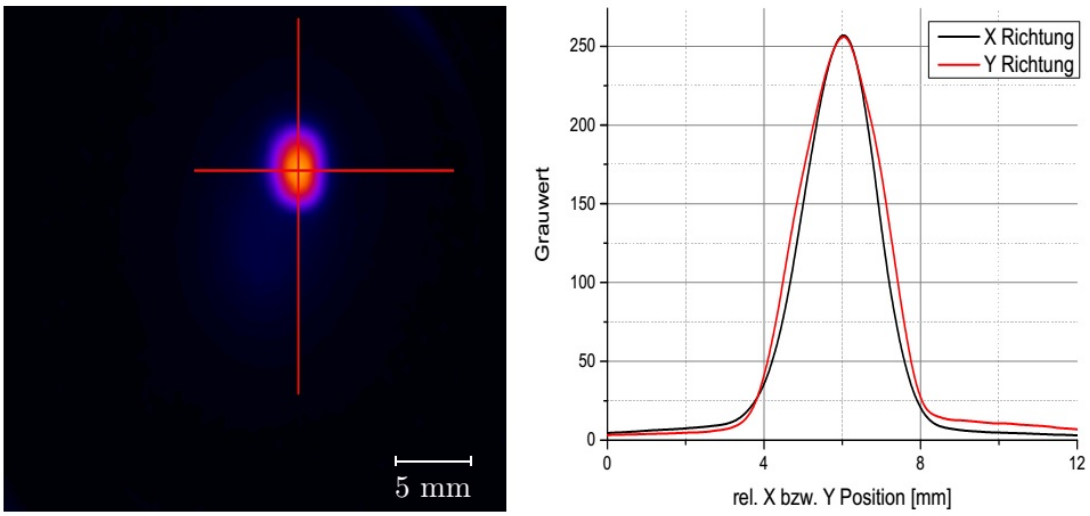

Figure 4.24: Spot of the focused beam at the end of the SPM interface, obtained with the MCP detector system (left) and graph of the beam profile in x and y direction (right): The beam spot is elliptically distorted. Its size is 2.15 mm FWHM in x, and 2.41 mm FWHM in y direction. The image is taken from [98].

4.5.1 Sample Chamber for Beam Diagnostics

We show a technical drawing of the specially constructed sample chamber for beam diagnostics in Figure 4.25. It is mounted directly after the second bunching unit, at the position, which is foreseen for the elevator. The pulsed beam passes an inner potential tube, where it is accelerated to its final implantation energy of about 2 keV. We deflect the beam in x and y direction by a set of coil pairs. This way, it is possible to scan the beam over a sample. We use the magnetic lens of the SPM remoderator to focus the beam. Therefore, we characterize the lens properties and the characteristics of the beam simultaneously. Furthermore, we are able to predict a future beam spot size on the last remoderator and, therefore, we can estimate the spatial resolution of the SPM at NEPOMUC.

We measure the annihilation radiation with the BaF_2 scintillator detector, which is placed behind a tungsten shield to avoid the detection of backscattered positrons. The setup allows first spatially resolved PALS at the FRM II. In order to save rare beam time, we programmed a special software, which controls the scanning coils, the magnetic lens and the measurement electronics. This way, we obtain two-dimensional PALS maps automatically. We present these results in the following section.

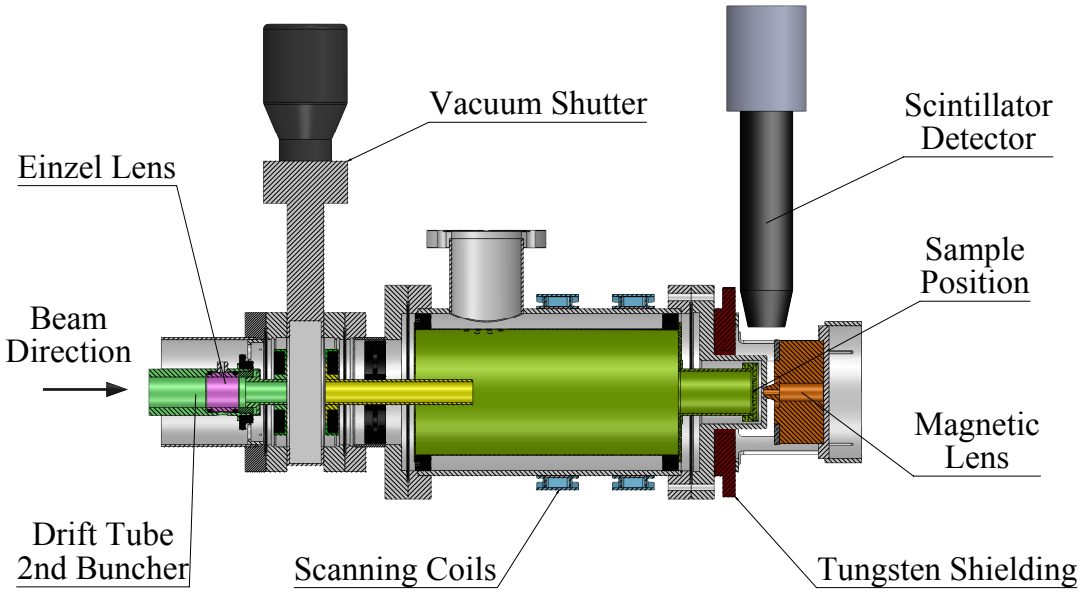

Figure 4.25: Technical drawing of the sample chamber for beam diagnostics: It is mounted after the second sine wave buncher of the SPM interface. The pulsed beam enters the device from the left, passes the vacuum shutter and is accelerated to its final implantation energy. We can deflect the beam by a set of scanning coils. A magnetic lens focuses the beam on the sample surface. A tungsten ring shields the detector from annihilation radiation of backscattered positrons.

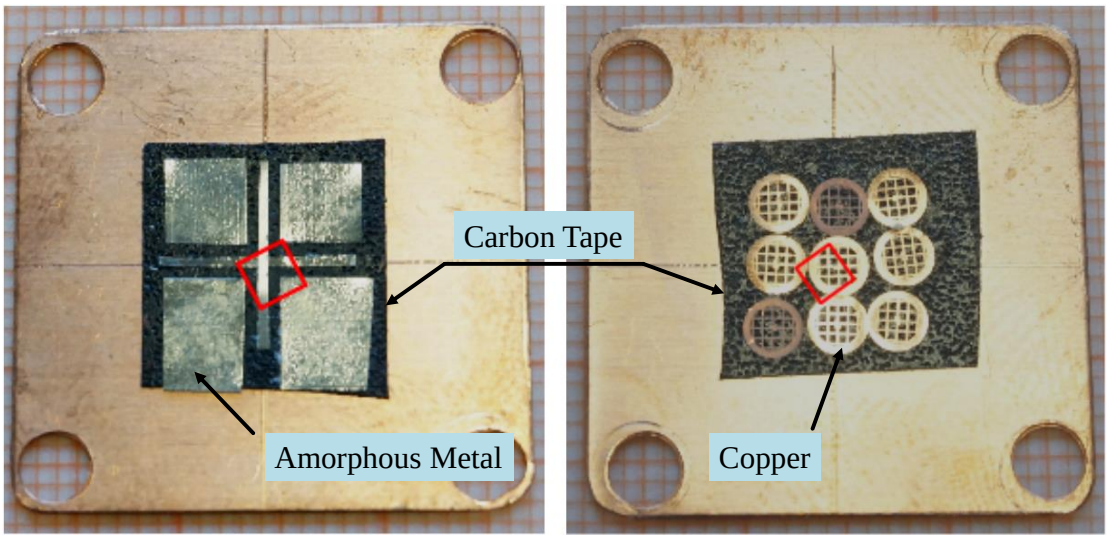

Figure 4.26: Samples for the beam characterization: Stripes of amorphous metal on carbon tape (left) and copper grids on carbon tape (right). The tagged rectangles (red) mark the scanned areas.

4.5.2 Spatially Resolved PALS Measurements at the SPM Interface

We use the sample chamber that is shown in Figure 4.25, to perform spatially resolved PALS. The goal is to scan the beam over an inhomogeneous sample and obtain a two-dimensional positron lifetime map. In combination with the sample geometry, we are able to determine beam parameters like the beam spot size and the spread of the positron beam. For that, we have prepared two different samples, which consist of two materials each, with explicitly different positron lifetimes. Figure 4.26 shows an image of both sample. The first sample consists of amorphous metal stripes on a conductive carbon tape, while the second sample is a composition of small copper grids on the same tape. The average positron lifetime in copper and amorphous metal at the implantation energy 1.5 keV is dominated by surface lifetimes close to 400 ps. The average positron lifetime for the carbon tape is $\approx$ 1.2 ns, due to a long lifetime component of 3.0 ns from pick-off annihilation of positronium in polymer voids [100]. Figure 4.27 shows positron lifetime spectra for carbon tape and amorphous metal, measured for 50 min including more than 5 million counts, each. As we can infer from Figure 4.28, an acquisition time of 8 s, corresponding to $\approx$ 13000 counts is sufficient to differentiate between both materials.

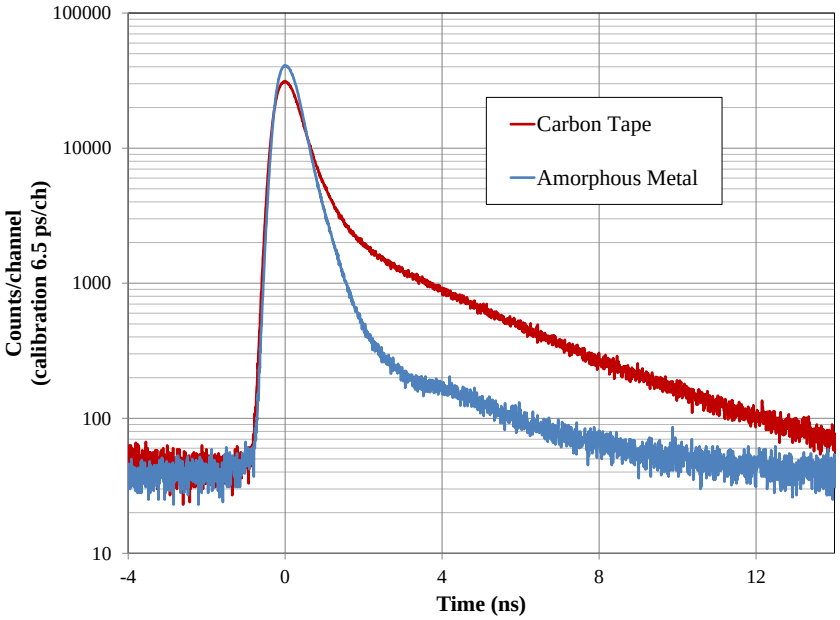

Figure 4.27: Positron lifetime spectra of carbon tape (red) and amorphous metal (blue): The spectra have been measured at two different points on the sample for 3,000 s and include ≈ 5 million counts, each.

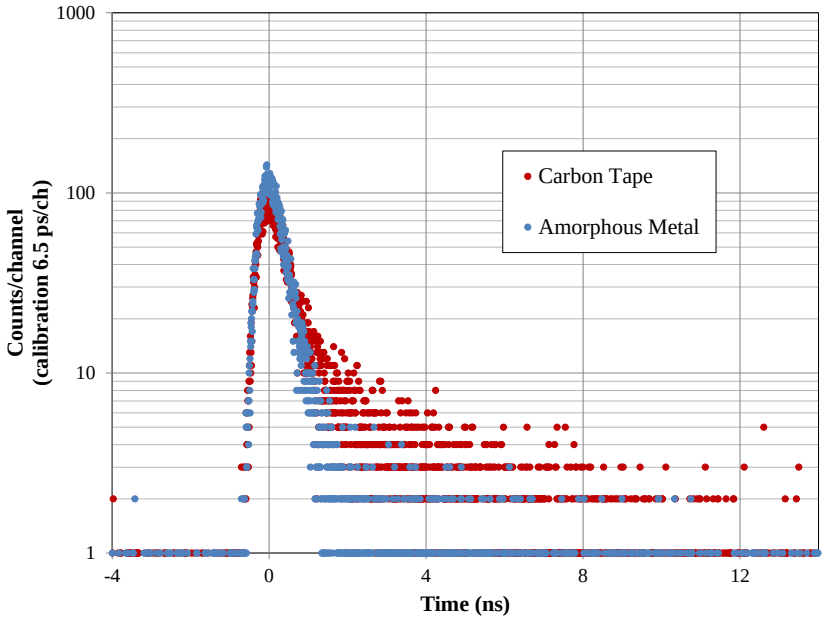

Figure 4.28: Spectra of carbon tape (red) and amorphous metal (blue) after a measurement time of 8 s: It is possible to differentiate the two materials because of their very different mean positron lifetimes. Each spectrum includes 13,000 counts.

To obtain a two-dimensional map, the pulsed beam is scanned over the sample and a positron lifetime spectrum is measured at each point. We generate an image by computing the first moment $T_{1\mathrm{st}}$ of the spectra:

$$T_{1\mathrm{st}} = \frac{\sum_{i=0}^{\infty}(t_i \cdot y_i)}{\sum_{i=0}^{\infty} y_i} \tag{4.9}$$

Here, t_i is the channel number and y_i the counts in this channel. For a pure, exponentially decaying spectra, $T_{1\mathrm{st}}$ represents the average positron lifetime τ_{av}.

Figure 4.29 shows the average lifetime map of the amorphous metal on carbon tape. A scanned area of 3 mm^2, including 441 single positron lifetime spectra, is shown. The step size between the measurement points is 83 µm and each pixel was measured for 8 s. We use this sample to determine the beam spot size, by scanning the beam over the edge of a metal stripe. This line scan is tagged with a white line in the picture. We observe a diameter of $d_{\mathrm{FWHM}} = (180 \pm 10)$ µm for an implantation energy of 1.5 keV [98].

The average positron lifetime map of the copper grid on carbon tape is shown in Figure 4.30. It includes 2544 single spectra and depicts a scanned area of 2.7 mm^2. The step size between the measurement points is 30 µm. The rectangular wholes of the copper grid are 425 $\times$ 425 µm^2 in size. Since they are bigger than the beam diameter, it is possible to obtain the average lifetime of the carbon tape between the copper bars. However, we cannot completely resolve the average copper lifetime on the 83 µm wide bars, as the line scan shows.

4.5.3 4D AMOC Measurements at the SPM Interface

Although we have built the sample chamber in order to investigate the beam characteristics of the SPM interface, we take the opportunity and use the device to perform additional measurements. The *Institut für angewandte Physik und Messtechnik LRT2* of the Universität der Bundeswehr München develop two new detectors, which enable measuring the full electron momentum and the positron lifetime at the same time, using both detector in combination. Additionally, the beam quality and its stability qualify the SPM to perform this first four-dimensional age momentum correlation (4D AMOC)

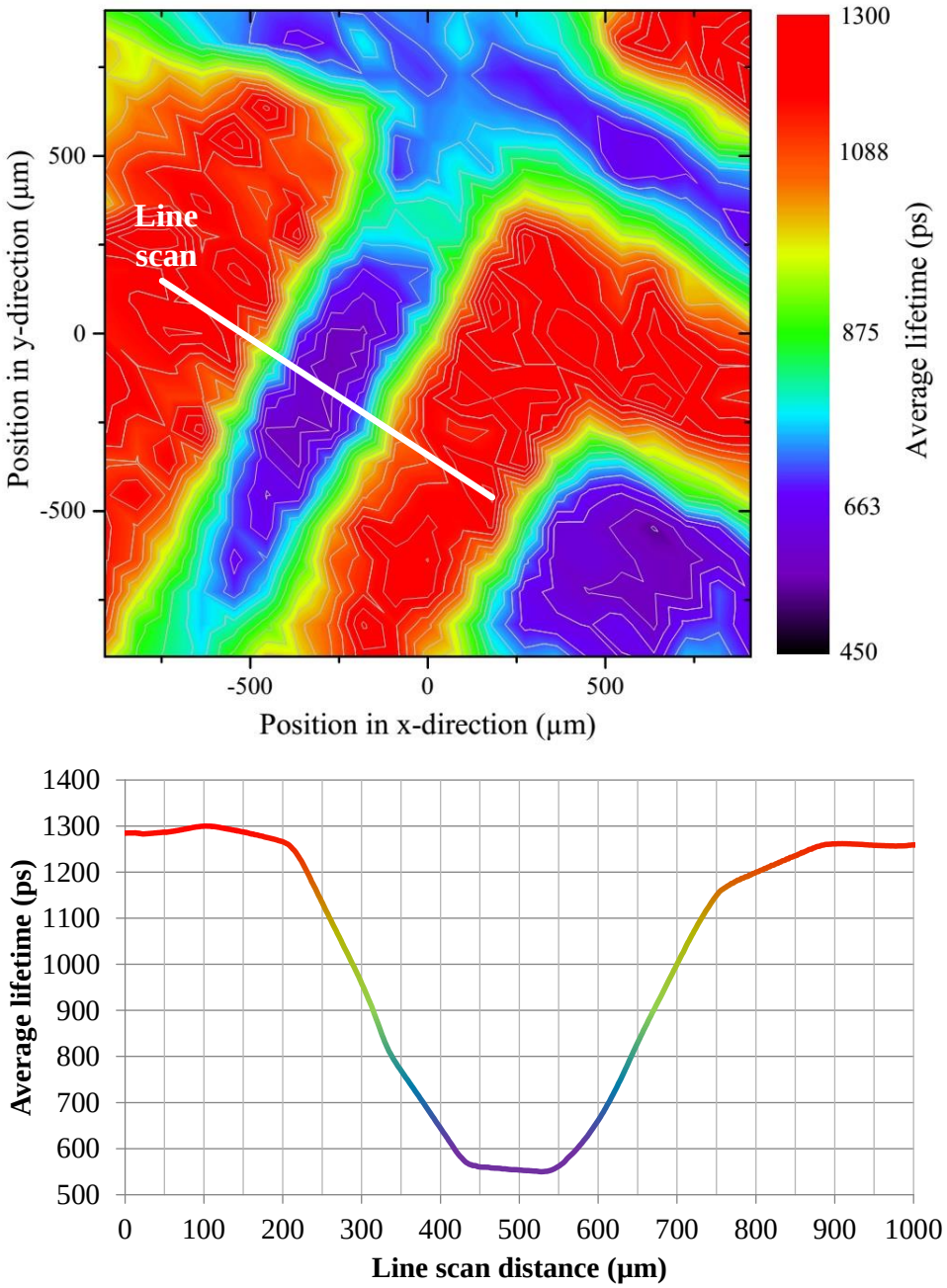

Figure 4.29: Average positron lifetime map of the first sample: The average lifetime of carbon tape (red) is higher than the lifetime of amorphous metal (violet). The picture includes 441 positron lifetime spectra with a measurement time of 8 s, each. The whole map has been measured within 70 min at an implantation energy of 1.5 keV. From the line scan we can determine the mean beam diameter as $d_{\mathrm{FWHM}} = (180 \pm 10)$ µm.

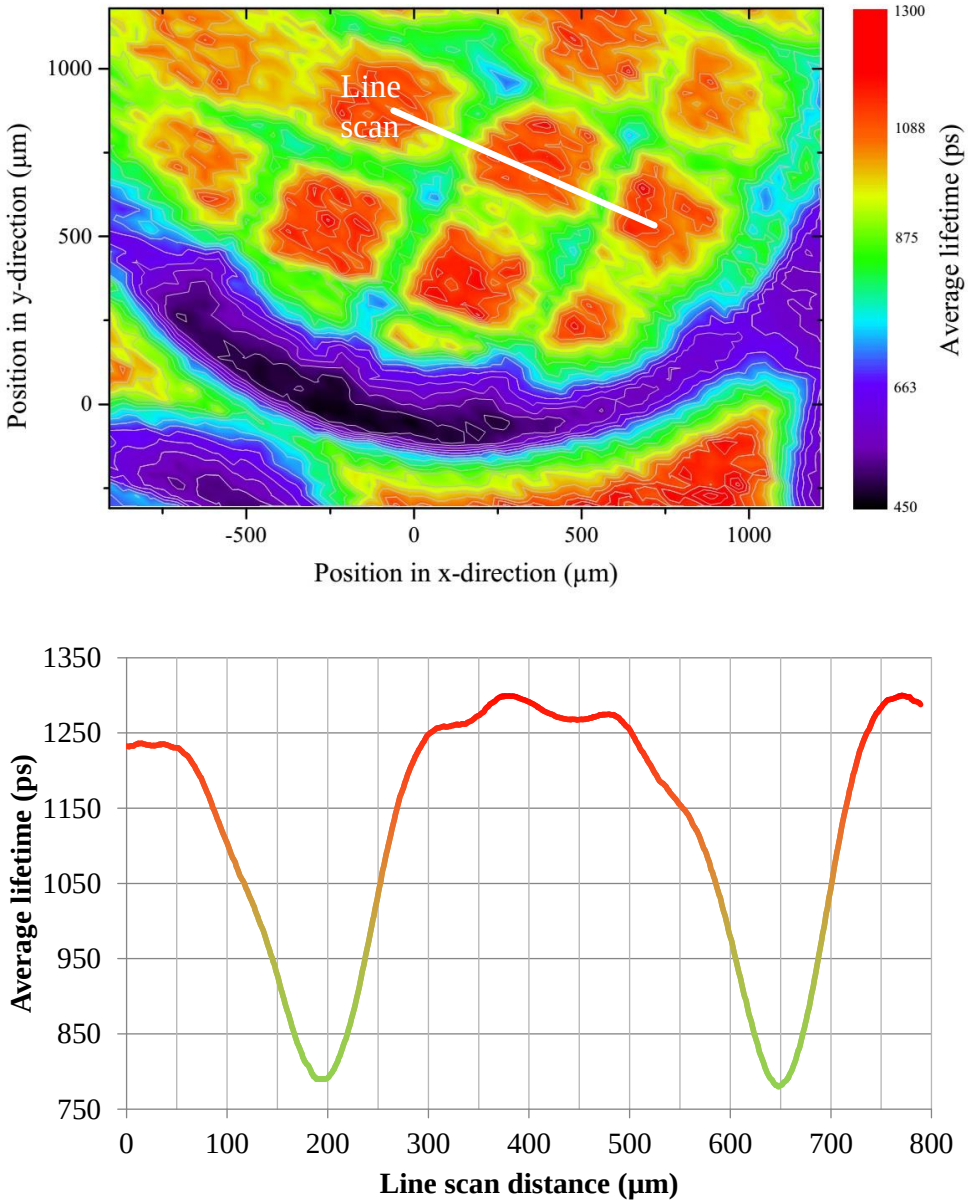

Figure 4.30: Average positron lifetime map of the second sample: The average lifetime of carbon tape (red) is higher than the copper lifetime (violet). The picture includes 2544 positron lifetime spectra with a measurement time of 8 s, each. The whole map has been measured within 8 hours at an implantation energy of 1.5 keV. The line scan shows that the 83 µm wide grid bars are too small to resolve the mean copper lifetime on them, using a beam of 180 µm in size.

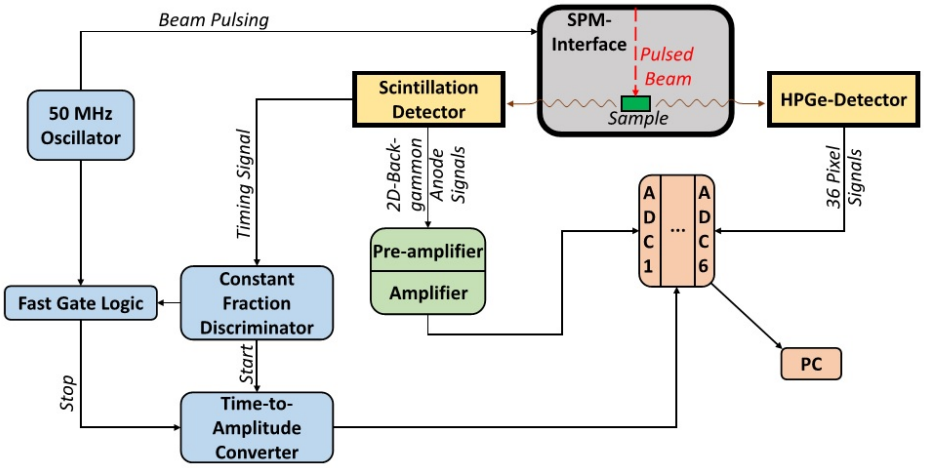

Figure 4.31: 4D AMOC measurement setup: The pulsed and focused beam hits the sample. The annihilation radiation is detected by the two pixelated detectors in an 180° arrangement. The picture is taken from [101].

spectroscopy. For that reason, we replaced the BaF_2 scintillator detector with the new detectors. Figure 4.31 shows an overview sketch of the measurement system.

Both detectors are pixelated to investigate the angular deviation of two related annihilation γs and, therefore, the transverse electron momentum. One of them is a high purity germanium detector, which is used to obtain the longitudinal momentum by measuring the Doppler broadening of the 511 keV peak. The position sensitivity is realized by a segmentation of the germanium crystal. With this detector we achieved a position resolution of 1.6 mm and an energy resolution of 1.33 keV (at 622 keV ^{113}Cs)) in previous measurements [102, 103].

The positron lifetime is measured with a fast timing detector. It consists of a $CeBr_3$ scintillator crystal that is coupled to a microchannel plate image intensifier (MCPII), which is mounted on a resistive anode. This detector obtains the position from a two-dimensional backgammon anode, which is coupled from the outside. The time resolution of about 320 ps FWHM is limited by the pixel cross section. U. Ackermann presents a detailed description of the detector in [104].

Both detectors are arranged at an angle of 180°. A shield of tungsten and lead avoids the detection of backscattered positrons. In order to achieve similar angular resolutions with both detectors, we placed the scintillator detector at a distance of 21 cm from the sample and the germanium detector 15.5 cm from the sample. The data acquisition bases on a VME (Versa Module Eurocard) system, which has been already used for former measurements. B. Löwe explains the system in detail in [102].

Gold foil	τ_1 (ps)	I_1 (%)	τ_2 (ps)	I_2 (%)	τ_3 (ps)	I_3 (%)		
PLEPS	175	22.4	347	77.3	2454	0.3		
SPM interface	175	22.1	347	76.1	2550	1.8		
Carbon tape	τ_1 (ps)	I_1 (%)	τ_2 (ps)	I_2 (%)	τ_3 (ps)	I_3 (%)	τ_4 (ps)	I_4 (%)
PLEPS	162	13.9	380	52.2	1029	5.9	3013	28.0
SPM interface	162	13.7	380	51.5	1029	7.8	2650	27.0

Table 4.4: Positron lifetime components and intensities of the measured samples, obtained with PLEPS and the SPM interface. The table is taken from [101].

With this system, we investigate two samples. The first sample is a 10 µm thick gold foil of 99.999 % purity, the second one is a double-sided adhesive carbon tape. We use the same tape as for the samples, described in Section 4.5.2. In previous measurements, we have investigated the positron lifetime of both samples with PLEPS. Table 4.4 shows these results, compared to our measurements. The conformity of both systems shows that the current state of the SPM interface is adequate to perform PALS.

Figure 4.32 shows 4D AMOC spectra for both samples. We obtain all results with a positron implantation energy of 2 keV. For this measurement geometry and a computer optimized beam, we achieve a count rate of 0.3 Hz, with both detectors in coincidence. We present a detailed discussion of the first 4D AMOC measurements in [101]. In addition, U. Ackermann presents a further discussion of the measurement and the results in his PhD thesis [105].

The measurements of 4D AMOC spectra at the SPM interface demonstrate the feasibility of a pulsed microbeam. Although the low count rate leads to measurement times of more than 4 days, the results show the long-term stability and the beam quality of the system. Furthermore, we used the present status of the interface to perform unique measurements.

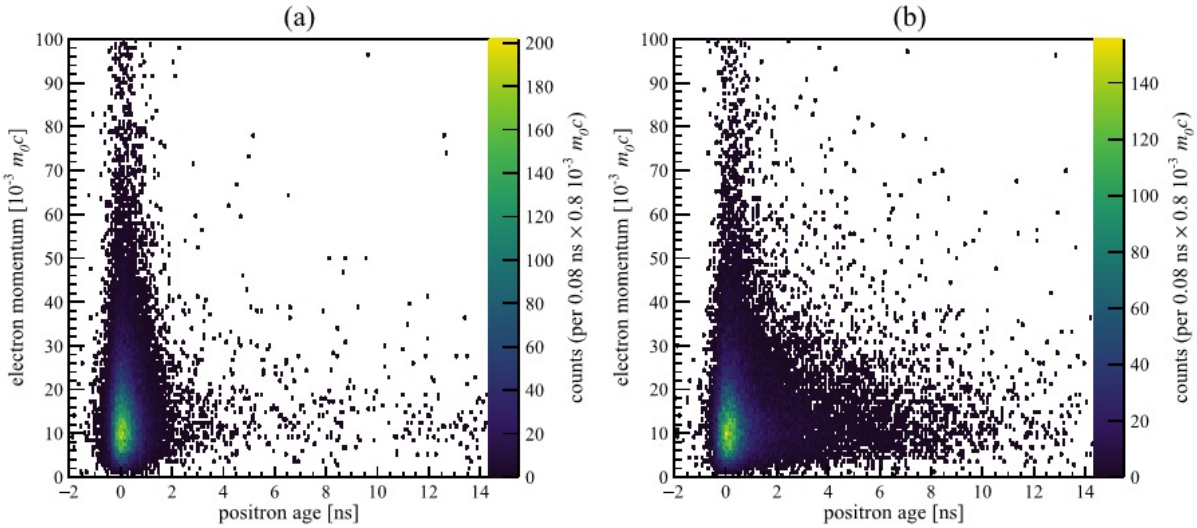

Figure 4.32: 4D AMOC spectra of the gold foil (a) and the carbon tape (b): The diagram show the absolute value of the three-dimensional electron momentum as a function of the positron age. Each spectrum includes $4 \cdot 10^4$ counts [101].

5 The Positron Elevator

We discussed in the previous chapters that we connect the SPM with NEPOMUC in order to increase the count rate and, therefore, reduce the measurement time considerably. The SPM interface adapts the NEPOMUC beam to the requirements of the microscope. The beam energy at the end of the interface is $E_{\mathrm{pot}} =$ -5 keV and $E_{\mathrm{kin}} = 600$ eV. However, the SPM requires a potential beam energy of $+5$ keV, to reach a desired implantation energy for the SPM remoderator, which is biased on ground potential. Accelerating the beam by more than 800 % of its original velocity within a limited distance of less than 30 cm is not possible without destroying the high beam quality. If we want to operate the well-balanced microscope without any reconstructions, we have to increase the potential beam energy by 10 keV. For this reason, we designed and built a special device, which raises the potential beam energy, without altering any other beam parameters. We call this final component of the SPM interface *Positron Elevator*. In the following sections we discuss the advantage of a positron elevator compared to a high frequency accelerator, when considering the best option to keep the positron beam quality.

The functional principle of the elevator was already proposed by G. Kögel and P. Sperr in 1997 [106]. In the same year, D. Passbach investigated the feasibility for an elevator resonator concept in the context of a seminar work at the *Institut für nukleare Festkörperphysik LRT2* [107]. Subsequently, R. Ernst considered the technical capabilities for the elevator in his diploma thesis in 2005 [108]. Following this, a detailed proposal for the elevator was given in 2006 [109].

Since the SPM interface transfers the NEPOMUC beam into a beam of higher brightness, the elevator must not influence other beam parameters, or even destroy the high beam quality. From the source diameter of $d_{\mathrm{s}} = 3$ mm FWHM and $E_{\perp} = 30$ meV FWHM [39], we can determine the phase space volume of the SPM laboratory setup as $\Omega_{rr} = 666$ mm^{2}meV$\cdot m_{\mathrm{e}}$. Since the interface replaces the source column of the SPM,

the occupied phase space volume after the elevator must be at least in the same order of magnitude to verify a proper operation of the microscope.

It has been possible, in the context of this work, to build the whole device and operate it with the NEPOMUC beam as final component of the SPM interface. We present in the following section the elevator principle, the technical implementation and measurement results of the elevated and non-elevated beam. Furthermore, we show that a positron elevator is valuable for all positron beam systems, since it is possible to change the beam energy although source and sample can be biased on the same electric potential. Some of the results have been already published in [99, 110].

5.1 Functional Principle of a Positron Beam Elevator

A diagram of the elevator principle is shown in Figure 5.1. The setup bases on a sine wave double-gap buncher or a conventional high frequency Alvarez accelerator. This device would accelerate the positrons on both gaps with a maximum electric field. However, in case of the elevator the sine wave voltage is shifted by $-T/4$ with respect to the beam pulses. Therefore, the pulsed beam passes the gaps, when they are field-free. This guarantees a prevention of a lens behavior at both gaps. According to Equation 3.34, a field difference of 5 kV would lead to strong lens effects with a focal length in the range of ≈ 10 mm. In this case, the lens aberrations would affect the beam quality in such a negative way that it would never be possible to correct these effects afterwards.

In order to overcome these problems, the elevator is adjusted as follows: We bias the entrance and exit electrode on the static potentials U_{in} and U_{out}, as required to transform the beam potential from the second remoderator to the potential, necessary for a further beam transport to the SPM. The static potential of the central electrode is superimposed by a time dependent sine wave voltage

$$U_{\mathrm{c}} = U_0 + U(t) = U_0 + A\sin(2\pi f \cdot t + \varphi) \tag{5.1}$$

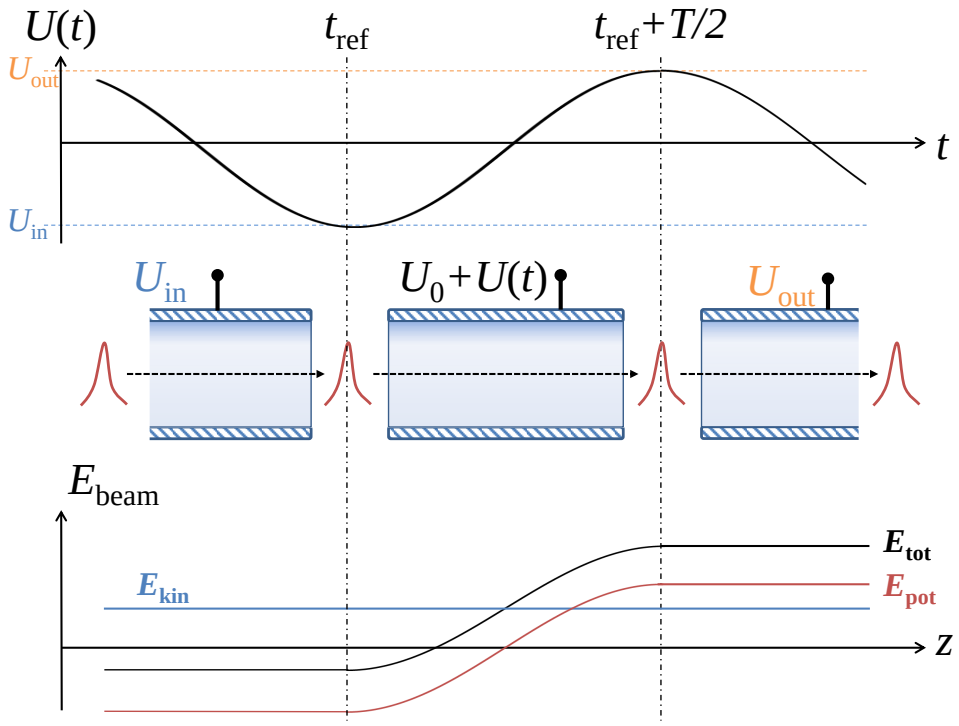

Figure 5.1: Functional principle of the positron beam elevator.

with amplitude A and frequency $f = 1/T$. The length of the central electrode L is adapted to the kinetic beam energy. The particles must pass it within half a period:

$$L = \sqrt{\frac{E_{\mathrm{kin}}}{2 \cdot m_{\mathrm{e}}}} \cdot T \tag{5.2}$$

We bias the static potential of the central electrode symmetrically between the other potentials:

$$U_0 = \frac{U_{\mathrm{in}} + U_{\mathrm{out}}}{2} \tag{5.3}$$

In order to reach field-free gaps, the amplitude has to be adjusted with respect to entrance and exit potential:

$$A = \frac{|U_{\mathrm{in}}| + |U_{\mathrm{out}}|}{2} \tag{5.4}$$

Together with Equation 5.1 and 5.3 we obtain:

$$U_{\mathrm{c}} = \frac{1}{2}\left[U_{\mathrm{in}} + U_{\mathrm{out}} + (|U_{\mathrm{in}}| + |U_{\mathrm{out}}|)\sin(2\pi \cdot f \cdot t + \varphi_{\mathrm{e}})\right] \tag{5.5}$$

The signal phase φ must be precisely adapted to the repetition rate of the beam so that the pulses enter the first gap, when $U_{\mathrm{c}} = U_{\mathrm{in}} = U_0 - A$. By adjusting all parameters, we achieve an increase of the potential beam energy by

$$\Delta E_{pot} = 2eA\,, \tag{5.6}$$

while the kinetic beam energy stays constant.

Although the elevator principle is simple, the technical implementation is more difficult. We present in the following section the constrictions for the elevator, caused by the SPM system and the solutions, which we found to overcome serious problems.

5.2 Design

The elevator is the final component, which connects the SPM interface with the microscope. The goal is to raise the potential beam energy by 10 keV. For this, we need a minimal voltage amplitude of $A = 5$ kV. The working frequency is defined by the pulsing frequency of the SPM interface, which is 50 MHz. Additionally, the space between interface and SPM is confined to 267 mm. Thus, the length of the central electrode, which correlates with the kinetic beam energy, is also limited. Because of these constrictions, we decided to design the elevator as shown in Figure 5.2.

The 146-mm-long central electrode is designed for a kinetic beam energy of 600 eV. The voltage signal is inductively coupled by a coil, which we placed on the axis of the resonator coil, in a distance of 30 mm. The resonator coil is connected to the central electrode. Both form a RLC circuit. The resonance frequency of the circuit is adjusted to 50 MHz in order to amplify the signal. In that way, we achieve a high amplitude without using high-power voltage, which would heat up the components considerably. In addition, the resonator coil is placed outside the vacuum chamber, because it is much easier to cool. This prevents length variation as a consequence of heating, since the resonance frequency changes significantly with the coil length.

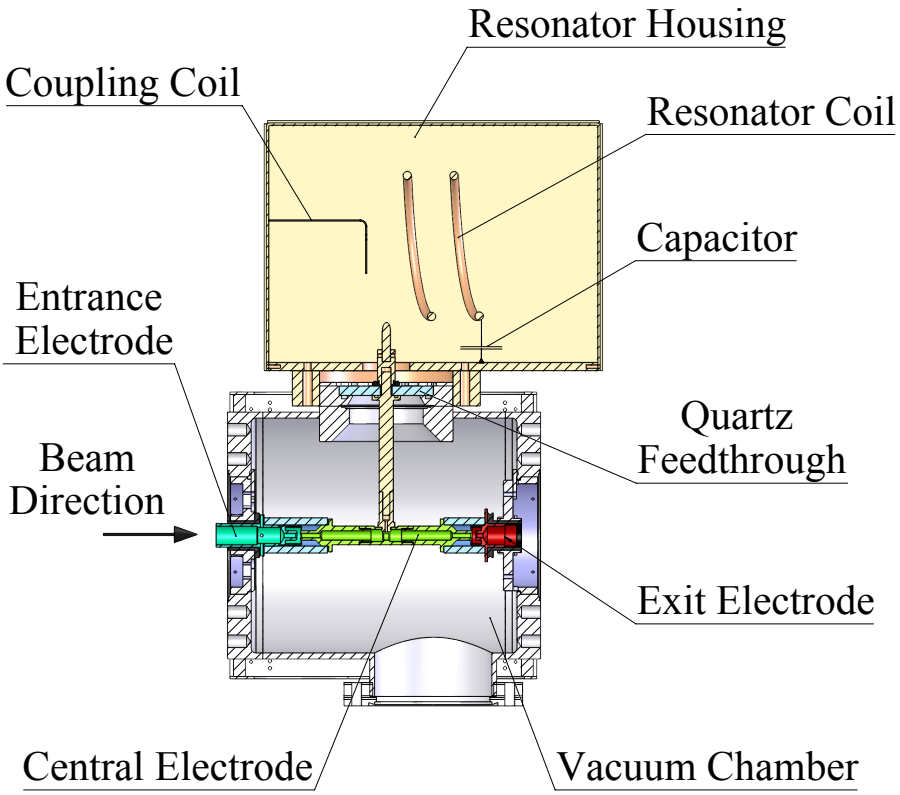

Figure 5.2: Technical drawing of the elevator setup.

The elevator setup is also favorable since we can adjust the energy elevation by regulating the amplitude of the coupled voltage. The voltage amplification depends on the Q-factor of the resonator, which is defined as the fraction of stored energy W and the lost energy V per cycle [111]:

$$Q = 2\pi \frac{W}{V} \tag{5.7}$$

Using the expressions

$$W = \frac{1}{2} C_{\mathrm{tot}} A^2 \tag{5.8}$$

$$V = \frac{A^2}{R} \frac{1}{f_0} = \frac{P}{f_0}\,, \tag{5.9}$$

we obtain:

$$Q = \frac{\omega_0 C_{\mathrm{tot}}}{2P} A^2 \tag{5.10}$$

Here, $\omega_0 = 2\pi f_0$ is the resonance frequency, C_{tot} the total capacity of the circuit and P the source power. With this equation, we can estimate a Q-factor, which we must reach in order to raise the potential beam energy by 10 keV ($A = 5$ kV). We use a 50 MHz power supply with a maximum output power of 20 W. The total capacity can be reduced by the geometry of the components. Therefore, we lowered the diameter of the electrodes at the gap to 4 mm. In addition, the diameter of the central electrode is as low as possible to decrease the capacitance to the vacuum chamber. Altogether, we reach a total capacity of $C_{\mathrm{tot}} \approx 20$ pF. We can estimate the necessary Q-factor for these values as:

$$Q \approx 4000$$

Figure 5.3 shows the Q-factor for different amplitudes as a function of the source power. It is evident that we achieve a higher energy elevation if we use more power. However, more power leads to a stronger heating of the system. Latest results show that the resonance frequency stays constant for 20 W with a simple air cooling. The heating increases linearly with the source power, whereas the thermal resistance stays constant. This means that the coil temperature increases and we have to further cool the system when increasing the dissipated power. Therefore, an increase of the amplitude by a higher source power is only a secondary solution.

Although it is easier to cool the resonator coil outside the vacuum chamber, this solution leads to another problem: The feedthrough, which connects resonator coil and central electrode means an additional capacitance in the system. A high C_{tot} decreases the voltage on the central electrode. In addition, the dielectric material of the feedthrough

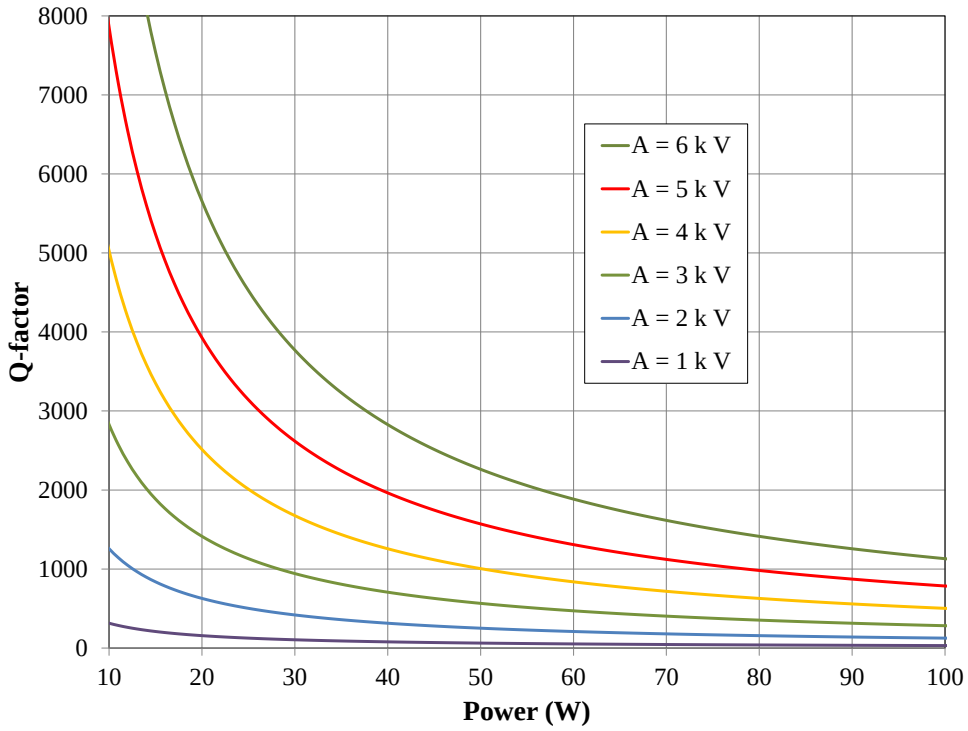

Figure 5.3: Q-factor for different amplitudes A as a function of the source power (C_{tot} = 20 pF).

leads to further losses. To solve both problems, we designed a CF63 flange, where a quartz window fixes the 10 mm feedthrough in the center. The dielectric dissipation factor for quartz is in the range of $\tan\delta \approx 10^{-4}$ [112], which is very low in contrast to other materials. For the same reason we use quartz tubes between the three electrodes, to keep the gap space of 3 mm. This gap width has been chosen, to avoid sparking and, therefore, voltage flashovers between the electrodes. Wide gaps are also of advantage, since its lowers the total capacity. However, we must ensure that the transit time of the pulse through both gaps is as low as possible. As a compromise we chose a gap width of 3 mm.

With these parameters we can now calculate the beam perturbation at the elevator gap, according to Chapter 3.6.1. Figure 5.4 presents the effects on the beam divergence. We find that the opening angle stays almost constant for a wide range of the incident beam divergence. However, it changes considerably with the particle distance from the optical axis. This perturbation can not be undone afterwards and leads to an enormous decrease of the beam quality. A modification of the beam divergence in the range of $\Delta\alpha \approx 10^{-3}$ would increase the beam spot size on the final remoderator by a factor 10. With this, we would never reach a spatial resolution of 1 µm for the SPM. However,

we see in Figure 5.4 that the modification of $\Delta\alpha$ is symmetrical to $x_0 = 0$. This means that the perturbation can be compensated, if a positron enters the first gap above and the second gap below the optical axis, or the other way around. This can be achieved, by focusing the particles in the center of the central electrode, where the beam crosses and leaves the second gap turned.

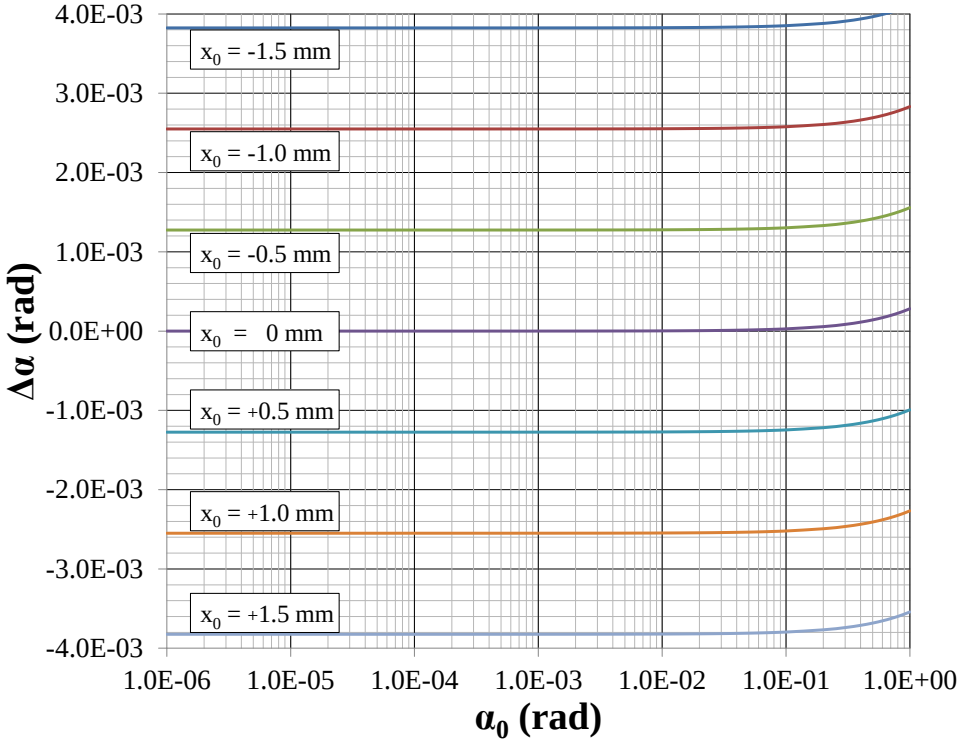

Figure 5.4: Change of the opening angle for different distances x_0 from the optical axis as a function of the beam divergence α: The curves are calculated with Equation 3.100 and $\Delta\alpha = \Delta v_x / v_{\|}$, $f = 50$ MHz, $E_{\|} = 600$ eV, $t_n = 181$ ps, $\Delta U_{\text{stat}} = 5$ kV, $d = 5$ mm.

5.3 Setup of the Elevated Beam Characterization

Figure 5.5 depicts the measurement setup for the first elevator tests. To guide the beam through the whole setup, we suppress the RF signal and bias all elevator electrodes on the same electric potential so that the beam energy stays constant at $E_{\|} = 600$ eV. We use a lens system, which is placed at the end of the buncher drift, to focus the pulsed beam into the central electrode. To ensure a beam crossing in the center, we place the detector at position 1 and measure time spectra at different lens settings. Since the

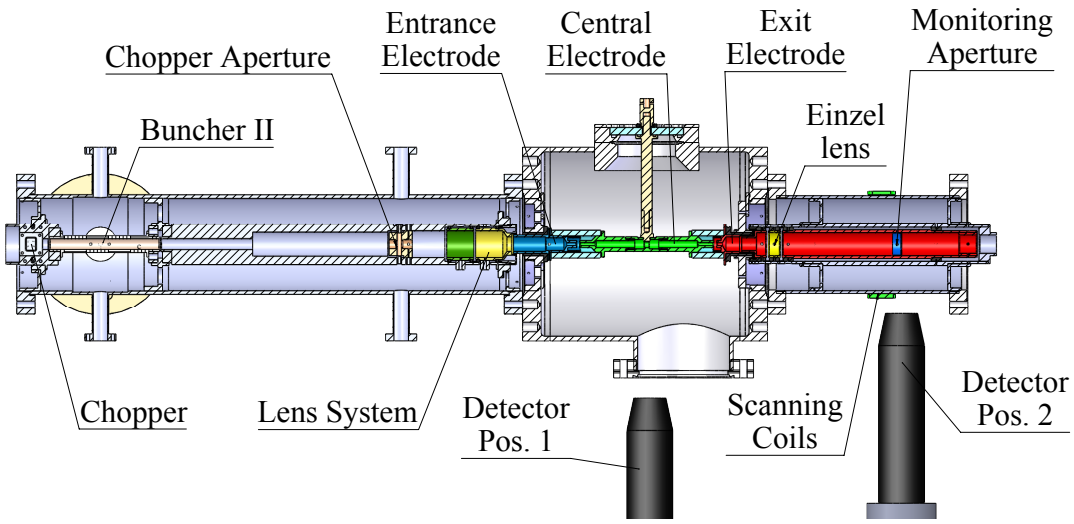

Figure 5.5: Setup for first elevator test measurements: The pulsed beam is focused with an electrostatic lens system in the center of the central electrode. The Einzel lens images this crossover one-to-one on a monitoring aperture, where we detect the annihilation radiation. To determine the beam size, we can scan the beam over this aperture by two pairs of scanning coils.

electrode diameters at both gaps are constricted, parts of the beam annihilate at these positions. We present the corresponding spectra in Figure 5.6. The annihilation at both gaps is clearly visible. In addition, we find that the beam passes the central electrode within 10 ns, which verifies a correct adjusted particle velocity. Because of the limited space around the whole setup, it has not been possible to place the detector in a middle position between both gaps. Therefore, the detector is closer to the first gap and obtains more radiation from the entrance. This is the reason why the peaks of the spectra never show the same height. For all further measurements we apply Configuration 3.

For the first test measurements, we used a very simple, ready-made resonator with a low Q-factor of 80. For this, we can calculate the maximum energy elevation with Equation 5.10 as $\Delta E_{\mathrm{pot,max}} = 1.4$ keV. However, this is only achievable if we feed 100 % of the RF signal into the system. To ensure a high voltage coupling, we customized the couple coil to an impedance, where the signal reflection is as low as possible. Nevertheless, it was not possible to reach a 100 % coupling. Therefore, we have chosen an energy elevation of $\Delta E_{\mathrm{pot}} = 1.0$ keV for a first test.

To operate the elevator as desired, we bias all electrodes on the required potentials. For a first test, we mounted a special chamber behind the elevator, where we can investigate the main beam characteristics. We measure the annihilation radiation with the detector

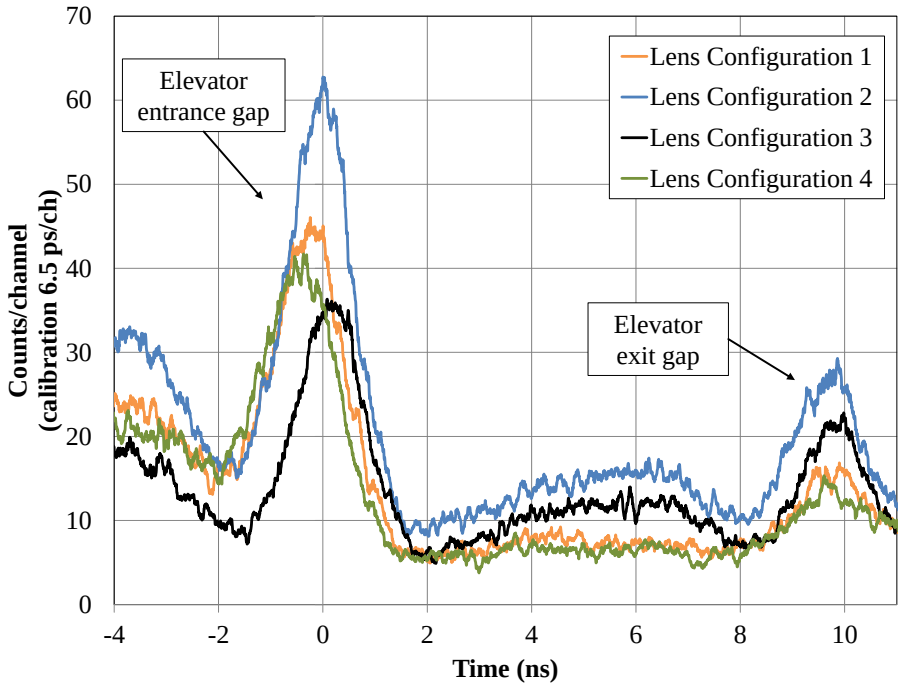

Figure 5.6: Time spectra for different lens settings: Parts of the beam annihilate at the electrode constrictions close to the gap. The particles transit the central electrode within 10 ns.

at position 2, where the beam hits a 12-mm, circular monitoring aperture. Since we are not able to measure the RF amplitude on the central electrode directly, we have to increase the coupled power stepwise, until the count rate rises. To verify a correct adjusted RF amplitude and, therefore, a desired energy lift, we use the Einzel lens as energy filter. Here, the electric potential can be increased until the beam is reflected. The corresponding voltage provides the total beam energy. Since the kinetic energy is known, we can directly conclude the potential energy.

To determine the spatial beam size, we scan the beam with two pairs of scanning coils over the monitoring aperture in x and y direction. From the detected count rate, we obtain a two-dimensional image of the aperture and infer the beam size.

5.4 Results

To investigate the elevator influences on the time structure, we used the scanning coils to deflect the 1keV-elevated and non-elevated beam on the monitoring aperture. The detector is placed behind a led shield at position 2. Figure 5.7 depicts the respective time

spectra. Since the elevator does not modulate the longitudinal velocity, the peaks of both spectra should appear at the same point in time. However, we find a time deviation of about 0.7 ns, which corresponds to a kinetic energy modulation of 56 eV. Therefore, the amplitude or the phase of the RF signal is not adjusted sufficiently. The voltage at both gaps is by 28 V too low. For a better visualization the curves are put on the top of each other. Nevertheless, the influences on the pulse shape keep within reasonable limits. The pulse of the elevated beam is broadened at the bottom side. This asymmetrical effect confirms the consideration of a slightly wrong adjusted RF signal. If the influences would be symmetrical, we could consider that the pulse transition time at both gaps is too high.

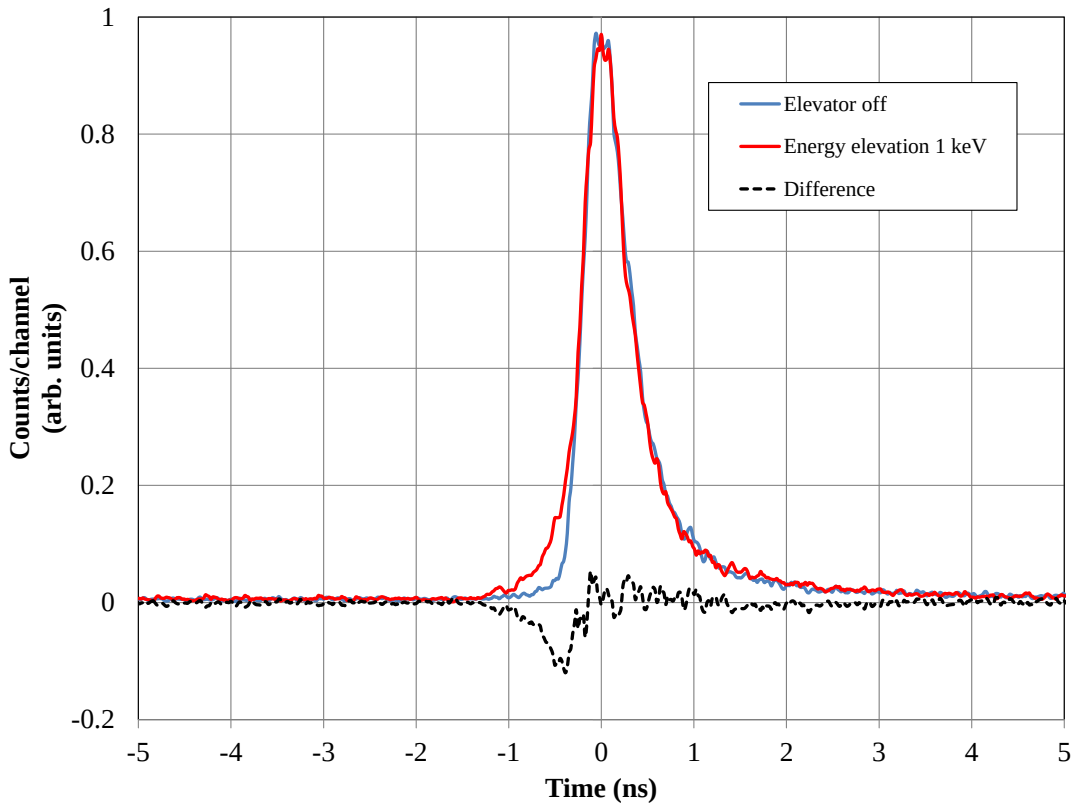

Figure 5.7: Time spectra of the 1keV-elevated and non-elevated beam: The time deviation of the raw spectra is about 0.7 ns. For a better visualization the curves are shifted on the top of each other.

In order to investigate the elevator influences on the beam's phase space, we scanned the beam over the monitoring aperture and measured the count rate at particular positions. In this way, we obtain a two-dimensional image of the aperture, shown in Figure 5.8. However, although we shield the detector from background radiation, the image

is blurred by positrons, which annihilate before or after the aperture. Therefore, the circular aperture is blurred and it is not possible to investigate the beam size.

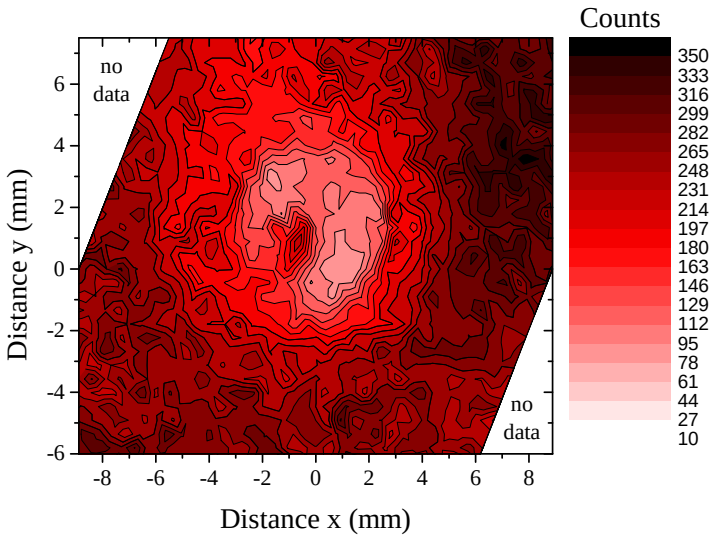

Figure 5.8: Count map from a scan over the monitoring aperture: The image includes 1225 positron lifetime spectra; the step width is about 0.25 mm. Each pixel represents the count rate, measured by the detector, for a certain position of the beam. Although the detector is shielded, radiation from positrons, which annihilate before or after the aperture, blurs the image.

If we want to analyze the beam characteristics, we have to separate the annihilation radiation of positrons on the monitoring aperture from the background. To this end, a pulsed beam is of great advantage, since the time stamp allows to detect the origin of the radiation. Figure 5.9 shows a map of the mean annihilation time. This picture is directly obtained from the same spectra as we used for Figure 5.8. Since every pixel represents a lifetime spectrum, we can determine the mean annihilation time, with respect to a reference time. The picture shows that the events in the center occur 5 ns later than on the aperture. This means that the positrons pass the aperture and annihilate up to 7.3 cm behind. This is due to the solid angle between detector and aperture. Since we had to place the detector outside the vacuum chamber, we can not completely shield the detector of background events. However, we are able to remove them from the data afterwards.

Figure 5.10 shows a count rate map of the aperture, where all events are removed, which do not occur in a time window of $\pm$ 0.75 ns. Here, the 12 mm aperture is clearly identifiable. The edges of the aperture image show that the beam is elliptically distorted.

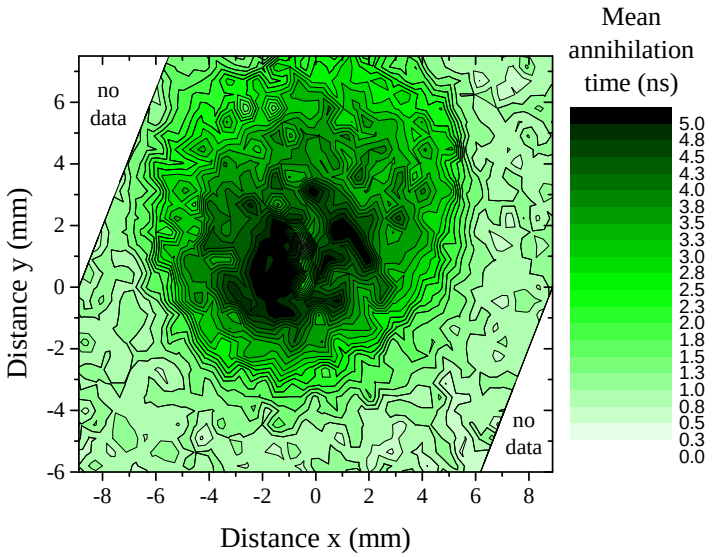

Figure 5.9: Mean annihilation time map of the aperture scan: Events in the center occur for up to 5 ns later in the spectra than on the aperture. This background is caused by positrons, which pass the aperture and annihilate behind.

However, this is not caused by influences from the elevator. The elliptic beam profile was already obtained directely after the NEPOMUC remoderator [88, 110].

To measure the transverse phase space of the beam in the first approximation, we use two different settings for the Einzel lens. The first setting images the beam crossover from the center of the elevator onto the monitoring aperture on a scale of 1:1. For the second setting we bias the Einzel lens on the same potential as the exit electrode. Thus, the lens is not excited and the beam can propagate freely. We present the respective beam paths in Figure 5.11.

We scan for both settings the beam over the aperture and obtain count rate maps as described. The results are presented in Figure 5.12. We indicated in the maps the short and long axis of the elliptically shaped beam, respectively. On the basis of these results, we scanned the beam on the tagged lines over the aperture. The line scans for both lens settings are shown in Figure 5.13.

From this measurements we obtain the radii for the free and focused beam as:

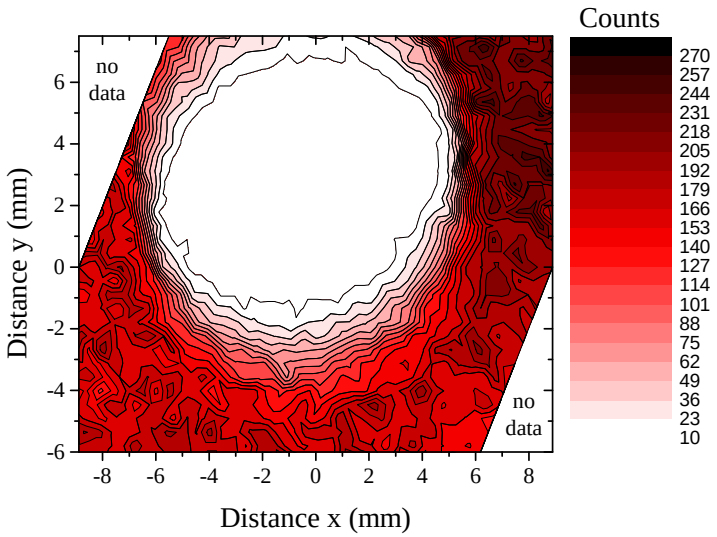

Figure 5.10: Filtered map of the aperture scan: All events, which do no occur in a time window of $\pm$ 0.75 ns have been removed.

$$r_{\text{free}} = \frac{1}{2}\sqrt{d_{\text{s,free}} \cdot d_{\text{l,free}}} = \frac{1}{2}\sqrt{2.7\text{ mm} \cdot 2.3\text{ mm}} \qquad = 1.25\text{ mm} \tag{5.11}$$

$$r_{\text{foc}} = \frac{1}{2}\sqrt{d_{\text{s,foc}} \cdot d_{\text{l,foc}}} = \frac{1}{2}\sqrt{1.1\text{ mm} \cdot 1.4\text{ mm}} \qquad = 0.62\text{ mm} \tag{5.12}$$

With the distance $L_i = 276$ mm from elevator center to the monitoring aperture we find for the divergence angle

$$\alpha = \arctan\left(\frac{\Delta r}{L_i}\right) = \arctan\left(\frac{r_{\text{free}} - r_{\text{foc}}}{L_i}\right) = 2.28 \cdot 10^{-3} = 2.28\text{ mrad} \tag{5.13}$$

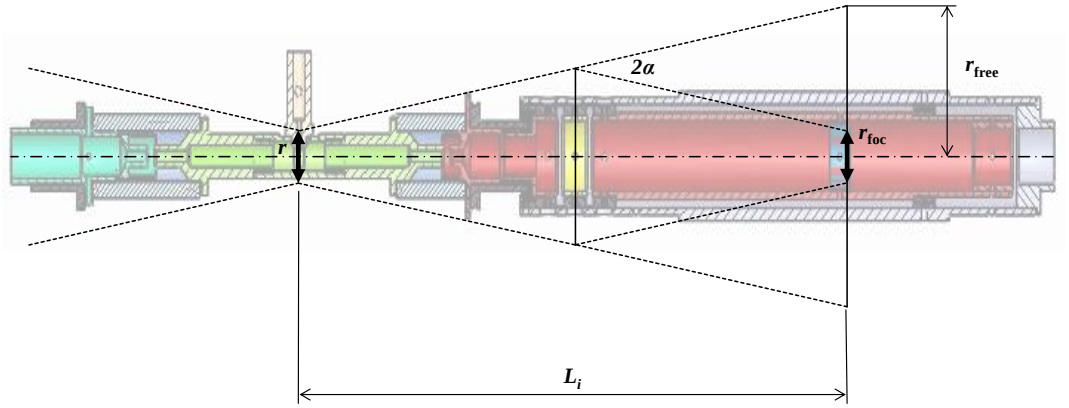

Figure 5.11: Beam paths for two different lens settings: If the Einzel lens (yellow) is not excited, the beam propagates freely. Otherwise it images the beam crossover approximately onto the monitoring aperture on a scale of ≈ 1:1.

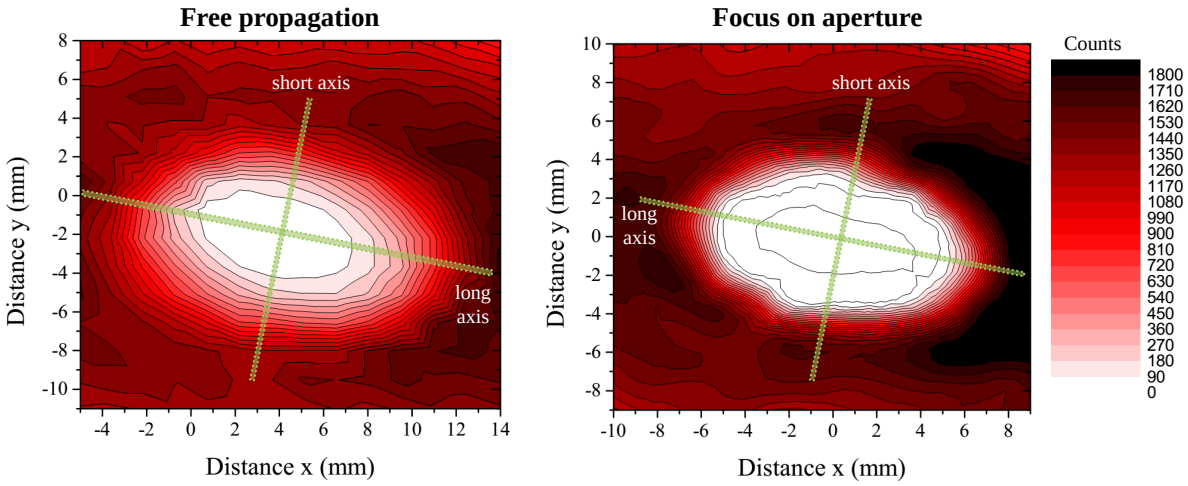

Figure 5.12: Count maps detected at the monitoring aperture for the free and focused beam: The beam is elliptically distorted. The marked regions for the long and the short axis are used to determine the spatial beam sizes.

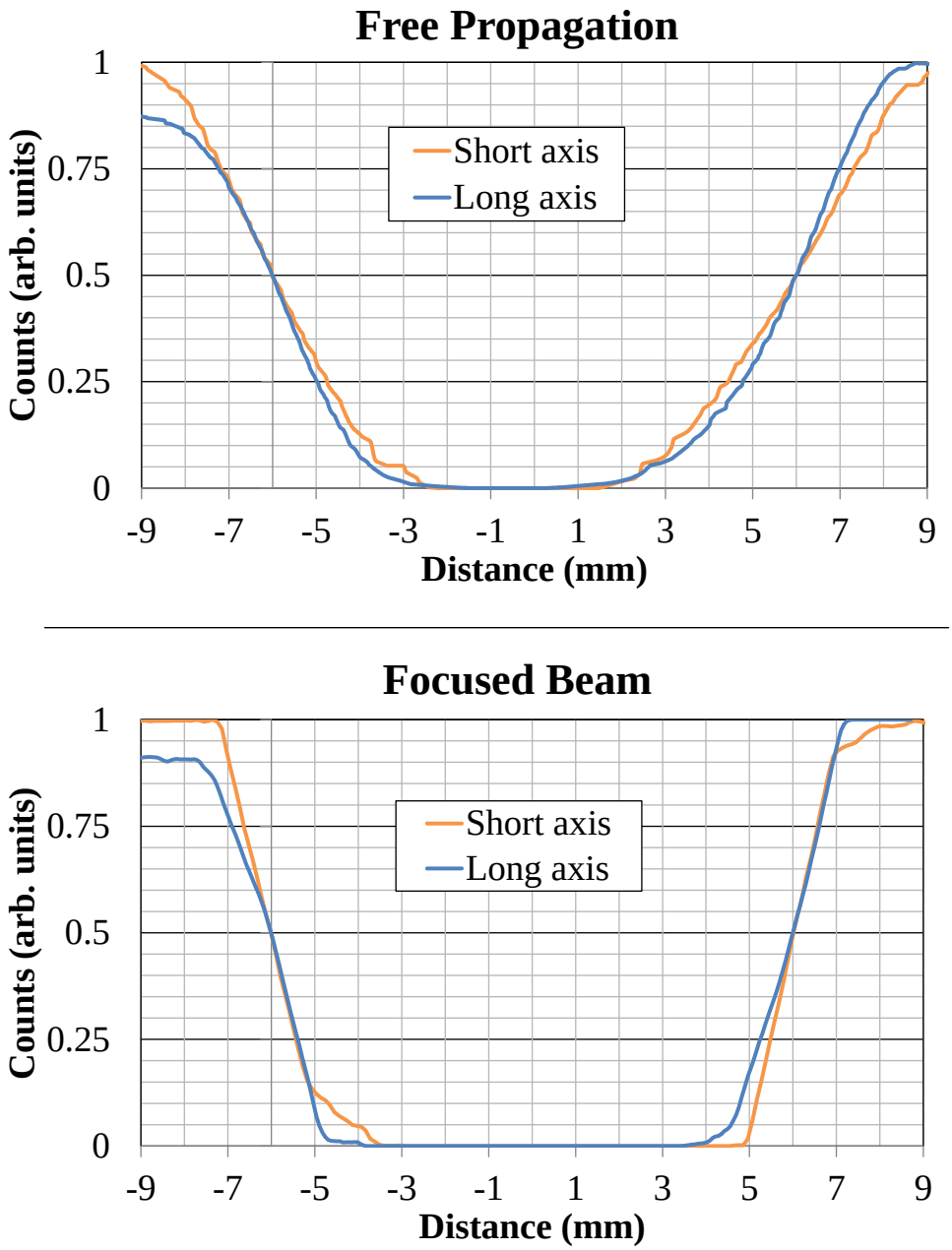

Figure 5.13: Line scans over the monitoring aperture for both lens settings: The respective regions are indicated in Figure 5.12. We obtain the beam diameters FWHM as as $d_{\mathrm{s,free}}$ = 2.7 mm and $d_{\mathrm{l,free}}$ = 2.3 mm for the freely propagating beam and $d_{\mathrm{s,foc}}$ = 1.1 mm and $d_{\mathrm{l,foc}}$ = 1.4 mm for the focused beam.

Finally, we obtain for the values

$$\alpha^2 = 5.20 \cdot 10^{-6} \tag{5.14}$$

$$r^2 = 0.38 \text{ mm}^2 \tag{5.15}$$

$$E_{\parallel} = 600 \text{ eV} \tag{5.16}$$

the full transverse phase space of the 1-keV-elevated beam as:

$$\Omega_{rr} = \frac{1}{2}\,\pi^2 \cdot r^2 \cdot p_{\perp}^2 = \pi^2 \cdot r^2 \cdot \alpha^2 \cdot E \cdot m_{\mathrm{e}} = 11.8 \text{ mm}^2 \text{ meV} \cdot m_{\mathrm{e}} \tag{5.17}$$

To the best of our knowledge, beam characterization by joint positron and time-of-flight measurements has been performed in this work for the first time in positron beam systems.

6 Conclusion and Outlook

In the present work, the SPM interface was re-assembled and connected with NEPOMUC in order to operate the SPM at the research reactor FRM II in the near future. The final component of the interface is the positron elevator, which increases the potential beam energy on a required level. To obtain applicable results, all components of the whole system have to work properly. Since the SPM necessitates a high beam quality, we characterize the properties of the brightness-enhanced and elevated beam. Furthermore, a computer-assisted algorithm was developed to minimize the losses of beam intensity along the beam path.

The improved pulsing system compresses approximately 50 % of the beam intensity with respect to the continuous beam, in a positron pulse of about 360 ps FWHM, within a time window of 20 ns. The obtained spectra show a peak to background ratio of roughly 1000:1. The additional re-moderation stage of the SPM interface reaches an efficiency of $\approx$ 23 % and increases the complete transverse phase space density of the beam by a factor 350. The novel, computer-assisted algorithm, shortened the beam adjustment time of up to one week to several hours. With a specially constructed sample chamber it was possible to perform first spatially resolved PALS at the FRM II with the SPM interface. The achieved beam spot size on the sample is in the range of 180 µm, using the magnetic single-pole lens of the microscope remoderator. Additionally, we used this setup to apply two newly developed detectors, which enable to obtain first four-dimensional positron age momentum correlation spectra.

In the context of this work, the positron elevator has been designed, build and implemented. With the current setup and a provisional resonator we achieve a total energy elevation of 1 keV. The corresponding time spectra show that influences on the beam's time structure can be neglected. Furthermore, it is possible to operate the elevator with almost no losses of beam intensity. The determined complete transverse phase space of $\Omega_{rr} = 12$ mm^{2}meV$\cdot m_\mathrm{e}$ show the high quality of the elevated beam, which benefits the future operation of the SPM at NEPOMUC. However, the Q-factor of the elevator res-

onator has to be improved in order to reach higher energies. Nevertheless, it is shown that both, elevator concept and design, work. Finally, we can conclude that the elevator is a favorable extension for many positron beam facilities, since it offers the possibility to bias source and sample on the same electric potential.

Using the BaF_2 detector system, we achieve a maximum count rate of 1800 Hz on the monitoring aperture behind the positron elevator. This value corresponds to a number of $1.2 \cdot 10^6$ positrons per second. The positron losses inside the following microscope are mainly caused by the final remoderator. We have determined an re-moderation efficiency of 23 % for the interface remoderator. Assuming a similar efficiency for the final remoderator, we will obtain count rates up to 7000 Hz for the SPM, using the same detector system in a distance of 40 mm from the sample position. This result shows that the count rate of the SPM at NEPOMUC will by a factor 14 higher compared to the laboratory operation. This will reduce future measurement times considerably. As an example: The SPM image of the fatigue crack, shown in Chapter 2.6.2, took a measurement time of 1 week. At NEPOMUC this measurement time will be reduced to about a half day.

For the characterization of the elevated beam, a novel time-of-flight method has been developed and applied for the first time. The 1-keV-elevated beam shows a transverse phase space volume of $\Omega_{rr} = 12$ mm^{2}meV$\cdot m_\mathrm{e}$. This value is by a factor 56 smaller than the 666 mm^{2}meV$\cdot m_\mathrm{e}$ of the SPM laboratory beam. According to [42] the beam spot size on the SPM remoderator was 20 µm using the ^{22}Na source. Since Ω_{rr} scales with d^2, we predict a remoderator spot size of ≈ 3 µm for the SPM at NEPOMUC. For this prediction, the spatial resolution of the microscope will be improved to about 0.3 µm.

All results together show that the implementation of the SPM at NEPOMUC enhances considerably the performance of the whole device. With the final system, spatially resolved PALS will be accessible for modern material science. However, the measurement time as well as the spatial resolution of the microscope can be still progressed by the improvement of the NEPOMUC remoderator. Anyway, the capabilities of the SPM will be applied in a wide field of research after the transfer to NEPOMUC, even with the present performances.

Minor modifications in those parts of the chain from NEPOMUC to SPM, which are not an object of the present work, will improve the SPM considerably. As shown in Chapter 4.3, improving the first remoderator to the level of the second one, will enhance

the event rate by a factor of 10 and the spatial resolution by a factor of 3. However, attempts to do so should be postponed until more experience with the entire system is available.

List of Publications

1. Positron Beam Characterization at the Scanning Positron Microscope Interface
   J. Mitteneder, **M. Dickmann**, G. Kögel, W. Egger, P. Sperr, G. Dollinger
   Journal of Physics: Conf. Series **791** (2017) 012006

2. New Insights into the Nanostructure of Innovative Thin Film Solar Cells Gained By Positron Annihilation Spectroscopy
   S. W. H. Eijt, W. Shi, A. Mannheim, M. Butterling, H. Schut, W. Egger, **M. Dickmann**, C. Hugenschmidt, B. Shakeri, R. W. Meulenberg, V. Callewaert, R. Saniz, B. Partoens, B. Barbiellini, A. Bansil, J. Melskens, M. Zeman, A. H. M. Smets, M. Kulbak, G. Hodes, D. Cahen, E. Brück
   Journal of Physics: Conf. Serie **791** (2017) 012021

3. Four-Dimensional Positron Age-Momentum Correlation
   U. Ackermann, B. Löwe, **M. Dickmann**, J. Mitteneder, P. Sperr, W. Egger, M. Reiner, G. Dollinger
   New Journal of Physics **18** (2016) 113030

4. Radio Frequency Elevator For a Pulsed Positron Beam
   M. Dickmann, J. Mitteneder, G. Kögel, W. Egger, P. Sperr, U. Ackermann, C. Piochacz, G. Dollinger
   Nuclear Instruments and Methods in Physics Research A **821** (2016) 40–43

5. SPM: Scanning Positron Microscope
   M. Dickmann, C. Piochacz
   Journal of Large-Scale Research Facilities JLSRF **1** (2015) 26

6. Demonstration of the Monolithic Interconnection on CIS Solar Cells by Picosecond Laser Structuring on 30 by 30 cm^2 Modules
   G. Heise, A. Börner, **M. Dickmann**, M. Englmaier, A. Heiss, M. Kemnitzer, J.

Konrad, R. Moser, J. Palm, H. Vogt, H. P. Huber
Prog. Photovolt: Res. Appl. **23.10** (2015) 1291–1304

7. INVESTIGATION OF THE ABLATION OF ZINC OXIDE THIN FILMS ON COPPER-INDIUM-SELENIDE LAYERS BY PS LASER PULSES
G. Heise, **M. Dickmann**, M. Domke, A. Heiss, T. Kuznicki, J. Palm, I. Richter, H. Vogt, H. P. Huber
Applied Physics A **104.1** (2011) 387–393

8. APPLICATION OF INDUCED LASER ABLATION WITH ULTRA SHORT PULSE LASERS FOR HIGH SPEED THIN FILM SOLAR CELL PROCESSING
G. Heise, **M. Dickmann**, J. Konrad, I. Richter, S. Sarrach, A. Heiss, H. Vogt, H. P. Huber
Proceedings of 29th ICALEO **1199** (2010)

Bibliography

[1] Paul AM Dirac. A theory of electrons and protons. In *Proceedings of the Royal Society of London A: Mathematical, Physical and Engineering Sciences*, volume 126, pages 360–365. The Royal Society, 1930.

[2] Carl D Anderson. Energies of cosmic-ray particles. *Physical Review*, 41(4):405, 1932.

[3] Carl D Anderson. The positive electron. *Physical Review*, 43(6):491, 1933.

[4] Peter J Mohr, Barry N Taylor, and David B Newell. CODATA recommended values of the fundamental physical constants: 2006a). *Journal of Physical and Chemical Reference Data*, 37(3):1187–1284, 2008.

[5] Paul G Coleman. *Positron beams and their applications*. World Scientific, 2000.

[6] R Krause-Rehberg, F Börner, F Redmann, W Egger, G Kögel, P Sperr, and W Triftshäuser. Improved defect profiling with slow positrons. *Applied surface science*, 194(1):210–213, 2002.

[7] Peter J Schultz and Kelvin G Lynn. Interaction of positron beams with surfaces, thin films, and interfaces. *Reviews of Modern Physics*, 60(3):701, 1988.

[8] J Makinen, S Palko, J Martikainen, and P Hautojärvi. Positron backscattering probabilities from solid surfaces at 2-30 keV. *Journal of Physics: Condensed Matter*, 4(36):L503, 1992.

[9] H Huomo, A Vehanen, MD Bentzon, and P Hautojärvi. Positron diffusion in Mo: The role of epithermal positrons. *Physical Review B*, 35(15):8252, 1987.

[10] DT Britton, PC Rice-Evans, and JH Evans. Epithermal effects in positron depth profiling measurements. *Philosophical magazine letters*, 57(3):165–169, 1988.

[11] Allen P Mills. Thermal activation measurement of positron binding energies at surfaces. *Solid State Communications*, 31(9):623–626, 1979.

[12] AF Makhov. The penetration of electrons into solids. 2. The Distribution of electrons in depth. *SOVIET PHYSICS-SOLID STATE*, 2(9):1942–1944, 1961.

[13] S Valkealahti and RM Nieminen. Monte Carlo calculations of keV electron and positron slowing down in solids. II. *Applied Physics A*, 35(1):51–59, 1984.

[14] John Algers, Peter Sperr, Werner Egger, Gottfried Kögel, and Frans HJ Maurer. Median implantation depth and implantation profile of 3–18 keV positrons in amorphous polymers. *Physical Review B*, 67(12):125404, 2003.

[15] J Keinonen, M Hautala, E Rauhala, V Karttunen, A Kuronen, J Räisänen, J Lahtinen, A Vehanen, E Punkka, and P Hautojärvi. Defect formation in H implantation of crystalline Si. *Physical Review B*, 37(14):8269, 1988.

[16] Martti J Puska and RM Nieminen. Theory of positrons in solids and on solid surfaces. *Reviews of modern Physics*, 66(3):841, 1994.

[17] JA Baker, NB Chilton, Kjeld O Jensen, AB Walker, and PG Coleman. Material dependence of positron implantation depths. *Applied physics letters*, 59(23):2962–2964, 1991.

[18] Allen P Mills Jr and Robert J Wilson. Transmission of 1-6-kev positrons through thin metal films. *Physical Review A*, 26(1):490, 1982.

[19] A Vehanen, K Saarinen, P Hautojärvi, and H Huomo. Profiling multilayer structures with monoenergetic positrons. *Physical Review B*, 35(10):4606, 1987.

[20] Kjeld O Jensen and Alison B Walker. Monte Carlo simulation of the transport of fast electrons and positrons in solids. *Surface science*, 292(1):83–97, 1993.

[21] Stephan Berko and Hugh N Pendleton. Positronium. *Annual Review of Nuclear and Particle Science*, 30(1):543–581, 1980.

[22] Andrzej Czarnecki and Savely G Karshenboim. Decays of positronium. *arXiv preprint hep-ph/9911410*, 1999.

[23] Roy Neil West. Positron studies of condensed matter. *Advances in Physics*, 22(3):263–383, 1973.

[24] P Hasbach, G Hilkert, E Klempt, and G Werth. Experimental determination of the ortho-positronium lifetime in vacuum. *Il Nuovo Cimento A Series 11*, 97(3):419–425, 1987.

[25] T Goworek, K Ciesielski, B Jasińska, and J Wawryszczuk. Positronium states in the pores of silica gel. *Chemical physics*, 230(2):305–315, 1998.

[26] P Hautojärvi and C Corbel. Positron spectroscopy of defects in metals and semiconductors. *Positron spectroscopy of solids*, 125:491–532, 1995.

[27] W Egger. Pulsed low-energy positron beams in materials sciences. *Proc. Int. School of Physics Enrico Fermi Course CLXXIV - Physics with many positrons*, pages 419–449, 2010.

[28] KF Canter, GR Brandes, TN Horsky, PH Lippel, and AP Mills Jr. The high brightness beam at Brandeis. In *Atomic Physics with Positrons*, pages 153–160. Springer, 1987.

[29] Léon J Seijbel, RFJ Neelissen, P Kruit, A Van Veen, and H Schut. Coupling optics for a combined electron positron scanning microscope. *Applied surface science*, 85:92–97, 1995.

[30] H Greif, M Haaks, U Holzwarth, U Männig, M Tongbhoyai, and Karin Maier. A Combined Positron Microprobe-Scanning Electron Microscope for Positron-Annihilation Spectroscopy with a Spatial Resolution in the Micron Range. In *Materials Science Forum*, volume 255, pages 641–643. Trans Tech Publ, 1997.

[31] H Greif, M Haaks, U Holzwarth, U Männig, M Tongbhoyai, T Wider, K Maier, J Bihr, and B Huber. High resolution positron-annihilation spectroscopy with a new positron microprobe. *Applied physics letters*, 71(15):2115–2117, 1997.

[32] A Zecca, RS Brusa, MP Duarte-Naia, GP Karwasz, J Paridaens, A Piazza, G Kögel, P Sperr, DT Britton, K Uhlmann, et al. A pulsed positron microbeam. *EPL (Europhysics Letters)*, 29(8):617, 1995.

[33] G Kögel et al. The München scanning positron microscope. *Applied surface science*, 116:108–113, 1997.

[34] W Triftshäuser, G Kögel, P Sperr, DT Britton, K Uhlmann, and P Willutzki. A scanning positron microscope for defect analysis in materials science. *Nuclear Instruments and Methods in Physics Research Section B: Beam Interactions with*

Materials and Atoms, 130(1):264–269, 1997.

[35] C Hugenschmidt. CDBS: coincident Doppler-broadening spectrometer. *Journal of large-scale research facilities JLSRF*, 1:23, 2015.

[36] T Gigl, C Piochacz, M Reiner, and C Hugenschmidt. Positronbeam for μm Resolved Coincident Doppler Broadening Spectroscopy at NEPOMUC. In *Journal of Physics: Conference Series*, volume 505, page 012032. IOP Publishing, 2014.

[37] A David. *Messungen mit dem weltweit ersten Rasterpositronenmikroskop*. PhD thesis, Universität der Bundeswehr München - Institute für Nukleare Festkörperphysik, 2000.

[38] RS Brusa, GP Karwasz, M Bettonte, and A Zecca. A high performance electrostatic positron beam. *Applied surface science*, 116:59–62, 1997.

[39] G Kögel. Private communication.

[40] P Willutzki, J Stormer, G Kögel, P Sperr, DT Britton, R Steindl, and W Triftshäuser. An improved pulsed low-energy positron system. *Measurement Science and Technology*, 5(5):548, 1994.

[41] P Sperr, G Kögel, P Willutzki, and W Triftshäuser. Pulsing of low energy positron beams. *Applied surface science*, 116:78–81, 1997.

[42] A David, G Kögel, P Sperr, and W Triftshäuser. Lifetime measurements with a scanning positron microscope. *Physical Review Letters*, 87(6):067402, 2001.

[43] W Egger, G Kögel, P Sperr, W Triftshäuser, S Rödling, J Bär, and H-J Gudladt. Vacancy clusters close to a fatigue crack observed with the München scanning positron microscope. *Applied surface science*, 194(1):214–217, 2002.

[44] Werner Triftshäuser. Positron microprobes. In *Materials Science Forum*, volume 445, pages 452–456. Trans Tech Publ, 2004.

[45] R Krause-Rehberg, F Börner, F Redmann, J Gebauer, R Kögler, R Kliemann, W Skorupa, W Egger, G Kögel, and W Triftshäuser. Identification of getter defects in high-energy self-implanted silicon at R p/2. *Physica B: Condensed Matter*, 308:442–445, 2001.

[46] W Egger, G Kögel, P Sperr, W Triftshäuser, J Bär, S Rödling, and H-J Gudladt. Measurements of defect structures of a cyclically deformed Al–Mg–Si

alloy by positron annihilation techniques. *Materials Science and Engineering: A*, 387:317–320, 2004.

[47] C Hugenschmidt. Positron sources and positron beams. *Proc. Int. School of Physics Enrico Fermi Course CLXXIV*, pages 399–418, 2010.

[48] William R Leo. *Techniques for nuclear and particle physics experiments: a how-to approach*. Springer Science & Business Media, 2012.

[49] Lellery Storm and Harvey I Israel. Photon cross sections from 1 keV to 100 MeV for elements Z= 1 to Z= 100. *Atomic Data and Nuclear Data Tables*, 7(6):565–681, 1970.

[50] RH Howell, RA Alvarez, and M Stanek. Production of slow positrons with a 100-MeV electron linac. *Applied Physics Letters*, 40(8):751–752, 1982.

[51] C Hugenschmidt. The status of the positron beam facility at NEPOMUC. In *Journal of Physics: Conference Series*, volume 262, page 012002. IOP Publishing, 2011.

[52] Byron T Wright. Spectrometer measurement on the high energy positrons of sodium 22. *Physical Review*, 90(1):159, 1953.

[53] B Krusche and K Schreckenbach. Intense positron sources by pair creation with neutron capture γ-rays. *Nuclear Instruments and Methods in Physics Research Section A: Accelerators, Spectrometers, Detectors and Associated Equipment*, 295(1):155–171, 1990.

[54] Leon Madansky and Franco Rasetti. An attempt to detect thermal energy positrons. *Physical Review*, 79(2):397, 1950.

[55] A Vehanen, KG Lynn, Peter J Schultz, and M Eldrup. Improved slow-positron yield using a single crystal tungsten moderator. *Applied Physics A*, 32(3):163–167, 1983.

[56] RJ Wilson and AP Mills Jr. Positron and positronium emission from tungsten (111). *Physical Review B*, 27(7):3949, 1983.

[57] PJ Schultz, EM Gullikson, and AP Mills Jr. Transmitted positron reemission from a thin single-crystal Ni (100) foil. *Physical Review B*, 34(1):442, 1986.

[58] Cherry A Murray and Allen P Mills. Narrow beam emission of slow positrons from negative affinity surfaces. *Solid State Communications*, 34(10):789–794, 1980.

[59] DA Fischer, KG Lynn, and DW Gidley. High-resolution angle-resolved positron reemission spectra from metal surfaces. *Physical Review B*, 33(7):4479, 1986.

[60] DM Chen, KG Lynn, R Pareja, and Bent Nielsen. Measurement of positron reemission from thin single-crystal W (100) films. *Physical Review B*, 31(7):4123, 1985.

[61] R Suzuki, T Ohdaira, A Uedono, Y K Cho, S Yoshida, Y Ishida, T Ohshima, H Itoh, M Chiwaki, T Mikado, et al. Investigation of positron moderator materials for electron-linac-based slow positron beamlines. *Japanese journal of applied physics*, 37(8R):4636, 1998.

[62] J Störmer, A Goodyear, W Anwand, G Brauer, PG Coleman, and W Triftshäuser. Silicon carbide: a new positron moderator. *Journal of Physics: Condensed Matter*, 8(7):L89, 1996.

[63] Peter W Hawkes and Erwin Kasper. *Principles of electron optics*, volume 3. Academic Press, 1996.

[64] Pierre Grivet, Peter William Hawkes, and Albert Septier. *Electron optics*. Elsevier, 2013.

[65] Frank S Crawford. Elementary examples of adiabatic invariance. *American Journal of Physics*, 58(4):337–344, 1990.

[66] Joachim Großer. *Einführung in die Teilchenoptik*. Springer-Verlag, 2013.

[67] Hans Busch and Ernst Brüche. *Beiträge zur elektronenoptik*. JA Barth, 1937.

[68] CJ Davisson and CJ Calbick. Electron lenses. *Physical Review*, 38:585, 1931.

[69] CJ Davisson and CJ Calbick. Electron lenses. *Physical Review*, 42(4):580, 1932.

[70] Johannes Picht. Bemerkungen zu einigen Fragen der Elektronenoptik (Elektronenlinse mit Zwischennetz, Elektronenspiegel, Immersionslinse). *Annalen der Physik*, 428(3-4):249–264, 1939.

[71] J Gratsiatos. Die Gausssche Dioptrik der elektrisch-magnetischen Zylinderlinse. *Zeitschrift für Physik*, 115(1-2):61–68, 1940.

[72] Frank Gray. Electrostatic Electron-Optics. *Bell System Technical Journal*, 18(1):1–31, 1939.

[73] Franz Ollendorff. Elektronik des Einzelelektrons. 1955.

[74] Erik Harting and Frank Henry Read. Electrostatic Lenses. 1976.

[75] Max Knoll and Ernst Ruska. Das elektronenmikroskop. *Zeitschrift für Physik A Hadrons and Nuclei*, 78(5):318–339, 1932.

[76] Peter W Hawkes. *Magnetic electron lenses*, volume 18. Springer Science & Business Media, 2013.

[77] Allen P Mills Jr. Brightness enhancement of slow positron beams. *Applied physics*, 23(2):189–191, 1980.

[78] KF Canter and AP Mills Jr. Slow positron beam design notes. *Canadian Journal of Physics*, 60(4):551–557, 1982.

[79] T Oka, S Jinno, and M Fujinami. Analytical methods using a positron microprobe. *Analytical Sciences*, 25(7):837–844, 2009.

[80] G Kögel. Microscopes/microprobes. *Applied surface science*, 194(1):200–209, 2002.

[81] G Kögel. Positron Microscopy. In *Materials Science Forum*, volume 363-365, page 409. Trans Tech Publ, 2001.

[82] C Hugenschmidt, K Schreckenbach, M Stadlbauer, and B Straßer. Low-energy positrons of high intensity at the new positron beam facility NEPOMUC. *Nuclear Instruments and Methods in Physics Research Section A: Accelerators, Spectrometers, Detectors and Associated Equipment*, 554(1):384–391, 2005.

[83] C Hugenschmidt, H Ceeh, T Gigl, F Lippert, C Piochacz, M Reiner, K Schreckenbach, S Vohburger, J Weber, and S Zimnik. Positron beam characteristics at NEPOMUC Upgrade. In *Journal of Physics: Conference Series*, volume 505, page 012029. IOP Publishing, 2014.

[84] B Strasser, C Hugenschmidt, and K Schreckenbach. Set-up of a slow positron beam for Auger spectroscopy. In *Materials Science Forum*, volume 363, pages 686–688. Trans Tech Publ, 2001.

[85] Christoph Hugenschmidt, Christian Piochacz, Markus Reiner, and Klaus Schreckenbach. The NEPOMUC upgrade and advanced positron beam experiments. *New Journal of Physics*, 14(5):055027, 2012.

[86] J Kopecky. Atlas of neutron capture cross sections. *International Nuclear Data Committee*, 1997.

[87] C Hugenschmidt, G Kögel, K Schreckenbach, P Sperr, B Strasser, and W Triftshäuser. Intense positron source at the Munich research reactor FRM-II. In *Materials Science Forum*, volume 363, pages 425–429. Trans Tech Publ, 2001.

[88] C Hugenschmidt, H Ceeh, T Gigl, F Lippert, C Piochacz, P Pikart, M Reiner, J Weber, and S Zimnik. The Upgrade of the Neutron Induced Positron Source NEPOMUC. In *Journal of Physics: Conference Series*, volume 443, page 012079. IOP Publishing, 2013.

[89] C Piochacz, G Kögel, W Egger, C Hugenschmidt, J Mayer, K Schreckenbach, P Sperr, M Stadlbauer, and G Dollinger. A positron remoderator for the high intensity positron source NEPOMUC. *Applied surface science*, 255(1):98–100, 2008.

[90] C Piochacz. *Technical drawing of the NEPOMUC facility done by Christian Piochacz*, 2013.

[91] P Sperr. Timing measurements with barium flouride scintillators. *Nuclear Instruments and Methods in Physics Research Section A: Accelerators, Spectrometers, Detectors and Associated Equipment*, 254(3):635–636, 1987.

[92] Ulrich Ackermann, Werner Egger, Peter Sperr, and Günther Dollinger. Time-and energy-resolution measurements of BaF 2, BC-418, LYSO and CeBr 3 scintillators. *Nuclear Instruments and Methods in Physics Research Section A: Accelerators, Spectrometers, Detectors and Associated Equipment*, 786:5–11, 2015.

[93] D Schödlbauer, P Sperr, G Kögel, and W Triftshäuser. A pulsing system for low energy positrons. *Nuclear Instruments and Methods in Physics Research Section B: Beam Interactions with Materials and Atoms*, 34(2):258–268, 1988.

[94] C Piochacz. *Generation of a high-brightness pulsed positron beam for the Munich scanning positron microscope*. PhD thesis, Technische Universität München, 2009.

[95] HH Seliger. The backscattering of positrons and electrons. *Physical Review*, 88(2):408, 1952.

[96] PG Coleman, L Albrecht, KO Jensen, and AB Walker. Positron backscattering from elemental solids. *Journal of Physics: Condensed Matter*, 4(50):10311, 1992.

[97] Gigl, T. Temperaturfeldanalyse an einem NEPOMUC-Testaufbau und Messung der Positronenstrahlparameter. Master's thesis, Technische Universität München, 2012.

[98] Mitteneder, J. Erste ortsauflösende Positronen Lebensdauerspektroskopie am Scanning-Positron-Microscope Interface. Master's thesis, Hochschule München, 2015.

[99] J Mitteneder, M Dickmann, G Kögel, W Egger, P Sperr, and G Dollinger. Micrometer positron beam characterization at the scanning positron microscope interface. In *Journal of Physics: Conference Series*, volume 791, page 012006. IOP Publishing, 2017.

[100] David Martin Schrader and Yves C Jean. Positron and positronium chemistry. 1988.

[101] Ulrich Ackermann, Benjamin Löwe, Marcel Dickmann, Johannes Mitteneder, Peter Sperr, Werner Egger, Markus Reiner, and Günther Dollinger. Four-dimensional positron age-momentum correlation. *New Journal of Physics*, 18(11):113030, 2016.

[102] Benjamin Löwe, Markus Reiner, Werner Egger, Christoph Hugenschmidt, and Günther Dollinger. A position sensitive germanium detector for the measurement of angular deviation of annihilation radiation. In *Journal of Physics: Conference Series*, volume 443, page 012098. IOP Publishing, 2013.

[103] Benjamin Löwe. *Entwicklung und Anwendung eines segmentierten Ge-Detektorsystems für die Positronenannihilationsspektroskopie*. PhD thesis, Universität der Bundeswehr München - Institute für angewandte Physik und

Messtechnik LRT2, 2017.

[104] Ulrich Ackermann, Stephan Eschbaumer, Andreas Bergmaier, Werner Egger, Peter Sperr, Christoph Greubel, Benjamin Löwe, Paul Schotanus, and Günther Dollinger. Position and time resolution measurements with a microchannel plate image intensifier: A comparison of monolithic and pixelated CeBr 3 scintillators. *Nuclear Instruments and Methods in Physics Research Section A: Accelerators, Spectrometers, Detectors and Associated Equipment*, 823:56–64, 2016.

[105] Ulrich Ackermann. *Ein Szintillationsdetektor für die Positronenannihilation zur Korrelation von Lebensdauer und 3D-Impuls*. PhD thesis, Universität der Bundeswehr München - Institute für angewandte Physik und Messtechnik LRT2, 2017.

[106] Peter Sperr and Gottfried Kögel. Present performance limits of pulsed positron beams. In *Materials Science Forum*, volume 255, pages 109–113. Trans Tech Publ, 1997.

[107] Daniel Passbach. Konstruktion eines Hochfrequenzresonators für eine gepulste Positronenquelle. Studienarbeit - Universität der Bundeswehr München, LRT2.

[108] René Ernst. Hochfrequenzbeschleuniger (Positronenaufzug) fü das Münchner Rasterpositronenmikroskop. Master's thesis, Universität der Bundeswehr München - Institute für angewandte Physik und Messtechnik LRT2, 2005.

[109] G Kögel and G Dollinger. Planned positron experiments at FRM II. *Applied surface science*, 252(9):3111–3120, 2006.

[110] Marcel Dickmann, Johannes Mitteneder, Gottfried Kögel, Werner Egger, Peter Sperr, Ulrich Ackermann, Christian Piochacz, and Günther Dollinger. Radio frequency elevator for a pulsed positron beam. *Nuclear Instruments and Methods in Physics Research Section A: Accelerators, Spectrometers, Detectors and Associated Equipment*, 821:40–43, 2016.

[111] H von Meinke and Friedrich Wilhelm Gundlach. *Taschenbuch der Hochfrequenztechnik*. Springer-Verlag, 2013.

[112] Horst Stöcker. *Taschenbuch der Physik: Formeln, Tabellen, Übersichten*. Deutsch, 1998.

Danksagung

An dieser Stelle möchte ich mich bei allen bedanken, die mich in den letzten viereinhalb Jahren unterstützt haben und ohne die meine Arbeit in dieser Form nicht möglich gewesen wäre:

Bei Prof. Dr. Günther Dollinger bedanke ich mich dafür, dass er mir die großartige Möglichkeit gab, dieses spannende, aber auch anspruchsvolle Thema im Rahmen einer Dissertation, in einer der weltweit führenden Gruppen auf dem Gebiet der Positronenphysik, zu verwirklichen. Er ließ mir während meiner Zeit am LRT2 stets die Freiheit eigenständig zu arbeiten, half mir aber bei Bedarf mit wertvollen Anregungen und konstruktiver Kritik weiter.

Dr. Werner Egger danke ich für die stets gute Betreuung meiner Arbeit. Seine umfassenden Kenntnisse der angewandten Positronenvernichtung konnte er mir während oftmals langer Strahlzeittage am Reaktor näher bringen. Das Arbeitsklima mit ihm als Leiter der Positronengruppe war und ist hervorragend. Danke auch für die Bereitschaft zur Diskussion jeglicher Art und für die vielen motivierenden Worte an manchen zähen Tagen.

Ein großes Dankeschön geht an Dr. Gottfried Kögel. Von Anfang an ließ er mich an seinem umfassenden Wissen über Positronenstrahlen und Physik im Allgemeinen teilhaben. Ohne seine mühevolle Geduld wäre meine Arbeit in dieser Form nicht entstanden. Des Weiteren bedanke ich mich für die Bereitstellung unentbehrlicher Dokumente, die mir während meiner Zeit am Institut, und darüber hinaus, sehr geholfen haben.

PD Dr. Christoph Hugenschmidt danke ich für das äußerst angenehme Arbeitsklima in der Positronengruppe am Reaktor, in welcher ich untergebracht war. Er stand mir ebenfalls bei Fragestellungen und Problemen immer zur Seite. Mit seiner Unterstützung konnten zahlreiche organisatorische Aufgaben sehr viel schneller umgesetzt werden.

Ein herzliches Dankeschön geht an Johannes Mitteneder, mit dem ich die meiste Zeit zusammengearbeitet habe. Während der unzälihgen Strahlzeittage und –nächte konnten wir häufig Frustration und Euphorie miteinander teilen. Ohne ihn wäre die Inbetriebnahme des SPM an NEPOMUC noch immer in weiter Ferne. Bei der Weiterführung unserer gemeinsamen Arbeit wünsche ich ihm alles erdenklich Gute und weiterhin viel Erfolg.

Des Weiteren gilt mein Dank Dr. Peter Sperr. Er hat mir auf dem Gebiet der angewandten Elektronik viel erklärt und nähergebracht. Mit der Entwicklung und dem Bau seiner Nuklearelektronik trug er maßgeblich zum Versuchsaufbau und zu den Ergebnissen aller meiner Experimente bei.

Dr. Christian Piochacz danke ich dafür, dass er sein Fachwissen über NEPOMUC und den Positronenstrahl am Forschungsreaktor FRM II mit mir teilte. Gerade in meinen ersten Strahlzeiten stand er mir mit Rat und Tat zur Seite und trug damit wesentlich zum Gelingen dieser Arbeit bei.

Meinen Kollegen Dr. Ulrich Ackermann, Dr. Tönjes Koschine, Benjamin Löwe und Dr. Luca Ravelli danke ich für die sehr gute und äußerst lustige Zusammenarbeit in den letzen Jahren. Gerade die teilweise ermüdenden PLEPS-Strahlzeiten konnte ich mit Eurer Hilfe sehr viel besser meistern.

Sehr zum Gelingen dieser Arbeit trug außerdem Sebastian Vohburger bei, dem ein besonderer Dank gilt. Mit seinen weitreichenden technischen Fähigkeiten half er mir maßgeblich beim Experimentaufbau am Reaktor. Nur durch seine unermüdliche Unterstützung konnte der Versuchsaufbau in dermaßen kurzer Zeit realisiert werden.

Mein Dank gilt weiterhin den Technikern der LRT2-Werkstatt, Ralph Schubert und Wolfgang Engl, für die Hilfe beim Erstellen wesentlicher Bauteile für den Aufbau und zur Verbesserung des Experiments.

Bei Benjamin Rienäcker bedanke ich mich für die wertvolle Unterstützung beim Programmieren. Große Teile der neuen Software konnten erst mit seiner Hilfe vernünftig zum Laufen gebracht werden.

Ich bedanke mich außerdem bei Dr. Markus Reiner und Thomas Gigl für die kollegiale Zusammenarbeit und für die gegenseitige Unterstützung am Reaktor, allen voran bei der Absprache unserer Strahlzeiten und den anschließenden Diskussionen.

Ferner möchte ich mich bei meinen Doktorandenkollegen Dr. Ulrich Ackermann, Dr. Hubert Ceeh, Matthias Dodenhöft, Thomas Gigl, Benjamin Löwe, Johannes Mitteneder, Pascal Neibecker, Dr. Markus Reiner, Benjamin Rienäcker, Josef Schmidbauer, Markus Singer, Dr. Josef-Andreas Weber und Samantha Zimnik bedanken. Die Zeit mit Euch am Reaktor werde ich immer positiv in Erinnerung behalten.

Allen weiteren Kollegen am LRT2 und am Reaktor danke ich für das tolle Arbeitsklima und die gute Zusammenarbeit während der letzten Jahre.

Für das großartige Engagement beim Korrekturlesen meiner Arbeit bedanke ich mich außerdem bei Lukas Beddrich, Johannes Mitteneder, Monika Pless, Michaela Schleuder und Markus Singer.

Mein ganz besonderer Dank gilt meiner Familie und meinen Großeltern, die mich bereits während des Studiums unterstützt und mir beigestanden haben. Nur mit ihrer Hilfe war es für mich möglich diese Arbeit zu vollenden.

Bei Ela bedanke ich mich für die großartige Unterstützung und die aufmunternden Worte in schweren Zeiten, für alle Tipps und Vorschläge, und ihre enorme Geduld.